FLAW TOLERANT ALUMINA / ZIRCONIA

MULTILAYERED COMPOSITES

FLAW TOLERANT ALUMINA / ZIRCONIA MULTILAYERED COMPOSITES

By

Benjamin D. Hatton, B.Sc.Eng.

A Thesis

Submitted to the School of Graduate Studies

in Partial Fulfilment of the Requirements

for the Degree

Master of Engineering

McMaster University

MASTER OF ENGINEERING (1998) McMASTER UNIVERSITY
(Materials Science and Engineering) Hamilton, Ontario

TITLE: Flaw Tolerant Alumina/Zirconia Multilayered Composites for High Temperature Applications

AUTHOR: Benjamin D. Hatton, B.Sc.Eng. (Queen's University)

SUPERVISOR: Professor P.S. Nicholson

NUMBER OF PAGES: xiv, 154

Abstract

Ceramic composites for high temperature applications must be designed with crack arrest capability to improve the resistance to flaws produced in service, such as by thermal shock. Laminated composites containing Al_2O_3 layers in 3mol%Y_2O_3-ZrO_2 (TZ3Y) were fabricated by electrophoretic deposition (EPD) and pressureless sintering. The layering design (Al_2O_3 layer thickness and volume fraction) was varied to determine the influence on fracture behaviour. The residual stress in Al_2O_3 layers was measured using a fluorescence spectroscopy technique.

The fracture strength of 15 different laminates, and monolithic Al_2O_3 and TZ3Y, was tested in 4-point bending at room temperature. Vickers indentation (10 kg load) was used to simulate natural flaws at the sample surface before testing as a measure of flaw tolerance. Fracture ranged from catastrophic failure, to multi-stage failure and complete delamination (in processing). Transitions in behaviour were found related to a geometrical parameter derived from the strain energy release rate for edge cracks.

The strength of three Al_2O_3/TZ3Y composites was compared with monolithic Al_2O_3 and TZ3Y for a range of indentation loads (up to 20 kg). The strength of the composites was similar to monolithic TZ3Y but the flaw tolerance was improved due to multi-stage fracture.

The strength and flaw tolerance (using 10 kg indentation) of two Al_2O_3/TZ3Y composites and monolithic TZ3Y was measured $\leq 1300\,^{\circ}C$. The multi-stage fracture behaviour disappeared $> 25\,^{\circ}C$, and there was no beneficial effect of the Al_2O_3 layers on the strength. Superplastic deformation of the TZ3Y layers at $1300\,^{\circ}C$ was prevented by the constraint of the Al_2O_3 layers. Recommendations are made about the design of flaw tolerant ceramic laminates for high temperature use.

Acknowledgements

The author would like to express his sincere thanks to his supervisor Prof.P.S.Nicholson for guidance, support and ideas during the course of this study. Thanks are also extended to Ena Nicholson for her generosity and organization. All has been greatly appreciated.

In addition the author would also like to recognize the helpful advice of Dr.Partho Sarkar and Prof.J.D.Embury.

The help of Klaus and Marcia, Yosh, George, Connie, Art, Ed and Anton Kitai was invaluable and much appreciated.

Sincere thanks are extended to *everyone* in the A203 Ceramics Research Group for their company, friendship and support, and to all the department for making his stay at McMaster memorable.

Finally, the author would like to thank his family for their encouragement. And to Macarena, tusen and tusener.

Table of Contents

List of Figures

List of Tables

Chapter 1: Introduction

Ceramic oxides (eg. α-Al_2O_3, ZrO_2) have high melting points, low density and good chemical stability, making them attractive for high temperature, corrosive environments. With further development, ceramics may find more common use in structural components such as turbine blades, engine parts, thermally insulating coatings and ballistic armour. The obvious limitation is their inherent brittleness. A fracture resistance of ~ 1000 J/m^2 is generally considered necessary for common structural applications, at least to raise the critical flaw size to a practical, detectable range (Gupta, 1974). Engineering ceramics are typically within 20-200 J/m^2 . Limitations in the influence of microstructure alone (ie; grain size) are such that the toughness of *monolithic* ceramics will never reach such levels. Ceramic *composites* can yield synergistic combinations of strength and toughness.

In the past, work has focused on improving the strength of ceramic components. It has been demonstrated that the majority of strength-limiting defects originate from processing (Sung, 1988; Lange, 1989). Improvements in powder quality, densification and microstructural homogeneity have reduced the size and distribution of processing defects so that strengths > 1 GPa are not uncommon (Becher, 1991). Statistical models, non-destructive evaluation and proof-testing can also be used to ensure that ceramic components have sufficient strength for a given application.

However, increasing the stress to initiate fracture comes at a cost. The large kinetic energy associated with failure at high stress causes spectacular catastrophic failure with no warning (Gupta, 1974). Unexpected failure can be caused by surface defects from impact or thermal shock damage in service which dramatically reduce the strength of brittle materials. The movement towards high strength is not necessary for many applications of ceramics and improvement of

structural *reliability* is more useful (Becher, 1991). *Flaw tolerant* design of ceramic composites ensures that an initially satisfactory strength is not degraded via damage in service. In addition, stabilized crack growth provides warning of catastrophic failure.

Studies on laminar ceramic composites have incorporated tougher materials, weak interfaces and residual stresses to induce crack arrest and/or deflection. The present work will focus on the optimal design of a multi-layered Al_2O_3/ZrO_2 composite for multi-stage fracture (in bending) by means of crack arrest and deflection at layers containing residual stress. The compressive stress in Al_2O_3 layers has a large influence on crack propagation for certain composite designs. In particular, the scale of the layering to optimize strength and flaw tolerance is not fully understood. Weak interfaces in composites are susceptible to creep at high temperature (Raj, 1993). Therefore, the interface between Al_2O_3 and ZrO_2 should be strongly-bonded.

Composites of Al_2O_3 / ZrO_2 + 3mol%Y_2O_3 (TZ3Y) were produced by electrophoretic deposition (EPD), a colloidal technique to produce dense layers of high perfection. The composites were designed with Al_2O_3 layers ($\approx$ 10-200 μm thick, 3-50 Vol%) in a TZ3Y matrix. The flaw tolerance of 15 different composite designs was compared with monolithic TZ3Y and Al_2O_3 in 4-point bending. Surface cracks were introduced by diamond indentation to simulate the flaws caused by impact or thermal shock. Flaw tolerance at high temperatures ($\leq$ 1300°C) was explored in certain composites and compared with monolithic TZ3Y.

Chapter 2: Literature Review

2.1 Brittle Fracture of Ceramics

2.1.1 Conditions of Crack Stability

The fundamentals of linear elastic fracture are discussed in Mai and Lawn (1986), and Lawn (1993). The energy balance condition developed by Griffith (1921) remains the central concept of brittle fracture theory. Griffith modelled a static crack in terms of thermodynamic equilibrium. Considering a 'crack system' as a stable crack in an infinite solid elastic medium, then if **U** is the total energy of the crack system, with crack surface area, **C**, the equilibrium condition defining crack instability is the point at which;

$$\frac{dU}{dC} = 0 \qquad (2.1)$$

ie., the increase of system energy with increasing crack length is zero. The total energy of the system is the sum of the mechanical strain energy (U_m) and the free energy required to create new crack surface (U_S) such that, at equilibrium;

$$\frac{dU}{dC} = \frac{dU_m}{dC} + \frac{dU_s}{dC} = 0 \qquad (2.2)$$

A stressed system stores energy and when a crack propagates this 'strain energy' is released. The *strain energy release rate*, **G**, is defined[1] as;

---

[1] For a straight crack the crack length, **c**, is sufficient to define the crack area, **C**, so that G can be defined per unit width of crack front.

$$G = -\frac{dU_m}{dc} \qquad (2.3)$$

The *resistance to fracture,* **R**, is a material property, defined by;

$$R = \frac{dU_s}{dc} \qquad (2.4)$$

At the point of fracture, according to Equation 2.2;

$$G = R \qquad (2.5)$$

An infinite plate (of unit thickness) containing a through-crack under a uniform applied stress (σ_a) has mechanical energy, $U_m = -\pi c^2 \sigma_a^2 / E'$, where $E' = (1-\nu^2)$. For an *ideal* brittle material, $U_s = 4c\gamma$, where γ is the surface energy (J/m^2). Solving for the applied stress (σ_f) at the equilibrium point of fracture (using Equations 2.3 - 2.5), gives the familiar Griffith result;

$$\sigma_a = \sigma_f = \left(\frac{2E'\gamma}{\pi c}\right)^{1/2} \qquad (2.6)$$

The linear elastic stress field near the tip of a sharp crack can be used to determine the mechanics of fracture in terms of the force to break atomic bonds and is given by;

$$\sigma_{ij} = K(2\pi r)^{-1/2} f_{ij}(\theta) \qquad (2.7)$$

where **r** is a radial distance from the crack tip and **K** is the *stress intensity factor*. At the point that fracture is energetically favourable;

$$K = K_c = T \qquad (2.8)$$

where $\mathbf{K_c}$ is the *critical* stress intensity and **T** is the material *toughness* (MPa $m^{1/2}$). The stress

intensity, strain energy release rate and toughness are related as follows,

$$K = (G\,E')^{1/2} \qquad (2.9)$$

$$T = (R\,E')^{1/2} \qquad (2.10)$$

where $E' = E/(1-\nu^2)$ for conditions of plane strain.

The three modes of fracture are illustrated in **Figure 2.1.** The stress intensity terms for a given mode of fracture (ie; Mode-I opening) are additive quantities. The net stress intensity (K_{net}) for a crack in a material containing internal residual stress is given by;

$$K_{net} = K_{applied} + K_{residual} \qquad (2.11)$$

where $K_{applied}$ (K_a) is the stress intensity due to an applied stress and $K_{residual}$ (K_r) is the stress intensity due to the residual stress. Compressive residual stresses improve the strength and toughness by *reducing* K_{net} for a crack. This effect is known as *apparent* toughening, since it is not an inherent material property (Lakshminarayanan *et al.*, 1987).

For an applied stress σ_a, K_a (Mode-I) is defined by,

$$K_a = \psi \sigma_a c^{1/2} \qquad (2.12)$$

where ψ is a dimensionless parameter defined for different crack geometries.

If the residual stress field is uniform, then K_r can be defined in the same way as an applied stress, ie;

$$K_r = \psi \sigma_r c^{1/2} \qquad (2.13)$$

where σ_r is the residual stress (Lawn, 1993).

Equation (2.1;p.3) defines the equilibrium condition for crack extension but not necessarily for failure. The sign of the second derivative of the strain energy, d^2U/dc^2, must be considered if one is to define whether the equilibrium is stable or unstable. Therefore, in addition to the Griffith energy balance, crack stability conditions are defined as;

$$\frac{dG}{dc} > \frac{dR}{dc} \qquad \textbf{Unstable} \text{ propagation} \qquad (2.14a)$$

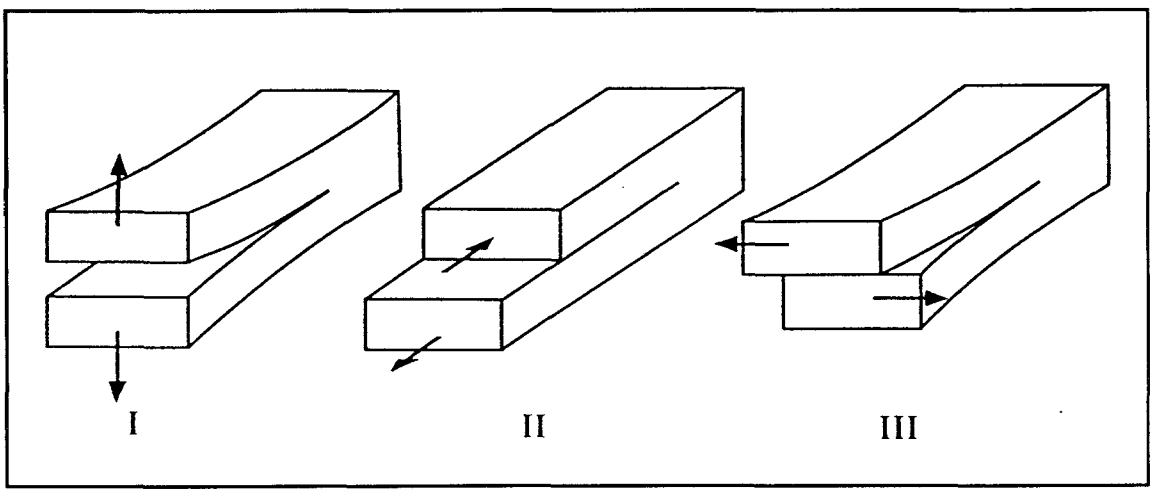

Figure 2.1 The three modes of fracture (Lawn, 1993).

$$\frac{dG}{dc} < \frac{dR}{dc} \qquad \textbf{Stable} \text{ propagation} \qquad (2.14b)$$

Stable crack propagation is a useful property for a material since it provides a 'warning' before unstable, catastrophic failure. Equations 2.14 suggest two situations exist for stable crack propagation. The first is that R(c) is constant and independent of crack length and G(c) is a *decreasing* function of crack length (either due to residual stress or geometrical factors). The second is that G(c) is constant while R(c) *increases* with crack length. The latter is known as *R-curve behaviour*. Microstructural mechanisms operating ahead, (ie. a dilational transformation zone, microcracking) or behind, the crack tip (ie. fibre pullout, grain bridging), result in R-curve behaviour.

The critical condition for unstable fracture is the tangency point on the R-curve where G(c) and R(c) intersect and dG/dc = dR/dc (see **Figure 2.2a**). **Figure 2.2b** is the corresponding T(c) curve. The G(c) curves (1,2 and 3) are linear functions of crack length (Equations 2.9 and 2.12), and the magnitude of σ_a is indicated by the slope of G(c). With increasing applied stress, a crack of initial length $\mathbf{c_0}$, will grow in a stable manner to the critical length, $\mathbf{c_M}$ (at the tangency point **M**). Past this point, dG/dc > dR/dc and the crack will propagate unstably. The fracture strength develops limited independence of the initial flaw size because of stable growth to the critical size (c_m) before fracture. Having a strength *tolerance* to flaws, either from processing or damage in service, improves the reliability of a material.

The shape of the R-curve of a material depends on the specimen geometry and it is not a material parameter. The applied stress necessary to *initiate* stable (or unstable) crack propagation for different crack lengths must be known to experimentally determine R(c) (or T(c)) for a given system.

Significant differences have been noted in the fracture behaviour due to naturally-present,

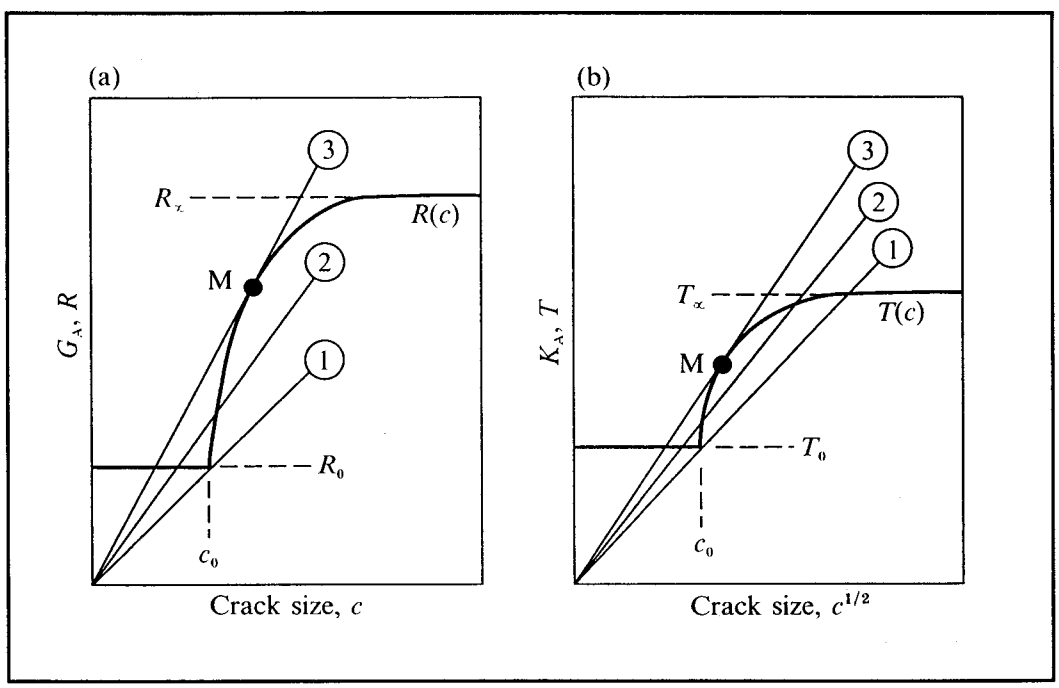

Figure 2.2 Schematic of (a) an R-curve and (b) an equivalent T-curve (Lawn, 1993).

small flaws and the large artificial cracks associated with notched beams (Cook *et al.*, 1985). Indentation with sharp diamond indentors produces sharp flaws at the surface in the short crack scale. These cracks have been shown to be akin to naturally-occurring flaws in ceramics (Lawn, 1983). As a result, measuring the 'indentation strength in bending' (ISB) is a useful way to assess the flaw tolerance of a brittle material (Chantikul *et al.*, 1981)

The stress intensity for the residual stress field around the half-penny shaped cracks produced by sharp indentation (ie; a Vickers diamond) is of the form;

$$K_r = \chi P/c^{3/2} \qquad (2.15)$$

where P is the applied load and χ is a constant for a given material and indentation diamond geometry (Lawn, 1986). Since $T_o = K_r + K_a$ (Equation 2.11; p.5), the *maximum* indentation crack size is;

$$c = \left(\frac{4\chi P}{T_o}\right)^{\frac{2}{3}} \qquad (2.16)$$

By substituting Equation 2.16 into Equation 2.12; p.5, the critical fracture stress (σ_f) in terms of the parameters, χ and P, is;

$$\sigma_f = \frac{3}{4}\left(\frac{T_o^4}{4\psi^3 \chi P}\right)^{1/3} \qquad (2.17)$$

(Lawn *et al.*, 1980). A plot of σ_f vs P should yield $\sigma_f \propto P^{-1/3}$ (a slope of -1/3 on a log-log graph) for an ideal brittle material with a single-valued toughness (T_o). This slope will approach zero if the material is flaw tolerant, ie; the fracture strength is independent of the indentation flaw size and T is not a constant. An example is shown in **Figure 2.3** for large-grain (25μm) Al_2O_3 versus single-

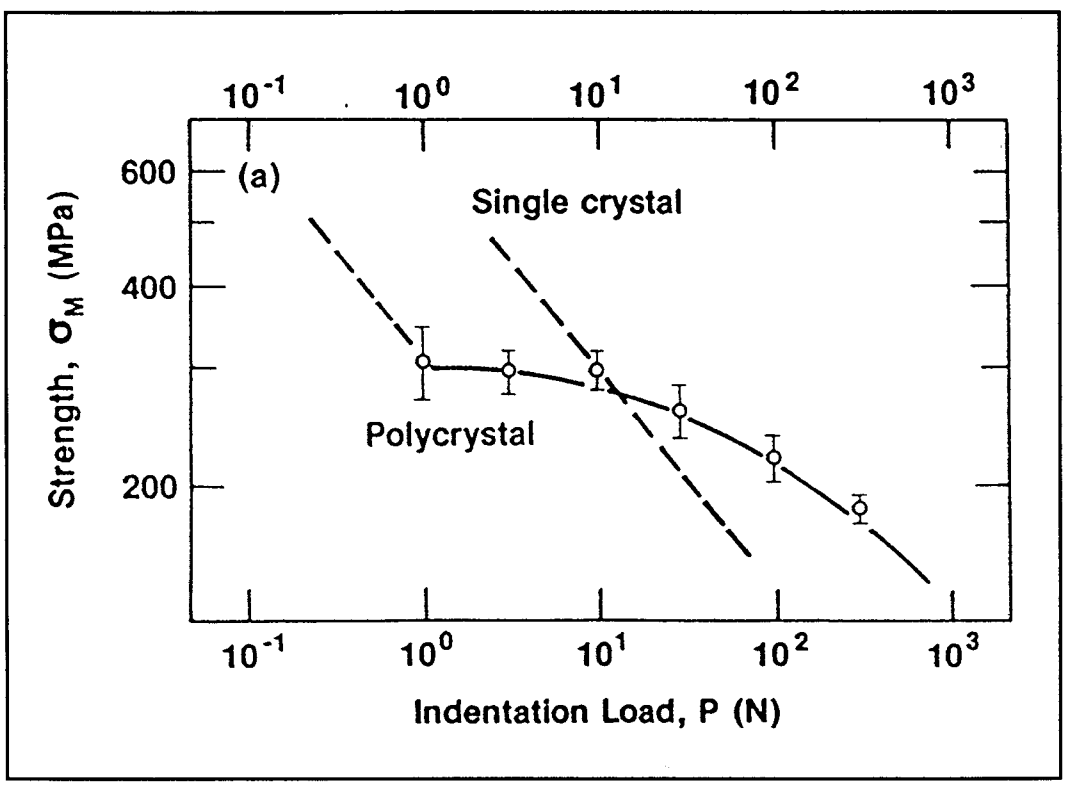

Figure 2.3 Indentation-strength data for polycrystalline and single crystal Al_2O_3 (Mai and Lawn, 1986).

crystal Al_2O_3 (Mai and Lawn, 1986). The elongated grain microstructure in this case helps bridge cracks and the resultant increased toughness improves the flaw tolerance.

There are many examples of use of the ISB technique for characterizing the flaw tolerance of ceramic materials. These include large-grained Al_2O_3 (Braun *et al.*, 1992), Si_3N_4 (Li *et al.*, 1992), and MgO-ZrO_2 (Marshall, 1986). ISB measurement has been applied to layered composites by Hansen *et al.* (1988), Russo *et al.* (1992) and She *et al.* (1998) and will be employed in the present work.

2.1.2 Crack Arrest Criteria

Once a crack becomes unstable, there is an imbalance of forces and the system acquires *kinetic energy*. In this situation, the conditions of static equilibrium defined by Equations 2.2 and 2.14, no longer apply. The kinetic energy associated with a moving crack arises because of the inertia of the material surrounding the crack faces. A 'loading pulse' caused by impact loading, which varies with time from the moment of impact, can also induce material motion. There is a surplus of stored energy for a moving crack to utilise. Mott (1948) included an additional term in the total energy balance, ie;

$$U = U_M + U_S + U_K \qquad (2.18)$$

where U_K is the kinetic energy of the crack system. In terms of the strain energy release rate, this additional kinetic energy is represented by the shaded area between the G(c) and R(c) curves in **Figure 2.4**. It is assumed in this figure that G(c) is linear and R is constant (insensitive to the rate of fracture). In general, U_K can be expressed as;

$$U_k = \int_{c_o}^{c} [G(c) - R(c)]dc \qquad (2.19)$$

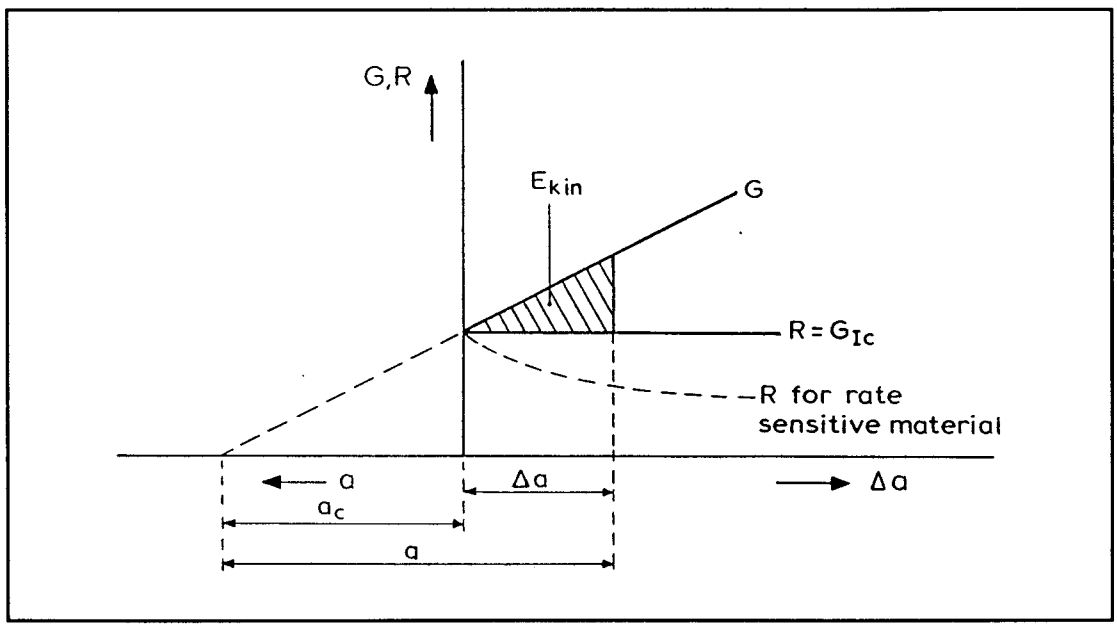

Figure 2.4 Representation of the kinetic energy associated with a crack (Broek, 1978).

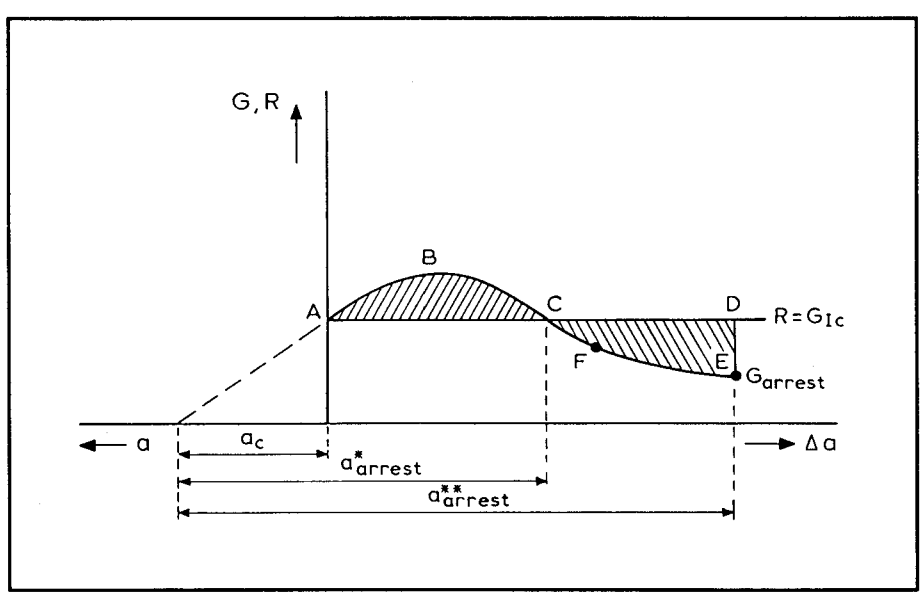

Figure 2.5 Crack arrest due to decreasing G(c) and constant R(c) (Broek, 1978).

(the shaded area in Figure 2.4) for an increase in crack size from $\mathbf{c_o}$ to **c**.

Equations 2.14 suggest that crack arrest will occur if G(c) is a decreasing function of crack length and falls below R(c) (point **C** on **Figure 2.5**) (Broek, 1978). However, the additional kinetic energy associated with the area ABC (Equation 2.19) means crack arrest will not occur until point **E**. At this point, area CDE is equal to area ABC (assuming that all the kinetic energy is used up on crack propagation).

Crack arrest depends on the exact shape of the G(c) and R(c) curves. In the case of a uniform, infinite plate under constant stress, the energy release rate will continue to increase with crack propagation so crack arrest is impossible. However, under certain conditions, either G(c) can *decrease* or R(c) *increase* sufficiently to arrest moving cracks. If a specimen is loaded to constant deflection, for instance, G(c) is a decreasing function and crack arrest will occur as illustrated in Figure 2.5 (Bluhm, 1969).

The kinetic energy associated with a moving crack depends on the applied stress. The inertia associated with a small crack is different from that with a large crack (as the stress to activate the former is higher than the latter). As a result, the position of, and potential for, crack arrest is different for a small and large crack (Broek, 1978).

In general, crack arrest mechanisms can be defined as *structural* or *material* (Bluhm, 1969). Structural factors, such as specimen geometry or residual stress, act to *decrease* G, whilst toughening mechanisms operate in the microstructure of the material to *increase* R. A crack arrest design utilised in metals is to weld a strip of a tough, ductile metal within a more brittle plate **(Figure 2.6)** (Bluhm, 1969). **Figure 2.7(a)** illustrates how the higher toughness of the ductile strip produces a stepped increase in R(a) (in this case, **a** is the crack length). Crack arrest occurs when G(a) intercepts R(a) and the two shaded areas are equal. There are two G(a) curves corresponding to cracks of different size in **Figure 2.7(b)**. Curves **m** and **n** represent crack systems with sufficient kinetic energy to avoid crack arrest. In curve **n** the areas between the G(a) and R(a) curves are not

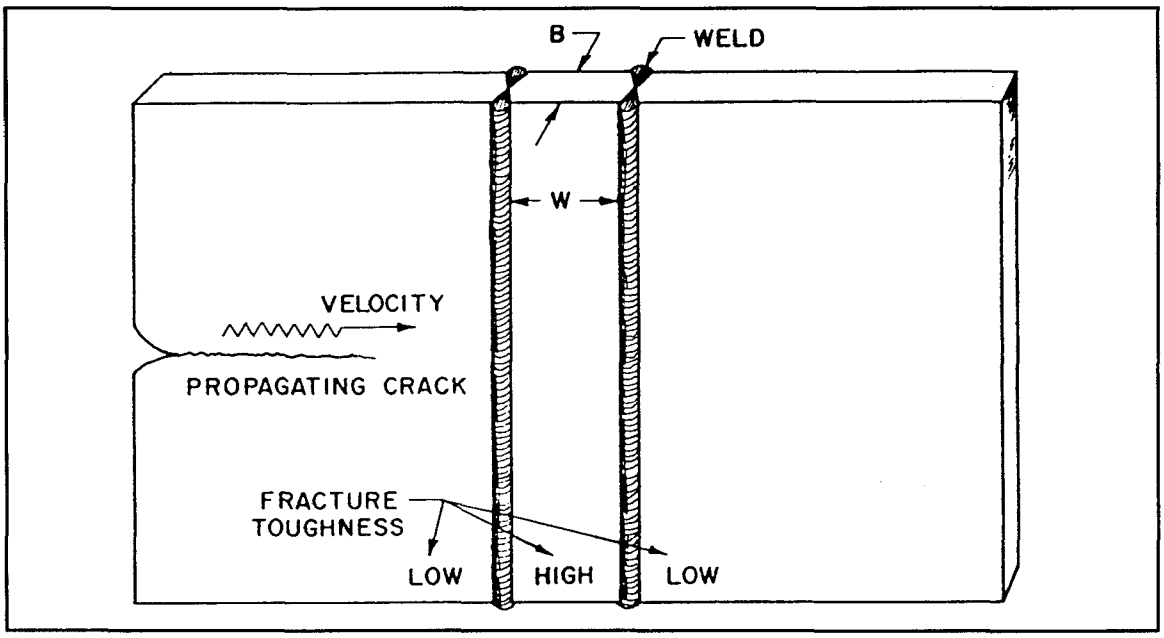

Figure 2.6 Layer of high toughness welded in a metal plate for crack arrest (Bluhm, 1969).

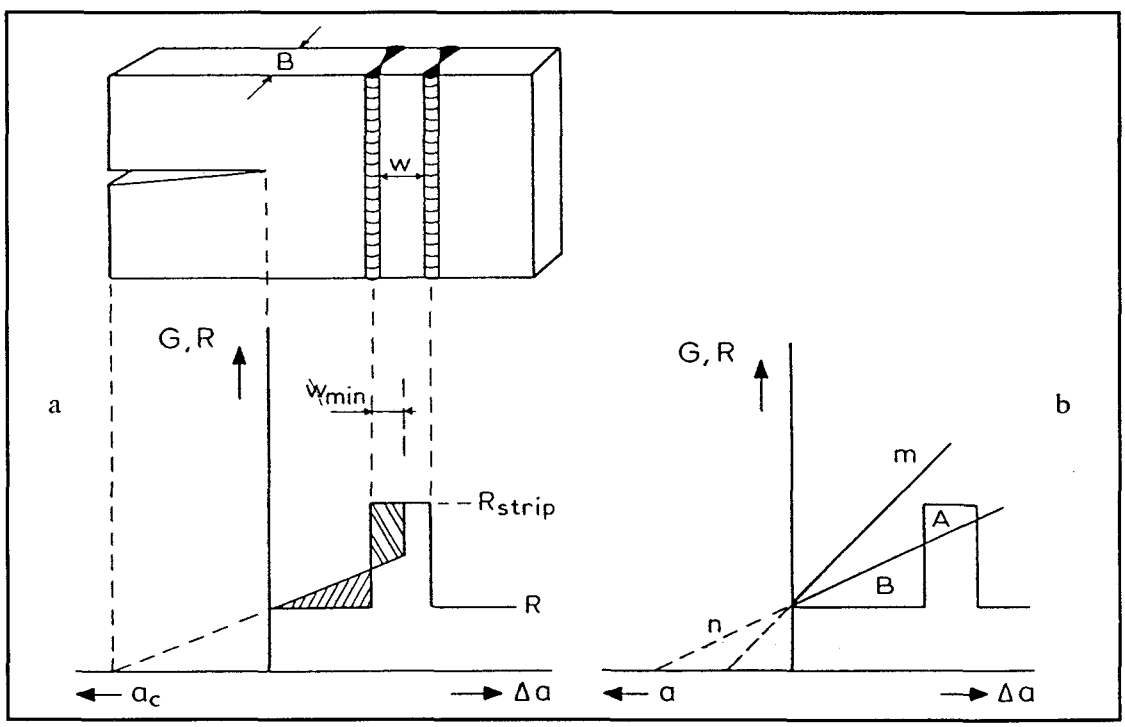

Figure 2.7 (a) Crack arrest at welded insert **(b)** Crack arrest not achieved (Broek, 1978).

equal, and curve **m** misses the R(a) step altogether (Broek, 1978).

Layered ceramic composites have also been designed to include layers of higher toughness (Russo, 1992; Chen and Mecholsky, 1995). The design of layered composites that incorporate residual stress (the present study) to limit crack propagation constitutes a *structural* approach to crack arrest since the stress depends on the layer geometry.

2.1.3 Conditions for Crack Deflection

Crack deflection is a change of crack path to maximize the reduction of total system free energy. If the total free energy (Equation 2.1) is expressed in differential form;

$$\begin{aligned} dU &= dU_m + dU_s \\ dU &= -Gdc + R_o dc \\ -\frac{dU}{dc} &= G - R_o \end{aligned} \qquad (2.20)$$

then the optimal crack path will *maximize* the term ($G - R_o$), which is known as the 'motive force' for fracture (Lawn, 1993). Therefore, either a large driving force G(c) (due to residual stress or geometry) or a low resistance R(c) (a weak interface) will cause deflection from the path of the 'parent' crack.

The condition for deflection (to some angle θ), along an interface is given by,

$$\frac{G_\theta}{G_s} > \frac{R_i}{R_s} \qquad (2.21)$$

where G_θ is the energy release for a deflected crack and G_s for a straight crack. R_i is the mixed-mode fracture resistance for an interface and R_s the Mode-I fracture resistance of the substrate

material (through the interface). This condition is based on the assumption that $G_\theta = R_i$ before $G_s = R_s$ (He and Hutchinson, 1989; Lawn, 1993).

Grain boundaries are common weak interfaces in polycrystalline ceramics. Equation 2.21 gives the conditions that determine the transition from transgranular to intergranular fracture, depending on the value of the ratio R_{GB}/R_{bulk} (where R_{GB} is the fracture resistance of the grain boundary) (Lawn, 1993). Models for crack deflection in layered composites are discussed in Section 2.4.2.

2.2 The Influence of Temperature on the Fracture of Ceramics

2.2.1 Thermal Shock

Thermal shock is a common cause of surface flaws in ceramics for high temperature applications. Although ceramics are well suited to high temperature environments, they are more susceptible to thermal shock than metals due to their low thermal diffusivity and inherent brittleness (Kingery, 1955).

The most deleterious thermal shock is caused by rapid cooling since the surface is put into tension. The magnitude of thermal gradients which develop within a material depends on the rate of heat transfer. The Biot number (β) is a non-dimensional parameter which describes the ratio of heat transfer at the surface to heat conduction through the bulk of a material section. It is given by;

$$\beta = \frac{bh}{k} \qquad (2.22)$$

where **b** is the slab thickness, **h** is the heat transfer coefficient, and **k** is the thermal conductivity. **Table 2.1** lists values of **h** for typical engineering environments (Kingery, 1955). A turbine blade, for example, is subject to extreme temperature changes when the fuel supply is cut and cool air is forced through the hot section of the turbine (Schneibel *et al.*, 1998).

Figure 2.8 is a graph of the surface stress versus time during the heating of an infinite slab for different values of β (Kingery,1955). Large values of β (ie. large heat transfer coefficient, large specimen thickness, or low thermal conductivity) induce the highest thermal stresses. The stresses quickly reach a maximum and then decay with time.

Various parameters can be used to measure the resistance of a material to thermal shock (Hasselman,1970). The first parameter (R_1) measures the maximum temperature gradient allowed

Conditions	h (Btu/hr/ft²/°F)	h (cal/sec/cm²/°C)
Air flow past cylinder:		
Flow rate 60 lb/sec/ft²	190	0.026
Flow rate 25 lb/sec/ft²	90	.012
Flow rate 2.5 lb/sec/ft²	20	.0027
Flow rate 0.025 lb/sec/ft²	2	.00027
Radiation to 0°C from 1000°C	26.0	.0035
Radiation to 0°C from 500°C	7.0	.00095
Water quenching	1000–10,000	.1–1.0
Jet turbine blades	35–150	.005–0.02

Table 2.1 Typical values of the surface heat transfer coefficient (Kingery, 1955).

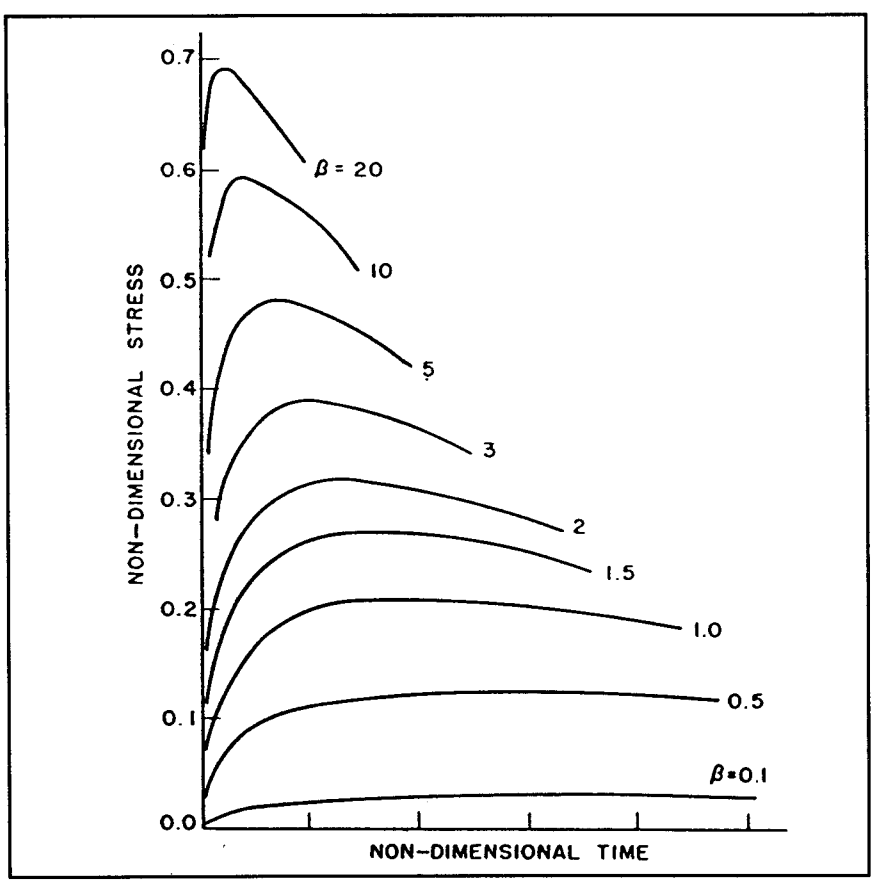

Figure 2.8 Variation of dimensionless thermal stress with dimensionless time for an infinite plate (Kingery, 1955).

before fracture initiates. R_1 can be approximated for non-steady state heat conduction over a wide range of β by;

$$R_1 = \Delta T_{max} = \frac{2.5\sigma_f(1-\nu)}{\alpha E}\left\{1+\frac{2}{\beta}\right\} \qquad (2.23)$$

A second parameter (R_2) is proportional to the maximum crack extension *after* thermal shock fracture initiates, given by;

$$R_2 = \frac{ER_o}{\sigma_f^2(1-\upsilon)} \qquad (2.24)$$

(where R_o is the fracture resistance). In a brittle solid, R_2 is essentially a measure of the strength retained after thermal shock (derived from Equation 2.6; p.4).

Maximizing R_1 by choosing a material with high σ_f/E is counter to maximizing R_2, which requires high E/σ_f^2 . The alternative is to increase R_o (ie. via crack arrest mechanisms) and maximize R_2 independently of R_1 (Hasselman, 1969; Kelly and MacMillan, 1986).

2.2.2 High Temperature Fracture

The strength of polycrystalline ceramics changes with temperature **(Figure 2.9)** (Jayatilaka, 1979). Region (a) represents brittle fracture as defined by linear elastic fracture mechanics, ie; failure originates from inherent flaws in the material. At high temperatures (region (c)) macroscopic yielding initiates cracks which, in turn, lead to failure. Fracture is preceded by nonlinear deformation at high temperatures and is caused by the accumulation of creep damage. **Figure 2.10** illustrates the relationship between stress and failure time for a given temperature in terms of crack nucleation, crack growth and blunting and crack coalescence (Dalgleish *et al.*, 1984). In the present work, the failure time was maintained low (ie; high loading rates were

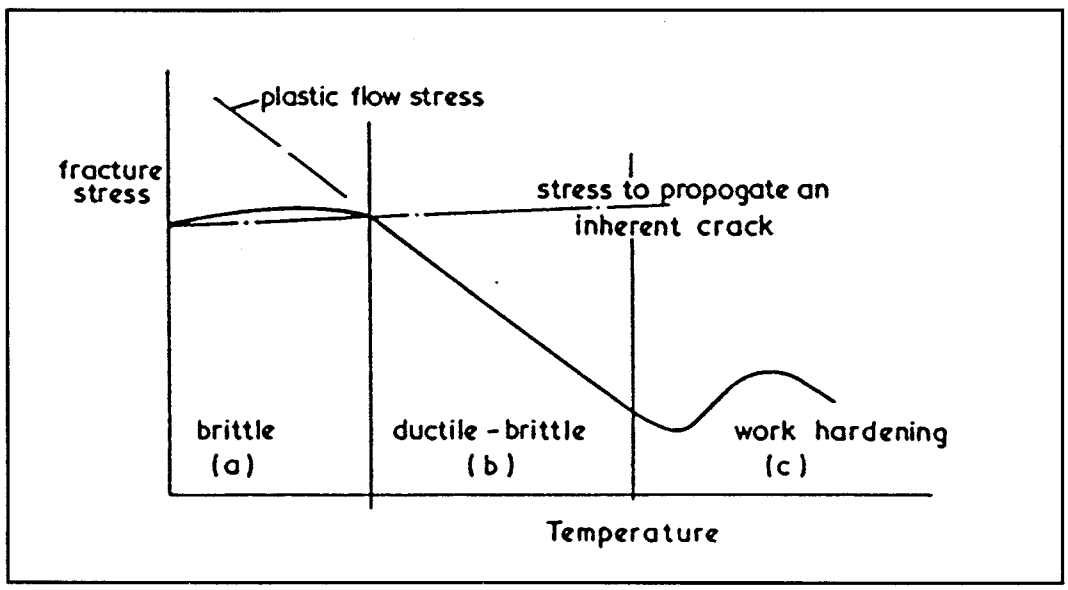

Figure 2.9 The fracture stress of ceramics as a function of temperature (Jayatilaka, 1979).

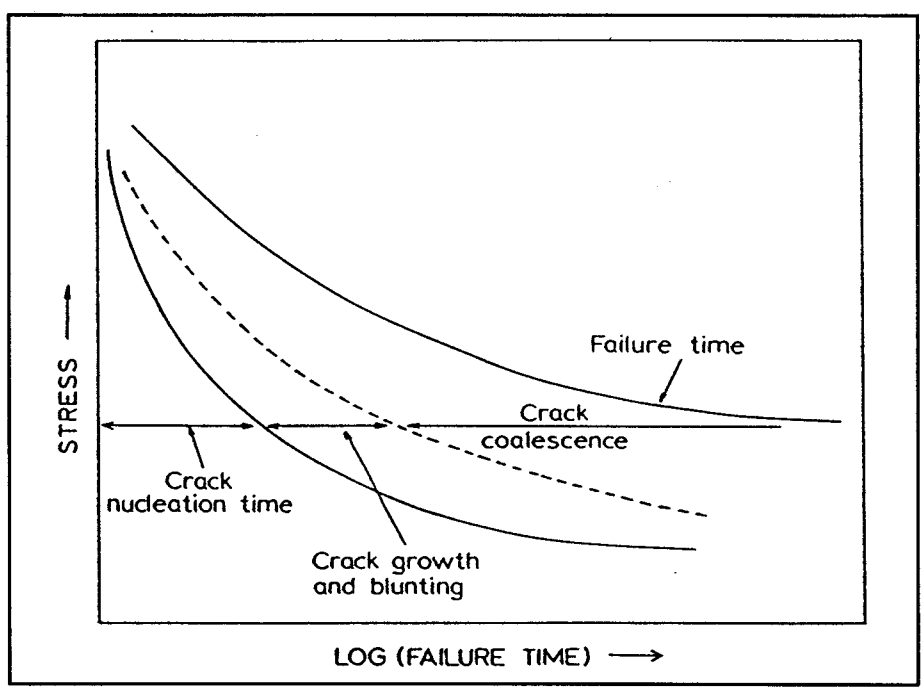

Figure 2.10 The influence of applied stress on failure time for fracture at high temperature (Dalgleish *et al.*, 1984).

employed) to simulate fracture from flaws due to impact or thermal shock. The influence of creep was thus minimized.

In partially stabilized zirconia (PSZ), a transformation zone extends ahead of a crack tip and this acts to reduce the net stress intensity. The dilational phase transformation from a tetragonal to monoclinic crystal structure contributes to the high fracture resistance of PSZ ceramics (at ambient temperatures), and is known as *transformation toughening*.

The tetragonal phase of partially stabilized Y_2O_3-(t)ZrO_2 (or Y-TZP) becomes stable at temperatures over ~ 750°C (Green *et al.*, 1989). The strength of Y-TZP decreases significantly as transformation toughening disappears at high temperatures. Huang and Nicholson (1993) measured the 4-pt bend strength of tape-cast TZ3Y at 25-1300°C (loading rate 0.2-0.5 mm/min). The results are shown in Table 2.2.

Temp(°C)	σ_f (MPa)
25	935 ± 54
800	176 ± 38
1300	113 ± 31

Table 2.2

The extensive deformation of polycrystalline Y-TZP at temperatures over ~1200°C is due to the *superplasticity* caused by grain boundary sliding of a fine grain-sized material (Wakai *et al.*, 1986). The strain rate dependence of superplasticity for Y-TZP was measured by Nieh and Wadsworth (1990). Extensive grain boundary sliding was attributed to segregation of Y to the grain boundaries (Na and Si were not detected). Govilla (1995) measured the strength of 3mol% Y_2O_3-TZP (or TZ3Y) as a function of temperature from 20 to 1000°C (4-pt bend, loading rate 0.5 mm/min) and found it to decrease continuously (**Figure 2.11**). Energy dispersive x-ray spectra (EDS) revealed Si distributed inhomogeneously throughout the matrix and identified the fracture

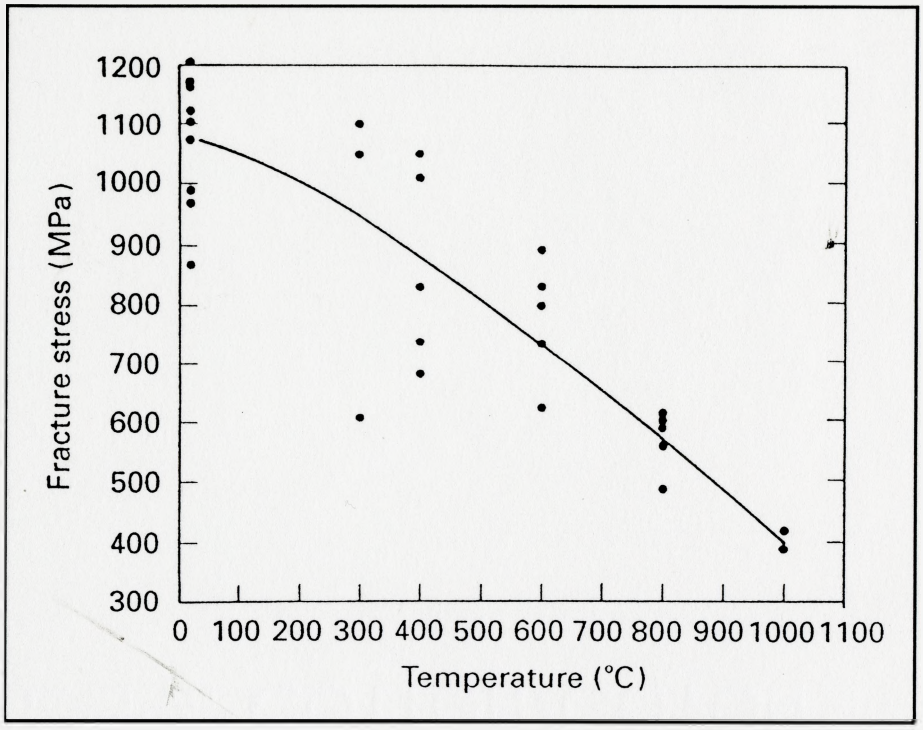

Figure 2.11 4-point bend strength of Y-TZP (at 0.5 mm min^{-1}) as a function of temperature (Govilla, 1995).

surface as covered with amorphous SiO_2. Silicate impurity is commonly found in commercial Y-TZP ceramics as a remnant from the processing of zircon ($ZrSiO_4$) to ZrO_2.

Whitehead (1991) measured the high temperature, 4-pt bend strength of Al_2O_3 prepared by electrophoretic deposition (Section 2.5.1). The results are shown in Table 2.3.

Temp (°C)	σ_f (MPa)
25	556 ± 11
800	475 ± 10
1300	353 ± 39

Table 2.3

There has been limited experimental work on the high temperature properties of multilayered ceramic composites. Jiménez-Melendo *et al.* (1997) prepared layered Al_2O_3 (125μm thick) and Al_2O_3-15vol%TZ3Y (400μm thick) composites by sequential slip casting. Sintering at 1550°C and 1700°C resulted in average Al_2O_3 grain sizes of 3μm and 40μm, respectively. The grain size of the Al_2O_3-15vol%TZ3Y layers remained the same (3-4 μm) as the TZ3Y grains pinned the Al_2O_3 grain boundaries.

The strength in compression was measured at 1400°C (at 5μm/min) for the composites, and for monolithic Al_2O_3 and Al_2O_3-15vol%TZ3Y. The final strength of the composites was found to be similar to monolithic Al_2O_3, but the ductility was closer to that for monolithic Al_2O_3-15vol%TZ3Y. Failure initiated from Al_2O_3 layers in the composites and the controlling parameter was grain size.

2.3 Residual Stress in Layered Structures

2.3.1 The Development of Residual Stress

Residual stresses in layered, ceramic composites arise due to strain mismatch between the bonded layers. This strain mismatch develops from differences in thermal expansion following cooling from sintering temperatures, or due to volume changes accompanying phase transformations.

Calculation of the average biaxial stress within constrained layers of a multilayer composite is based on a simple force balance across the layers. An isotropic, layered composite is illustrated in **Figure 2.12.** The net strain ($\Delta\epsilon$) for two bonded layers cooled from an initial temperature (T_i) to a final temperature (T_f) is given by;

$$\Delta\varepsilon = \int_{T_i}^{T_f} (\alpha_1 - \alpha_2) dT \qquad (2.25)$$

where α_1 and α_2 are the coefficients of thermal expansion for layers 1 and 2, respectively (Timoshenko and Goodier, 1964). Since the layers are bonded, the net strain must be the sum for both layers, ie;

$$\Delta\varepsilon = \varepsilon_1 + \varepsilon_2 \qquad (2.26)$$

Furthermore, the forces within the layers must balance across the cross-section of the composite, ie;

$$\sum \sigma_1 t_1 + \sum \sigma_2 t_2 = 0 \qquad (2.27)$$

where t_i is the thickness, and σ_i is the average biaxial stresses for layers 1 and 2, respectively. Combining equations 2.25, 2.26 and 2.27 gives the residual stress in layer 1 as;

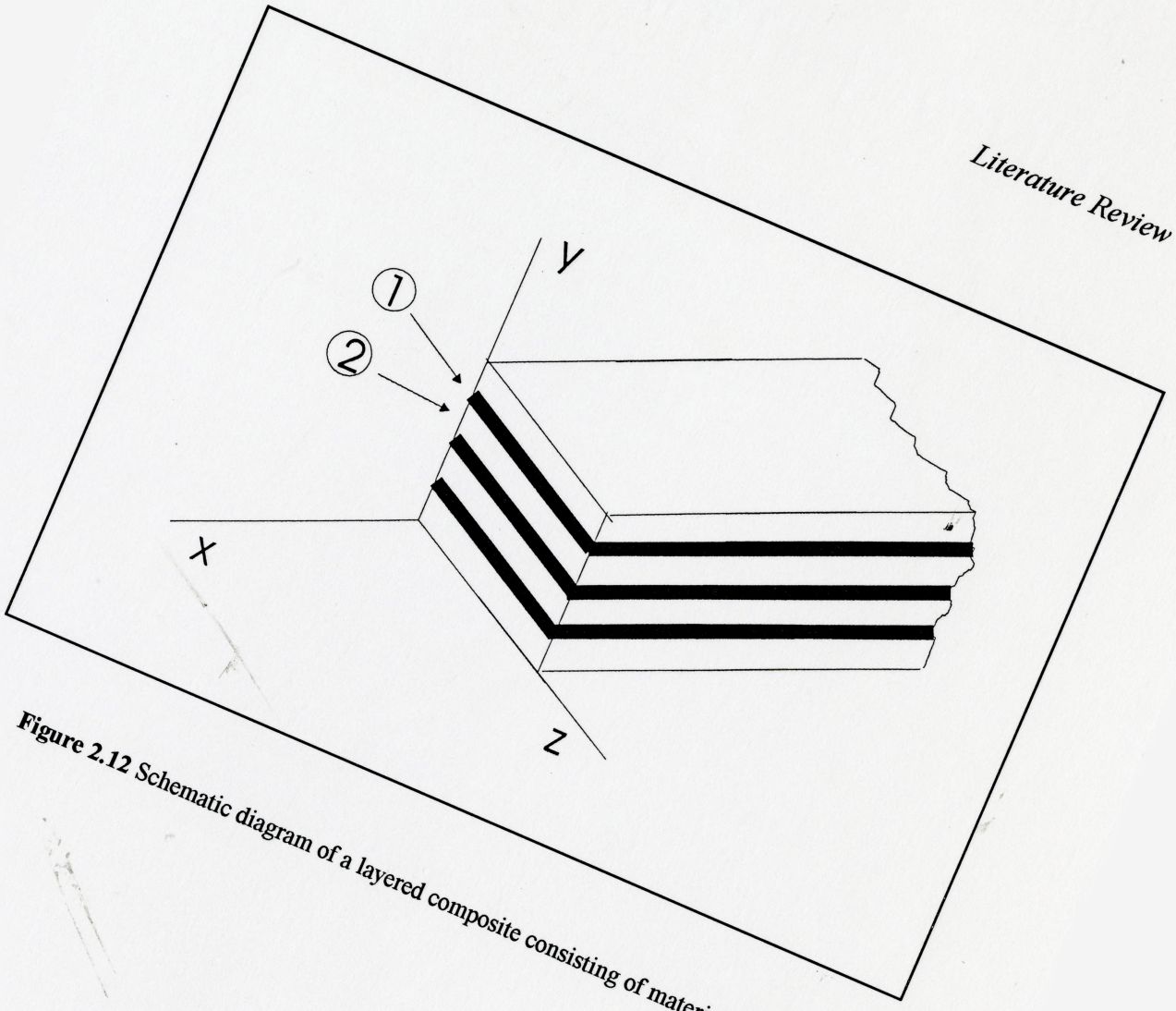

Figure 2.12 Schematic diagram of a layered composite consisting of materials 1 and 2.

$$\sigma_1 = -\Delta\varepsilon E_1' \left(1 - \frac{\sum t_1}{\sum t_2}\frac{E_1'}{E_2'}\right)^{-1} \qquad (2.28a)$$

and that in layer 2 as;

$$\sigma_2 = \Delta\varepsilon E_2' \left(1 - \frac{\sum t_2}{\sum t_1}\frac{E_2'}{E_1'}\right)^{-1} \qquad (2.28b)$$

where $E'_i = E_i/(1-\nu_i)$ (Ho *et al.*, 1995).

Equation 2.25 suggests stress should develop following cooling from the sintering temperature (1550°C in the present study). However, the superplasticity of PSZ over ~1200 °C (Section 2.2.2) will cause viscous flow and relax the residual stress.

Cai *et al.* (1997a) studied defect evolution in tape cast laminates of Al_2O_3 and Al_2O_3+Ce-ZrO_2 . **Figure 2.13** shows the Al_2O_3/ZrO_2 interface in a composite which shows imperfect densification. They observed that the spacing of tunnel cracks within the tensile layers (Al_2O_3+Ce-ZrO_2) was sensitive to the cooling rate following sintering, which indicates the influence of time-dependent, viscoelastic relaxation of the layers. Cai *et al.* (1997b) modelled the evolution of stresses for different cooling rates, based on the measured viscoelastic parameters for Al_2O_3 and Ce-ZrO_2 . **Figure 2.14** illustrates the evolution of residual stress in their laminates (of different composition) for fast and slow cooling from 1500°C. Temperatures ≥1200°C were sufficient to relieve thermal stress on controlled cooling at 3°C/min. During fast cooling (furnace shut-off), stresses developed immediately at 1500°C.

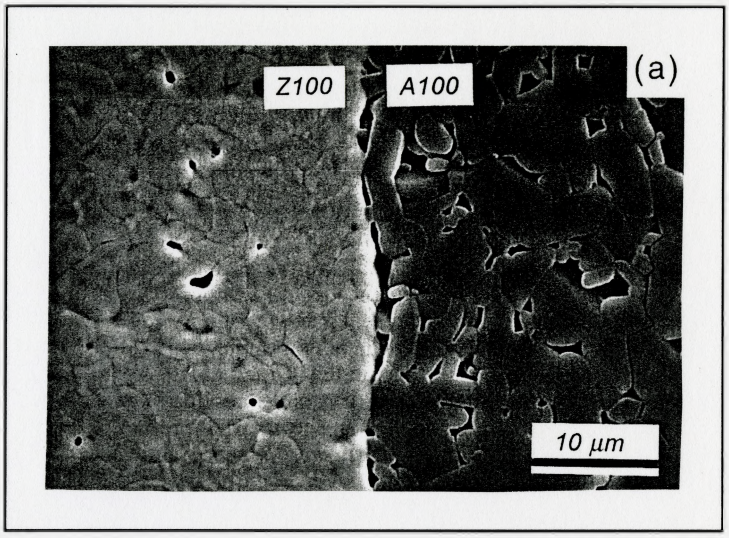

Figure 2.13
The Al_2O_3/ZrO_2 interface in a multilayered composite produced by tape casting (Cai *et al.*, 1997a).

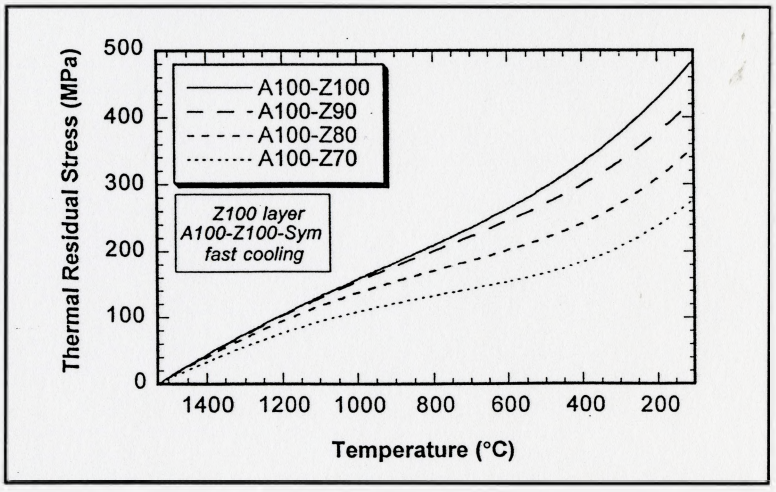

(a)

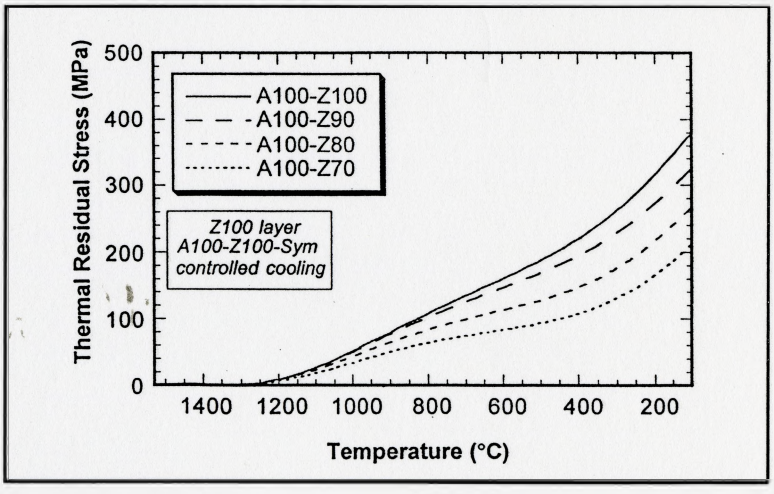

(b)

Figure 2.14
Calculated thermal stress in $Al_2O_3/Al_2O_3+ZrO_2$ composites caused by **(a)** furnace cooling and **(b)** 3 °C/min controlled cooling (Cai *et al.*, 1997b).

The biaxial stress within a layer (σ_r) (calculated by Equations 2.28) is valid at a depth far from the free surface. Close to the free surface there is an imbalance of forces since the stress normal to the surface is necessarily zero. Considering the y-z face of the composite in Figure 2.12; p.25, a significant stress (σ_{yy}) exists normal to the layer plane at the free surface (x = 0). **Figure 2.15** illustrates the imbalance of forces at a surface which leads to σ_{yy} (σ_{R1} is compressive and σ_{R2} is tensile) (Ho *et al.* 1995). The sign of σ_{yy} is opposite to σ_r, ie; σ_{yy} is tensile at the surface of a compressed layer. σ_{yy} is at a maximum at the surface then decreases with x over a distance the order of the layer thickness, t. A localized *tensile* stress at the surface causes shallow edge cracks to form (Section 2.4.3).

Ho *et al.* (1995) determined an analytical solution for $\sigma_{yy}(x)$ by considering the surface stress state as being the superposition of two simpler problems (**Figure 2.16**). Problem A is simply the biaxial stress acting within a constrained layer (given by Equations 2.28). In Problem B a point stress, σ_M, acts at the free surface of a constrained layer. The solution to Problem B can be found by integrating for a point force on a free surface (Timoshenko and Goodier, 1964). The result for $\sigma_{yy}(x)$ (normalized to σ_M) (along the centreline of the layer) is given by;

$$\frac{\sigma_{yy}(x)}{\sigma_M} = \frac{2}{\pi}\left[\theta - \frac{1}{2}\sin 2\theta\right] \qquad (2.29)$$

where $\tan\theta = t/2x$, and t is the layer thickness. A graph of σ_{yy}/σ_M as a function of x/t (for different values of y/t within the layer) is shown in **Figure 2.17.**

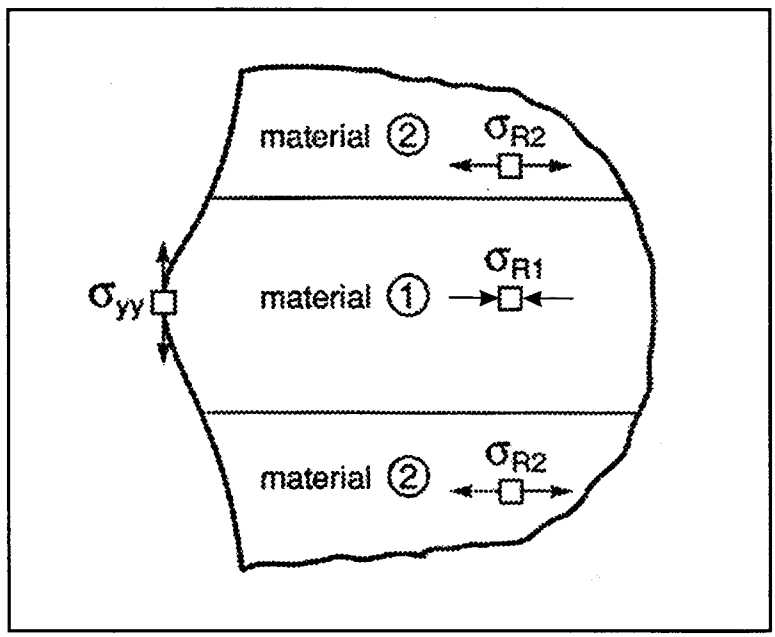

Figure 2.15 The force imbalance at the surface of a residually compressed layer which causes localized tensile stress (σ_{yy}) to form (Ho *et al.*, 1995).

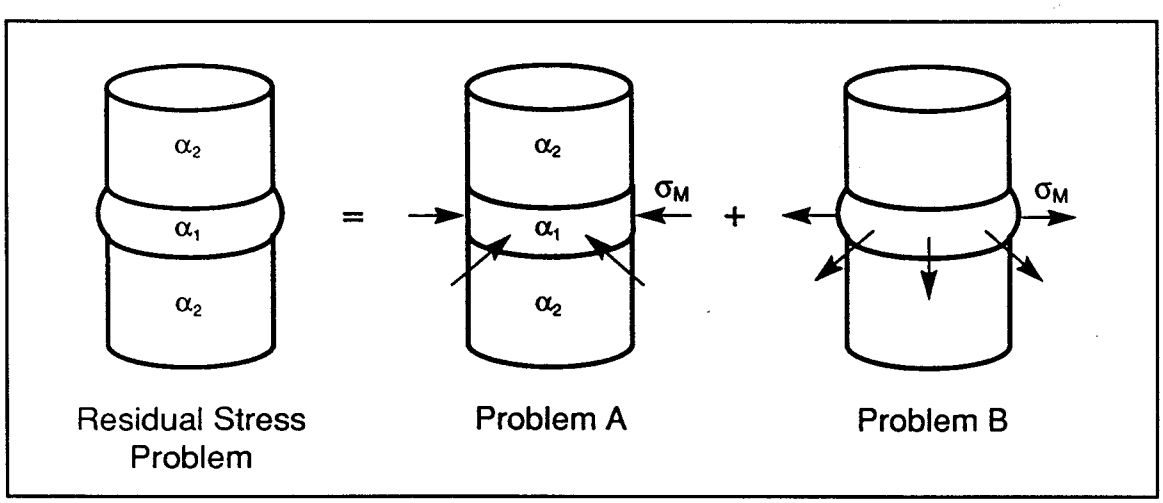

Figure 2.16 The superposition of problems A and B to solve for σ_{yy} (Ho *et al.*, 1995).

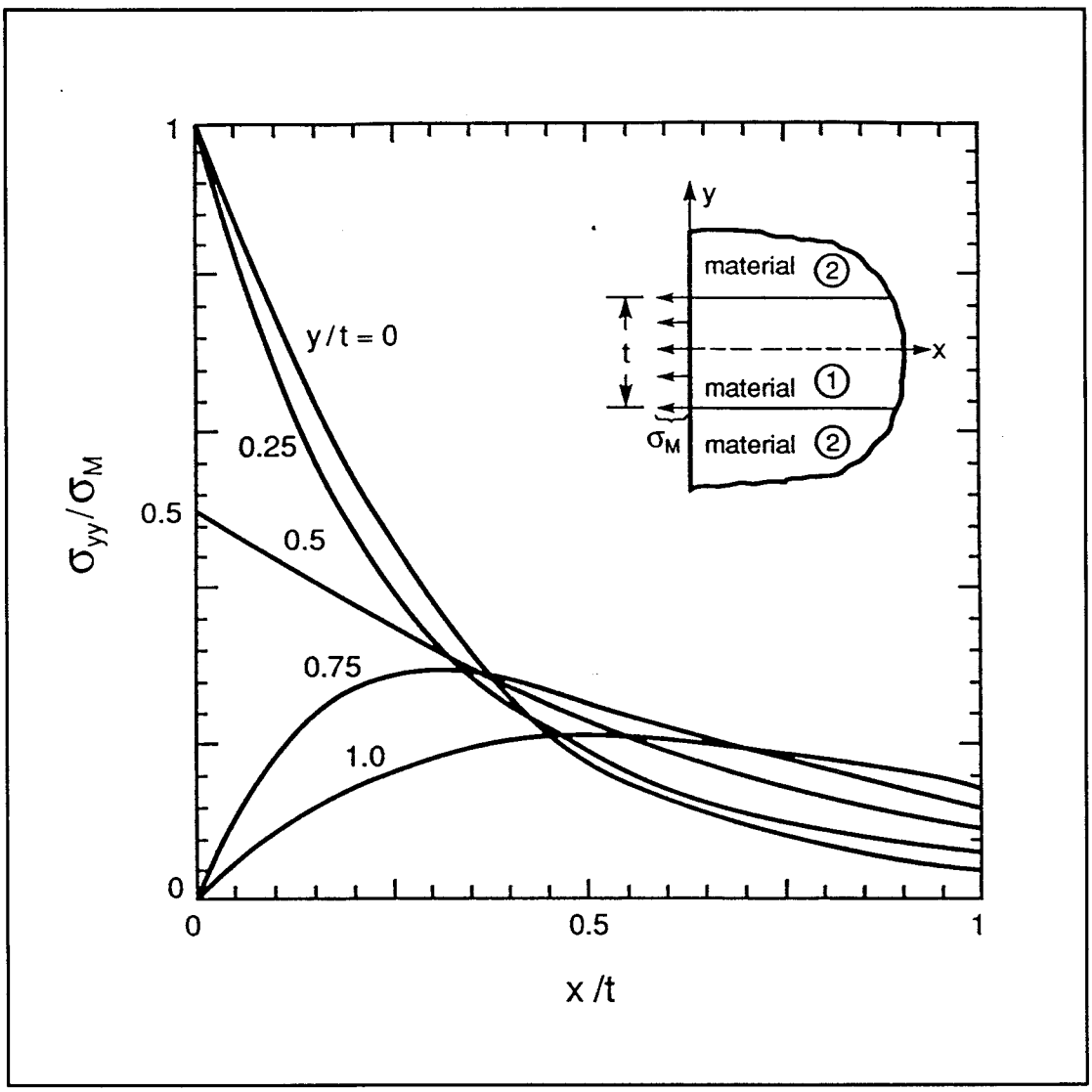

Figure 2.17 The solution for σ_{yy} (normalized by σ_M) as a function of x/t (Ho *et al.*, 1995).

2.3.2 The Piezospectroscopic Measurement of Stress in Al_2O_3

Chromium ions are a common impurity in Al_2O_3 and occupy substitutional sites as Cr^{3+}. When excited by an energy source (eg. an argon ion laser), the Cr^{3+} ions fluoresce at a frequency which is sensitive to the strain distortion of the host lattice (Grabner, 1978; Ma and Clarke, 1993). This stress influences the transition energy between the electronic states. A change in the energy associated with electronic transitions (causing luminescence) causes a frequency shift in the fluorescence spectral lines. There are two distinct radiative transition lines for Cr^{3+} in Al_2O_3, R1 and R2 (at 1.790 and 1.794 eV), as shown in **Figure 2.18** for single crystal and polycrystalline Al_2O_3 (Ma and Clarke, 1993).

The theory for applying fluorescence spectroscopy to measure stress in polycrystalline Al_2O_3 was developed by Grabner (1978). The relationship between the shift in frequency ($\Delta\nu$) and the stress state of the Al_2O_3 lattice is given by;

$$\Delta\nu = \Pi_{ij}\,\sigma_{ij} \qquad (2.30)$$

where Π_{ij} are the *piezospectroscopic coefficients* (cm^{-1}/GPa). The latter form a symmetrical second-rank tensor. The point symmetry of the Cr^{3+} ion means that the off-diagonal Π_{ij} are zero. The values of these coefficients were reported by Grabner (1978), and have been remeasured recently by He and Clarke (1995) (Table 2.4).

	Π_{11}	Π_{22}	Π_{33}
R1	2.56	3.5	1.53
R2	2.65	2.8	2.16

Table 2.4

Figure 2.19 shows the linear change in frequency with a uniaxial applied stress for polycrystalline

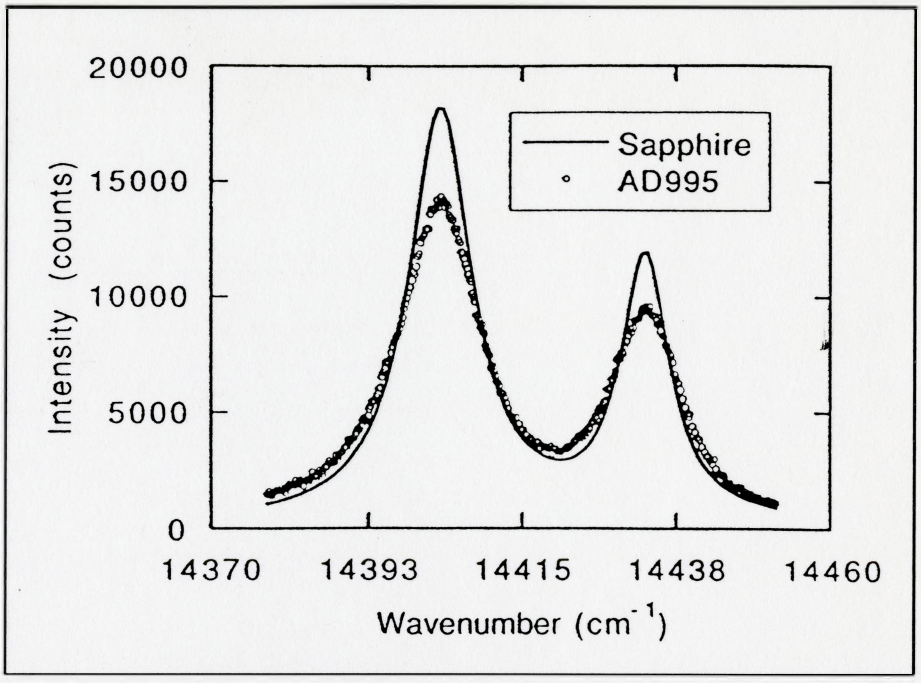

Figure 2.18 The fluorescence spectra measured for sapphire and polycrystalline Al_2O_3 (Ma and Clarke, 1993).

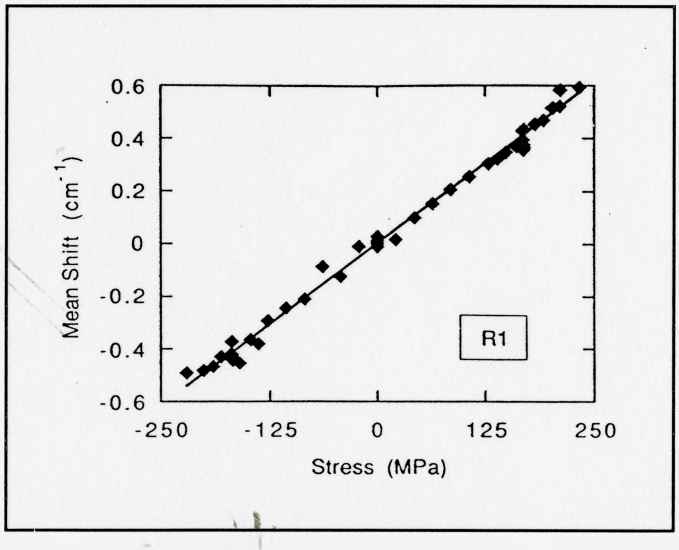

Figure 2.19 The peak shift ($\Delta\nu$) measured for the R1 fluorescence line of polycrystalline Al_2O_3 under an applied stress (Ma and Clarke, 1993).

Al_2O_3 (Ma and Clarke, 1993).

In a polycrystal the fluorescence signal is assumed to originate from a large number of randomly oriented grains. The associated frequency shift was derived by Ma and Clarke (1993) by integrating the product of $\Delta\nu$ and an orientation probability function, $P(\theta,\phi,\psi)$, in three dimensions, ie;

$$\overline{\Delta\nu} = \iiint P(\theta,\phi,\psi)\Delta\nu\, d\theta\, d\phi\, d\psi \qquad (2.31)$$

to give an average $\Delta\nu$,

$$\Delta\nu = \frac{1}{3}(\Pi_{11} + \Pi_{22} + \Pi_{33})(\sigma_{11} + \sigma_{22} + \sigma_{33}) \qquad (2.32)$$

Thus, the frequency shift in a polycrystal can only be related to the average *hydrostatic* stress, ie; $\sigma_{hyd}=1/3(\sigma_{11}+\sigma_{22}+\sigma_{33})$.

$\Delta\nu$ is calculated by measuring the fluorescence from the unknown sample Al_2O_3 (ν_s) and that of an Al_2O_3 standard with no macrostress (ν_o), then taking the difference, ie;

$$\Delta\nu = \nu_s - \nu_o \qquad (2.33)$$

The argon ion laser (514 nm wavelength) within a Raman spectrometer is used to excite the Cr^{3+} fluorescence in Al_2O_3 . The 'probe volume' is a measure of the depth of measurement within the sample. This depth varies from 50-200 μm for Al_2O_3, depending on the amount of optical scattering in the microstructure (Clarke, 1998). Lipkin and Clarke (1995) discuss the relationship between a finite probe size and spacial property gradients at the surface. A 'probe response function' must be measured by experimental calibration to determine the measurement sensitivity as a function of depth. This calibration used to separate the influence of sampling sensitivity from those of property gradients in the material, such as localized stress gradients.

Sergo *et al.* (1997) measured the tensile edge stresses in laminates of Al_2O_3 and Al_2O_3+Y-TZP using fluorescence piezospectroscopy. The depth resolution of the fluorescence measurements was determined using a laminated sample with the surface ground at an angle to the layering plane. The measured probe response functions for Al_2O_3 and Al_2O_3+Y-TZP **(Figure 2.20)** indicate a maximum sensitivity in Al_2O_3 at $\approx 10\mu m$.

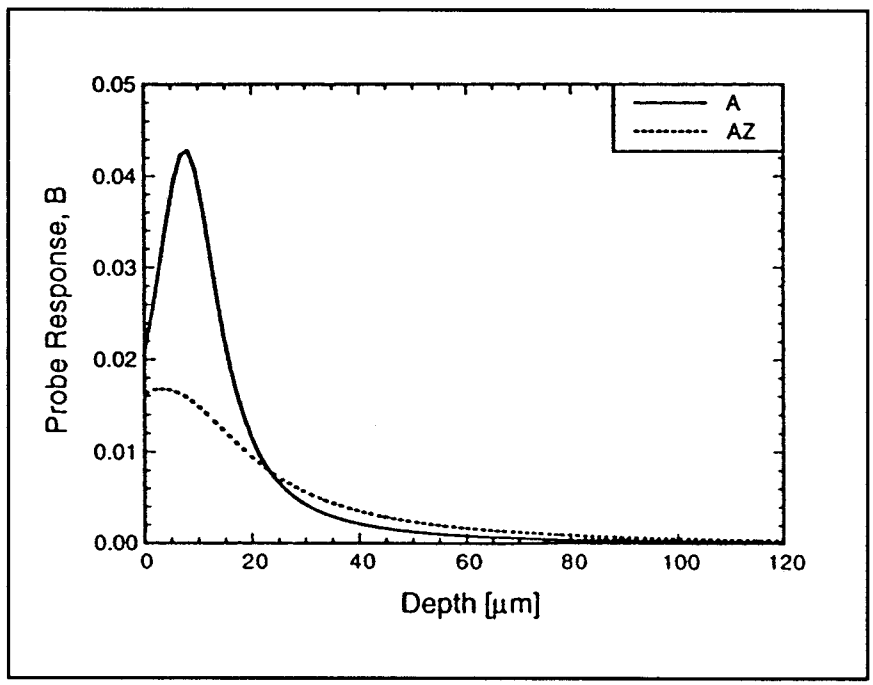

Figure 2.20 The probe response functions measured for monolithic Al_2O_3 and Al_2O_3+ZrO_2 (Sergo *et al.*, 1997).

2.4 The Fracture of Layered Ceramic Composites

2.4.1 The Influence of Elastic Mismatch Between Layers

The stress intensity acting on a crack in an elastic, layered composite is influenced by the difference in the elastic properties of the layers.

Hilton and Sih (1971) calculated the stress intensity factors for a single tunnel crack in various orientations within the centre layer of a three layer laminate. The crack system and layer geometry used in their model are shown in **Figure 2.21**, where μ is the shear modulus, and ν is Poissons ratio. The influence of crack size, position, layer thickness and stiffness ratio of the two layered materials on the stress intensity were calculated using a numerical solution to the differential equations of equilibrium and compatability. **Figure 2.22** shows the change in (normalized) K_I for different values of the crack size (normalized to the layer thickness, **h**) and for different values of the shear moduli μ_1 and μ_2.

Lu and Erdogan (1983) modelled the elastic strain energy of an edge crack oriented perpendicularly to the interface of two bonded isotropic layers with an applied bending moment (**Figure 2.23**). **Figure 2.24** shows the results for K_I (normalized) as a function of normalized crack length with different compliance ratios for the two layers. The solid lines are the results for $\mu_1 = 3\ \mu_2$ (approaching a stiffer layer), and the dashed lines for $\mu_1 = \mu_2/3$.

In both studies, the Mode-I stress intensity for a crack decreases steadily as the crack tip approaches a layer of higher elastic modulus. From the point of view of layered composite design, incorporating layers of higher stiffness *reduces* the driving force for cracks propagating normal to the interface.

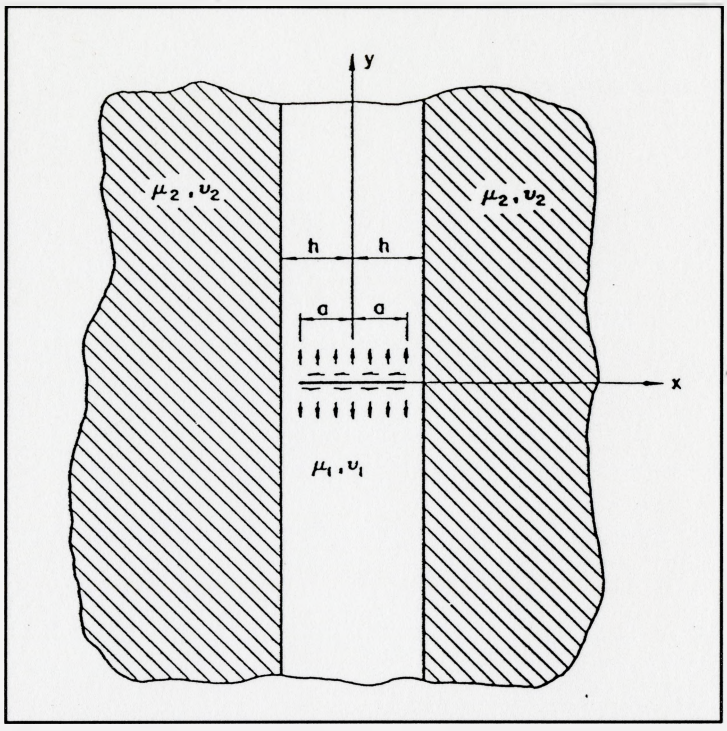

Figure 2.21 Schematic model used by Hilton and Sih (1971) of a crack within a layered composite.

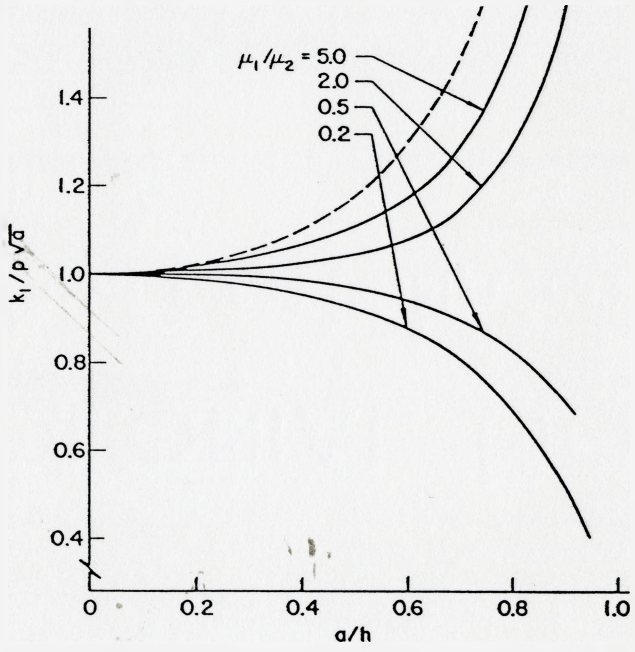

Figure 2.22 The normalized mode-I stress intensity as a function of c/t, for different elastic modulus ratios (Hilton and Sih, 1971).

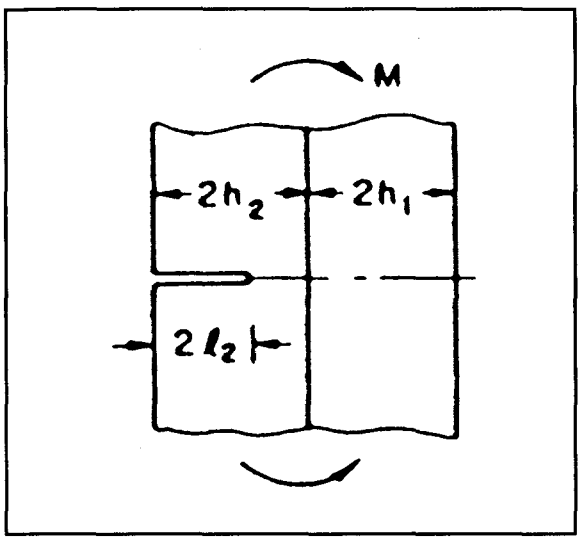

Figure 2.23 Schematic model used by Lu and Erdogan (1983) of a surface crack in a layered composite under an applied bending moment.

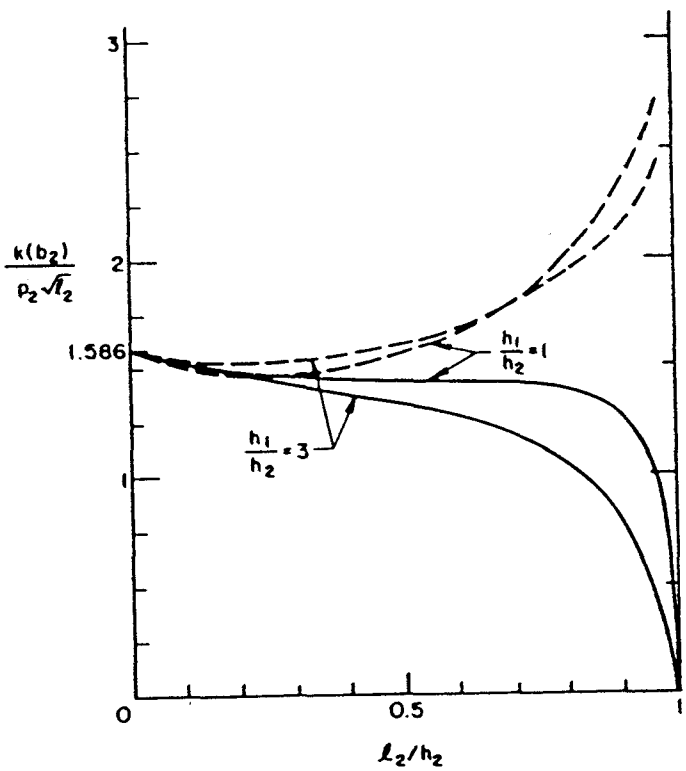

Figure 2.24 The normalized mode-I stress intensity as a function of c/t, for different elastic modulus ratios (Lu and Erdogan, 1983).

2.4.2 Models of Crack Deflection in Layered Composites

The conditions for crack deflection were discussed in Section 2.1.3. In two-phase, layered composites, the interface between two dissimilar layers can be a source of weakness and deflect cracks. He and Hutchinson (1989) used a model crack system to determine the conditions necessary to deflect a crack along the interface between dissimilar elastic materials (in terms of Equation 2.19; p.11). He *et al.* (1994) investigated the influence of residual stress on deflection along an interface for the same crack system model as He and Hutchinson (1989). Residual stress in a composite can arise from differences in thermal expansion between layers of different materials (Section 2.3.1).

The model in He *et al.* (1994) consisted of a crack perpendicular to a layer with its tip at the interface (see **Figure 2.25**). The residual stress (σ_t) acting within the layer ahead of the crack tip is normalized (using Equation 2.11) to define a non-dimensional parameter, η_t, given by,

$$\eta_t = \frac{\sigma_t a_d^{1/2}}{k_I} \qquad (2.34)$$

where $\mathbf{k_I}$ is the local stress intensity for the deflected crack and $\mathbf{a_d}$ is the length of the *initial* deflected crack. The latter can be interpreted as the inherent grain size (Marshall *et al.*, 1997). The elastic mismatch between the two layers is described by the Dundurs parameter, α, given by,

$$\alpha = \frac{\bar{E}_1 - \bar{E}_2}{\bar{E}_1 + \bar{E}_2} \qquad (2.35)$$

where $\bar{E} = E/(1-\nu^2)$.

The conditions necessary for penetration through, or deflection (debonding) along, the interface, are shown in **Figure 2.26** in terms of α and the residual stress parameter η_t.

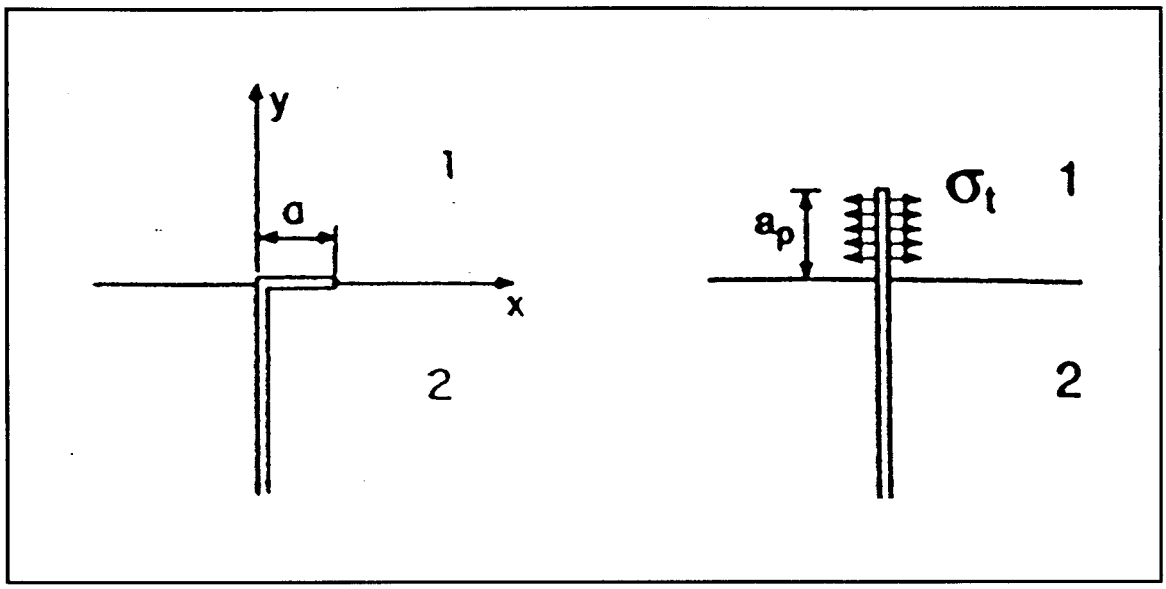

Figure 2.25 A schematic model of a crack with its tip at the interface between two materials, representing (a) penetration to the next layer, or (b) deflection along the interface (He *et al.*, 1994).

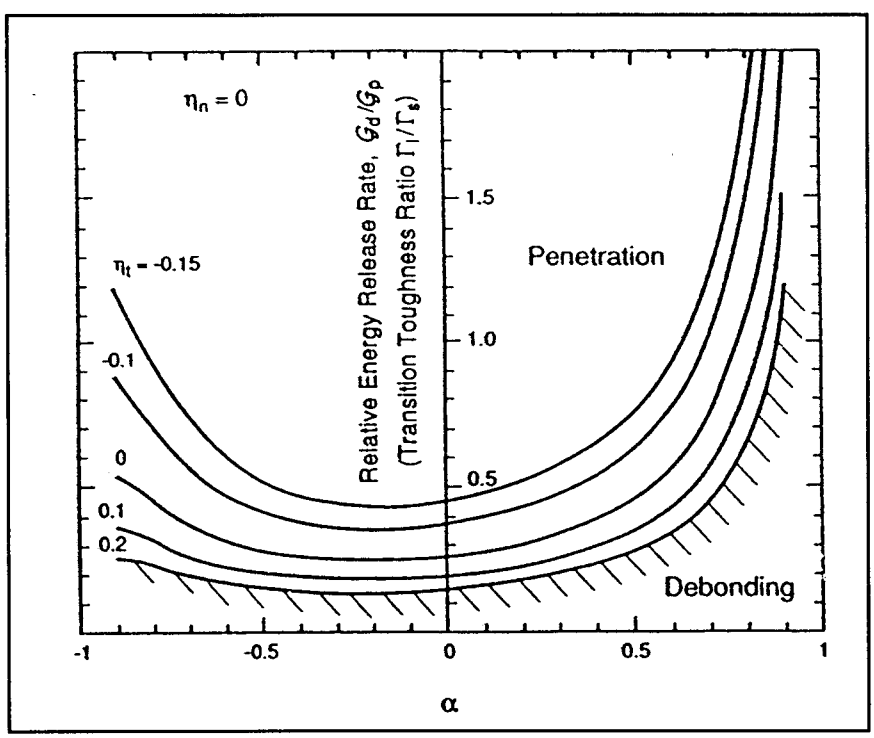

Figure 2.26 The energy release ratio as a function of α for various values of η_t (He *et al.*, 1994).

Clearly, a large negative value of η_t (ie; *compressive* stress) will increase the driving force for crack deflection along the layer interface. He *et al.* point out that deflection is possible for strongly bonded interfaces (where $R_i \approx R_s$) with sufficiently large compressive stress.

Lu (1996) modelled the branching of a parent crack *within* a layer of an isotropic composite due to compressive residual stress therein. The non-dimensional parameter $E\Omega/\sigma_\infty$ (where $\Omega = (\alpha_1-\alpha_2)\Delta T$) is used as a measure of the magnitude of the thermal residual stress, $E\Omega$, relative to the uniform applied stress, σ_∞. **Figure 2.27** shows the geometry Lu used to model the 'parent' and 'branch' crack. Branch cracks of length L propagate perpendicular to the parent crack in the matrix phase.

In this model, there is no weak interface present to direct the crack sideways (ie; $R_i \approx R_s$). The ratio G_θ/G_s from Equation 2.19 (or G_h/G_b in his terminology) is calculated as the driving force for crack deflection, such that $G_h/G_b > 1$ is sufficient to the grow the branch cracks. **Figure 2.28** is a graph of G_h/G_b versus the (normalized) deflected crack length (L/h_b). These curves indicate a maximum in G_h/G_b over short branch crack lengths. As a result, unstable cracks will branch sideways, but will be stabilized again if G_h/G_b decreases below unity. For $E\Omega/\sigma_\infty \geq 3.8$ the G_h/G_b curve is sufficiently high to cause branch crack propagation at all lengths. For $E\Omega/\sigma_\infty \leq 3$ the driving force for branch cracking is very low after the initial crack deflection.

2.4.3 Transformation Zone Modifications in PSZ Layers

Marshall *et al.* (1991) demonstrated that 35μm Al_2O_3 (mixed with Ce-TZP) layers in a Ce-TZP matrix can modify the size and shape of the transformation zone ahead of a crack. They synthesized multilayered composites using a centrifugal slip-casting technique to deposit layers of 100% Ce-TZP, and layers of mixed Ce-ZrO_2 +Al_2O_3. After initiating a sharp pre-crack, samples

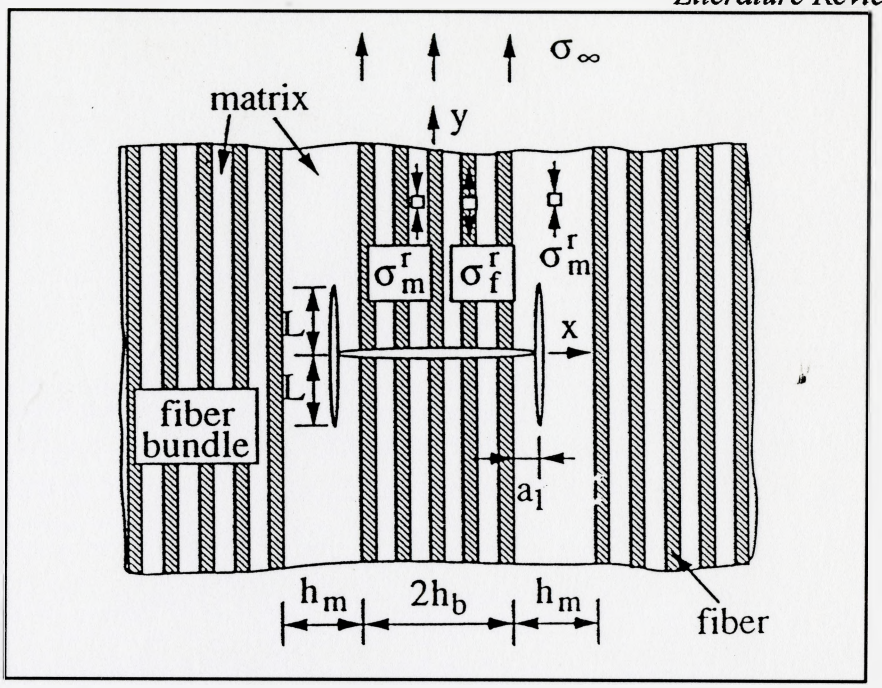

Figure 2.27 The model used by Lu (1996) of a crack in a layered composite with branch cracks extended into the 'matrix' phase.

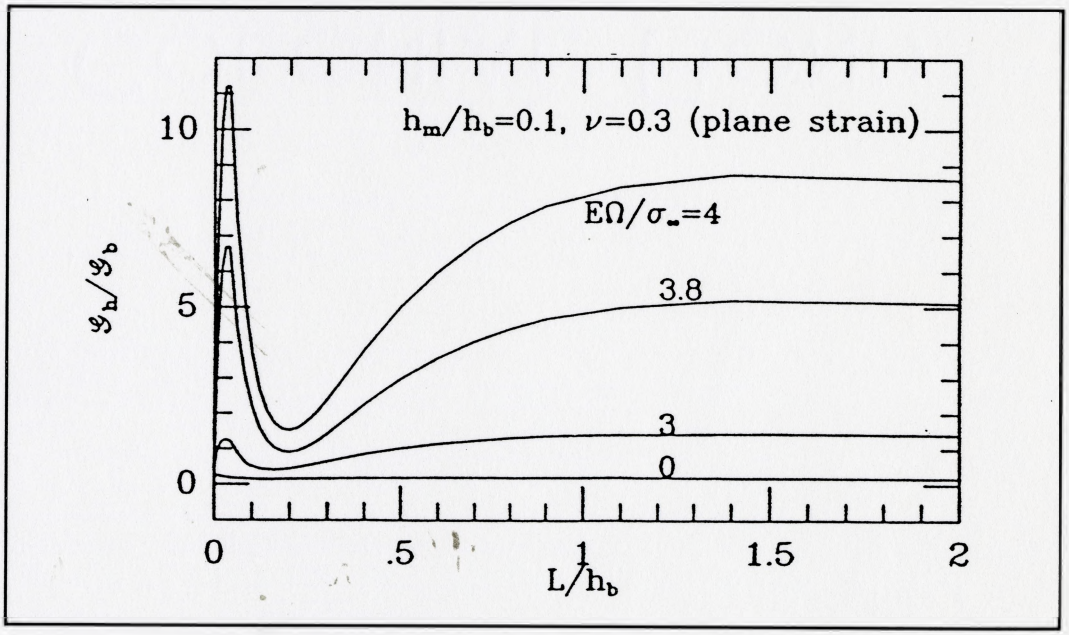

Figure 2.28 Energy release rate ratios calculated for branch cracks as a function of (normalized) crack length (Lu, 1996).

were tested in 4-point bending and crack propagation was observed *in situ* using a Normarski interference microscope.

The elongated transformation zone normally found in monolithic Ce-TZP was broadened as cracks approached layers of Ce-TZP +Al_2O_3. Crack arrest was caused by the increased size of the transformation zone at the crack tip (lowering K_{net}). As the crack propagated through several closely spaced layers, they observed stable crack growth as the transformation zone (and T) continued to increase (**Figure 2.29**). K_{net} was calculated by simultaneously measuring the crack length and applied stress (Equation 2.11; p.5), to determine the R-curve (or T-curve, as shown in Figure 2.2 b; p.8). The toughness was found to increase from 5 to 17.5 $MPam^{1/2}$ as a result of the closely spaced layers (**Figure 2.30**), before unstable crack growth.

2.4.4 Cracks in Thin Layers with Residual Stress

The evolution of biaxial residual stresses in layered composites was discussed in Section 2.3.1. The elastic strain energy stored in a layer of area, **A**, and thickness, **t**, is given by;

$$U_m = \frac{\sigma_r^{\,2}}{E'} At \qquad (2.36)$$

The strain energy release rate (Equation 2.3; p.3) for a crack within the layer, is derived from Equation 2.36 to be,

$$G = \frac{Z\sigma_r^{\,2} t}{E'} \qquad (2.37)$$

where **Z** is a dimensionless parameter which defines the driving force for different crack geometries (Hutchinson and Suo, 1992). In Equation 2.37, crack propagation is steady-state, since G is

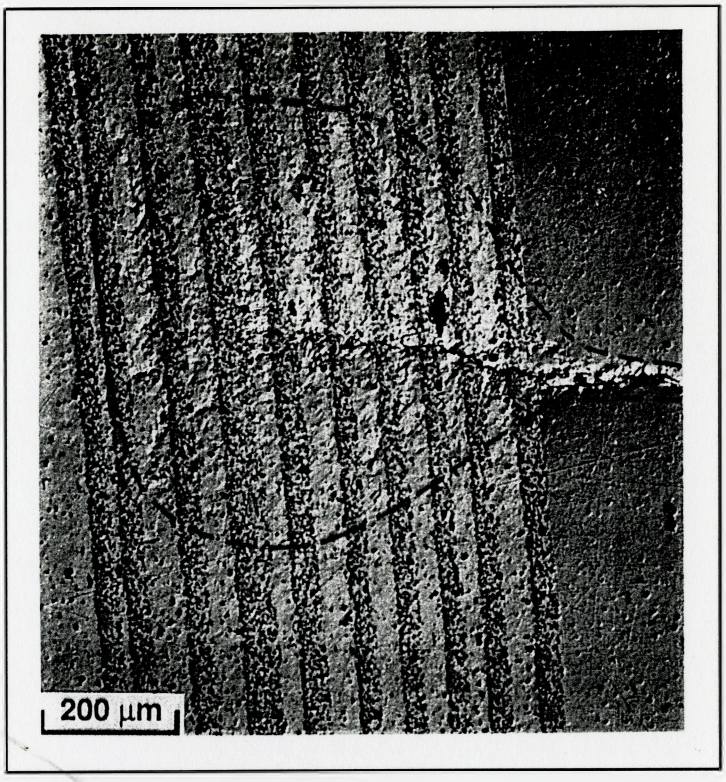

Figure 2.29 The widening of the transformation zone ahead of a crack propagating through a series of Al_2O_3+ZrO_2 layers (Marshall *et al.*, 1991).

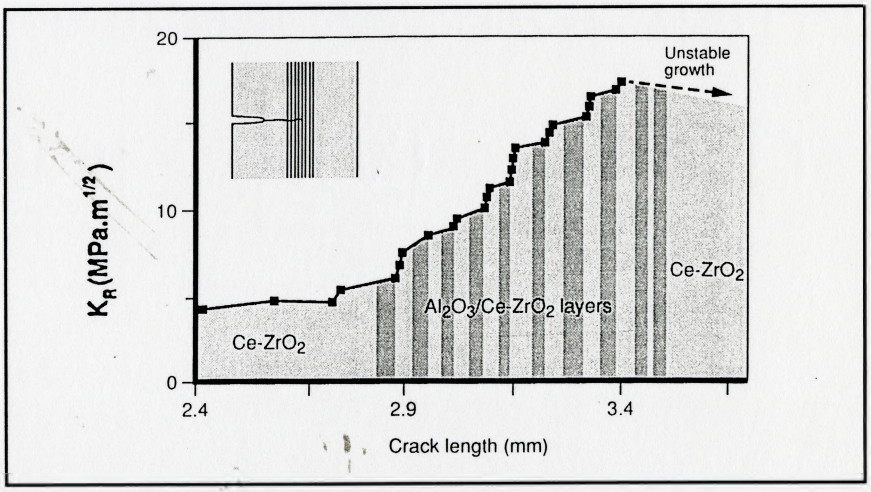

Figure 2.30 R-curve (T-curve) measurements for a crack propagating through a series of Al_2O_3+ZrO_2 layers (Marshall *et al.*, 1991).

independent of the crack size, **c**. *Thin* layers can be distinguished from *thick* layers via the c/t ratio. If c/t is large, the energy release rate achieves steady-state and is defined by the layer thickness. If c/t « 1, the layer thickness is significantly larger than the crack size and G is proportional to c (ie; **t** should be replaced by **c** in Equation 2.37). Equation 2.37 applies to fracture within *localized* stress fields in various composite materials, such as around reinforcing particles (Davidge and Green, 1969; Lange, 1973) and within thin layers (Hutchinson and Suo, 1992).

Equation 2.37 suggests there is a critical layer thickness *below* which fracture will not occur for a given stress and fracture resistance. The critical layer thickness is given by;

$$t_c = \frac{R_o E'}{Z\sigma_r^2} \qquad (2.38)$$

Tensile stresses (σ_{yy}) exist locally at the free surface of layers under biaxial compressive residual stress (Section 2.3.1). Ho *et al.* (1995) discuss the conditions for the propagation of edge cracks along the edge of thin layers due to local tensile stress. Edge cracks propagate by *edging* and *channeling* (**Figure 2.31**). The strain energy release rate for edging, G_{ED}, is defined by;

$$\frac{G_{ED}E'}{\sigma_M^2 t} = \pi \frac{a}{t} s^2 \left\{1.122 - (1-s)[0.296 + 0.25s^{3/4}(0.75-s)]\right\}^2 \qquad (2.39)$$

where $s = 2/\pi \tan^{-1}(t/2a)$ (from Tada *et al.*, 1985) and σ_M was defined in Figure 2.16; p.29. G_{ED} is plotted in **Figure 2.32** (normalized using Equation 2.37) as a function of a/t (Ho *et al.*, 1995). G_{ED} reaches a maximum with crack length at a/t ≈0.3, and then decreases because of the rapid decrease in $\sigma_{yy}(x)$ (Figure 2.17; p.30). As a result, edge cracks are stabilized a short distance into the layer.

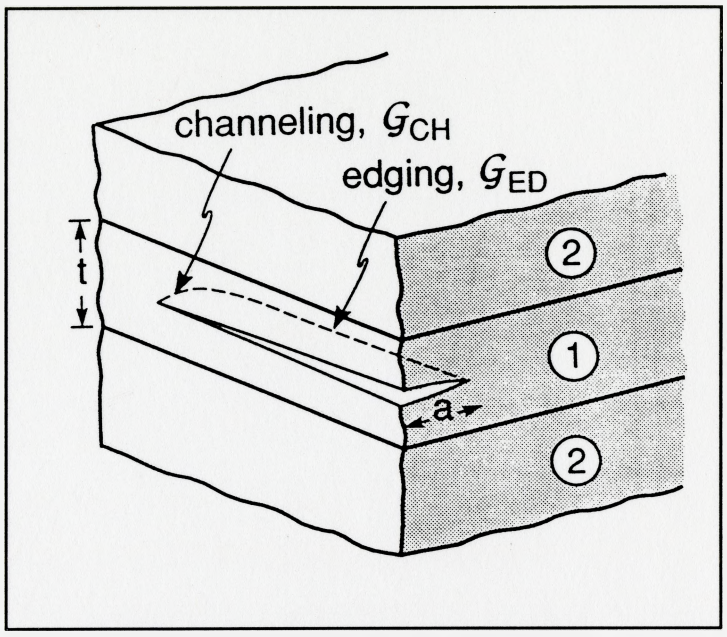

Figure 2.31 Schematic of *edging* and *channeling* at the surface of a layer (Ho *et al.*, 1995).

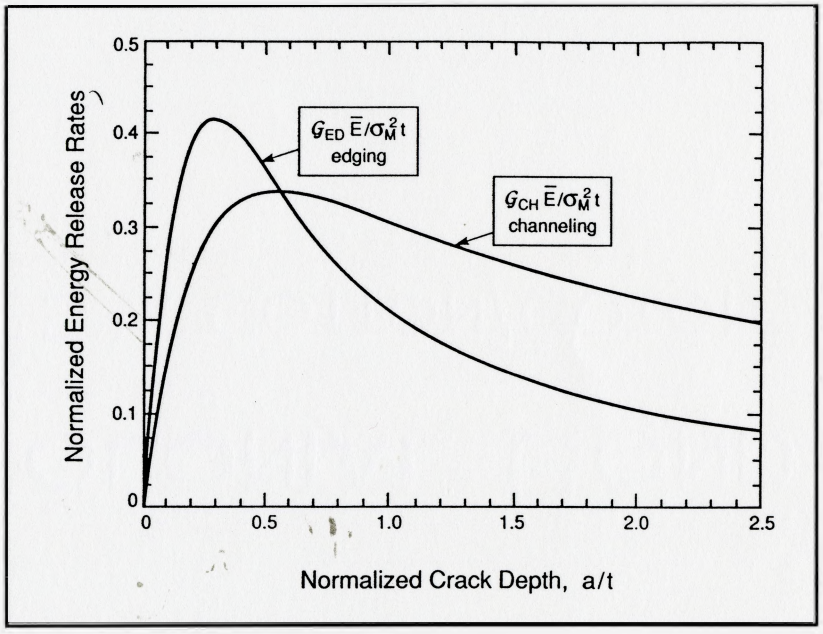

Figure 2.32 Strain energy release rates for edging and channeling (Ho *et al.*, 1995).

2.4.5 Layered Ceramic Composites with Residual Stress

Compressive residual stresses around a Mode-I crack in a solid reduce K_{net} (Equation 2.13; 5). Surface compression is used very effectively to increase the strength of monolithic ceramics, eg; physically or chemically tempered glass (Kelly and MacMillan, 1986; Kingery, 1976). Examples of surface compression in PSZ include surface grinding (Garvie et al., 1975; Gupta, 1980), and the removal of the stabilizing agent (Y_2O_3 or CeO_2) by heat treatment (Green, 1983), to produce m-ZrO_2 in the surface layers. Tandon and Green (1991) used models of parabolic residual stress profiles to show that the stabilization of fracture is only possible when the *maximum* compressive stress is away from the surface. Therefore, a *gradient* in surface compression, such as for monolithic PSZ, increases the apparent strength but there is no chance for stable crack growth prior to failure. Layered ceramic composites have biaxial residual stresses which are uniform across each layer (Equations 2.28; p.26). Past studies of layered ceramic composites include designs with compressive layers at the surface or the interior.

2.4.5.1 Compressive Layers at the Surface

Hansen *et al.* (1988) used the ISB technique (Section 2.1.1) to compare the strength and flaw tolerance of three-layer laminates of Al_2O_3-15%ZrO_2, containing unstabilized ZrO_2 in the outer layers for residual compression. The 4-point bend indentation-strength results are shown in **Figure 2.33** (plotted in terms of $P^{-1/3}$) for the composite and monolithic layers. The apparent strength of the composites was greater than the monolith by ≈500 M Pa over the entire range of P. There is no significant flaw tolerance in the composite material since the slope in Figure 2.33 is very similar that for monolithic Al_2O_3-15%ZrO_2.

She *et al.* (1998) measured the flaw tolerance of three-layer laminates of Al_2O_3+mullite (outer layers) and ZrO_2+Al_2O_3 (inner layer) using the ISB technique. The lower thermal expansion

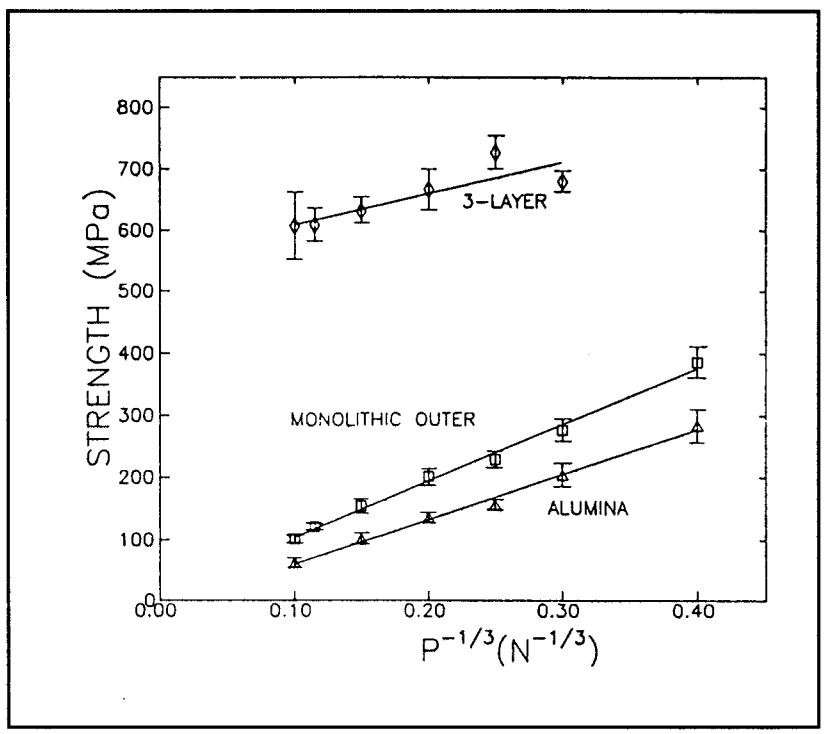

Figure 2.33 Indentation-strength results for the layered composite, monolithic Al_2O_3+15vol% ZrO_2 (tetragonal) and monolithic Al_2O_3 (Hansen *et al.*, 1988).

coefficient of mullite resulted in residual compression in the outer layers. The ISB results show a flaw tolerance in the laminated composite as compared to monolithic ZrO_2+Al_2O_3 (**Figure 2.34**). The slope of the data for the composite samples is close to zero, indicating that the strength is independent of the indentation load. They suggest failure did not originate at the indentation site (as the outer layer was in compression) and instead initiated from the interface between the layers.

2.4.5.2 Compressive Layers within Composites

Compressive layers within a composite can cause crack arrest or deflection by influencing the driving force for propagation normal to the layer. Prakash et al. (1995) evaluated the strength in 4-point bending of multilayer composites of Al_2O_3 and TZ3Y prepared by electrophoretic deposition (EPD). The properties of laminates containing Al_2O_3 layers in TZ3Y (5vol% Al_2O_3), and TZ3Y layers in Al_2O_3 (5vol% TZ3Y), were compared to monolithic Al_2O_3 and TZ3Y. The layering design was not discussed, but the Al_2O_3 layer thickness was ≈ 10 μm in the 5 vol% Al_2O_3 composite. Different coefficients of thermal expansion cause compression in the Al_2O_3 layers and tension in the TZ3Y layers. A fractured sample indicated crack deflection 'steps' at the Al_2O_3 layers (**Figure 2.35**) due to the compressive residual stress therein (calculated to be ≈800 MPa). The strength of the 5vol%Al_2O_3 composite was close to monolithic TZ3Y (950 MPa) and the specific energy of fracture was improved due to crack deflection at the layers.

Oechsner *et al.* (1996) investigated the role of Al_2O_3 layer thickness on the fracture behaviour of a Al_2O_3 / Ce-ZrO_2 layered composite in 4-point bend. Laminates were fabricated by tape casting and pressureless sintering. The Al_2O_3 layers within the composites had thickness 33 to 100 μm and the Ce-ZrO_2 layers ~ 800 μm. The biaxial compressive stress in the Al_2O_3 layers was found to be ≈2 GPa, via piezospectroscopic stress measurement (Section 2.3.2). Significant *bifurcation* (double deflection) was observed through the centre of the Al_2O_3 layers of thickness

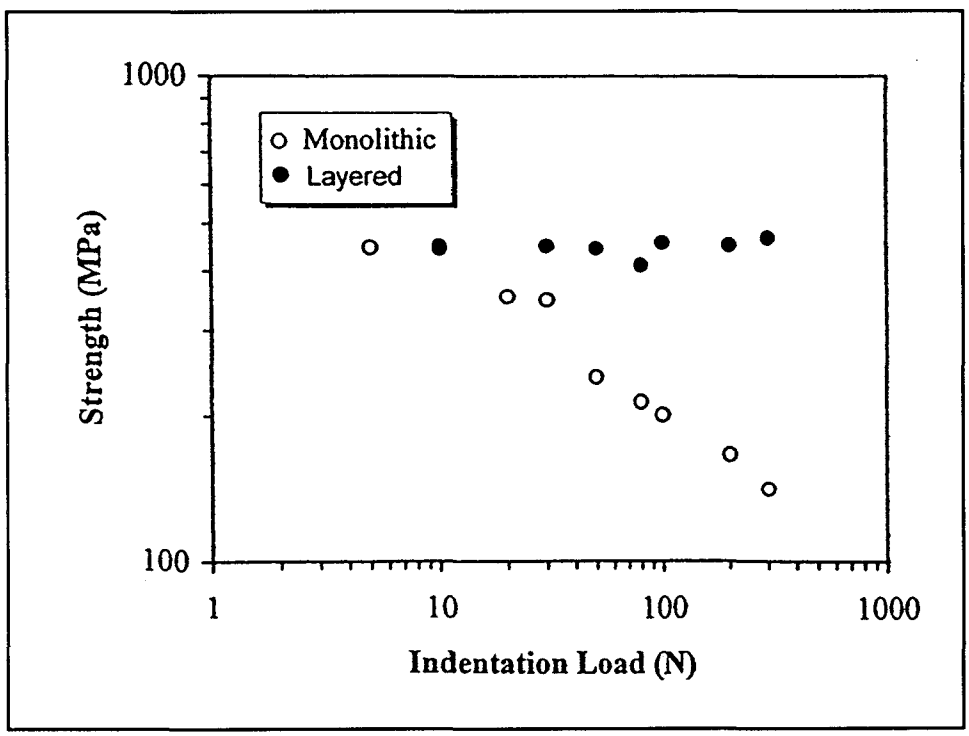

Figure 2.34 Indentation-strength results for the layered composite and monolithic Al_2O_3+ZrO_2 (She *et al.*, 1998).

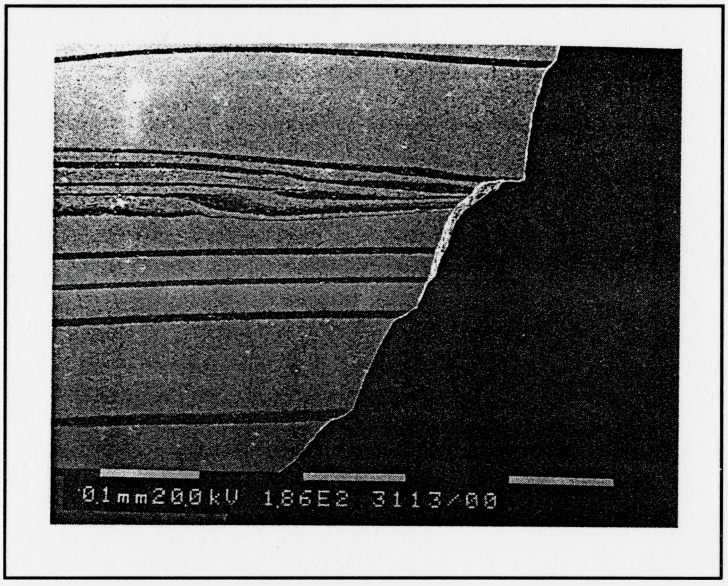

Figure 2.35 Cross-section of a fractured sample (5vol%Al_2O_3) indicating deflection steps (Prakash *et al*, 1995).

70-76 μm (**Figure 2.36**). Crack propagation was stable when approaching the Al_2O_3 layers (as also observed in Marshall *et al.* 1991). As a result, the fracture test could be stopped at various times during fracture (**Figure 2.37**). Bifurcation was *not* observed in Al_2O_3 layers < 70 μm (**Figure 2.38**). All laminates fabricated with Al_2O_3 layers ≥ 90 μm delaminated during sample preparation. They proposed the bifurcation mechanism is related to the phenomenon of edge-cracking along the edge of compressed layers (in this case Al_2O_3). This phenomena is known to be scale dependent (Section 2.4.4).

Free surfaces are created as a perpendicular crack penetrates an Al_2O_3 layer (**Figure 2.39**) and the constraint of the surrounding material is released to produce localized tensile stresses normal to the layer plane (ie; Figure 2.15; p.29). The tensile stresses cause the parent crack to bifurcate and continue to propagate along the centre of the Al_2O_3 layer. The driving force for the bifurcated cracks is of the same form as for edge cracks (Equation 2.37; p.43). As a result, the Al_2O_3 layer must be a minimum thickness to cause bifurcation (Equation 2.38; p.45). The critical minimum Al_2O_3 thickness for *edge cracking* was calculated to be ~ 18 um and edge cracks were observed in all Al_2O_3 layers ≥33μm. The minimum layer thickness for bifurcation is expected to be different than for edge cracking, since the crack geometry is different.

Sánchez-Herencia *et al.* (1998) used three-layer composites of m-ZrO_2 (outer layers) and mixed m-ZrO_2 + t-ZrO_2 (inner layer) to further test the bifurcation mechanism suggested by Oechsner *et al.* (1996). The tetragonal to monoclinic transformation during cooling caused large compressive, residual stress within the single layer of mixed m-ZrO_2 + t-ZrO_2 . The magnitude of this stress depends on the composition and thickness of the centre m-ZrO_2 + t-ZrO_2 layer. Several composites were made by sequential slip casting with the mixed layer containing 30 to100 vol% m-ZrO_2 and thickness 5 to 150 μm. Samples were loaded in 4-point bend and the fracture behaviour is shown in **Figure 2.40**. Samples with layer thickness > 175 μm and large MZ % (high residual stress) delaminated spontaneously during processing. Those with layer thickness < 75 μm, and low

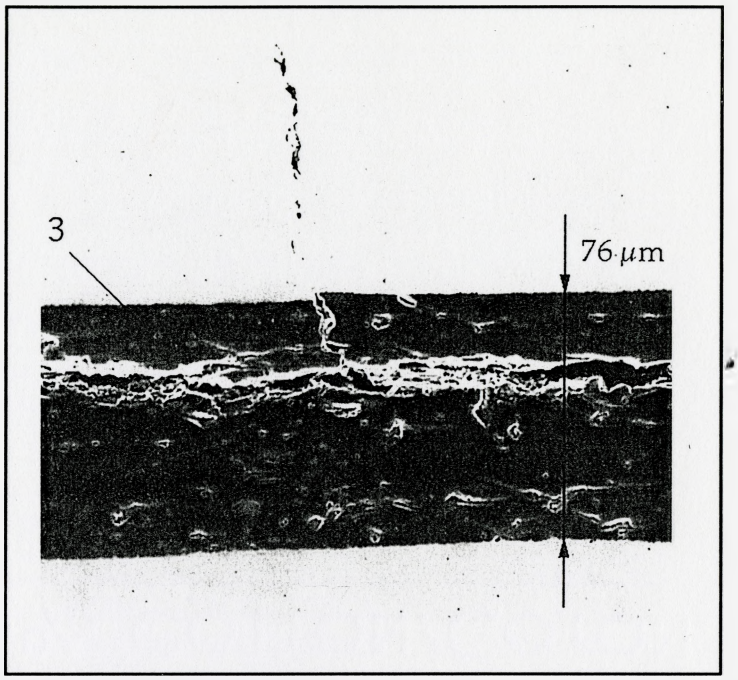

Figure 2.36 Crack bifurcation through a 76 μm Al_2O_3 layer (Oechsner *et al.*, 1996).

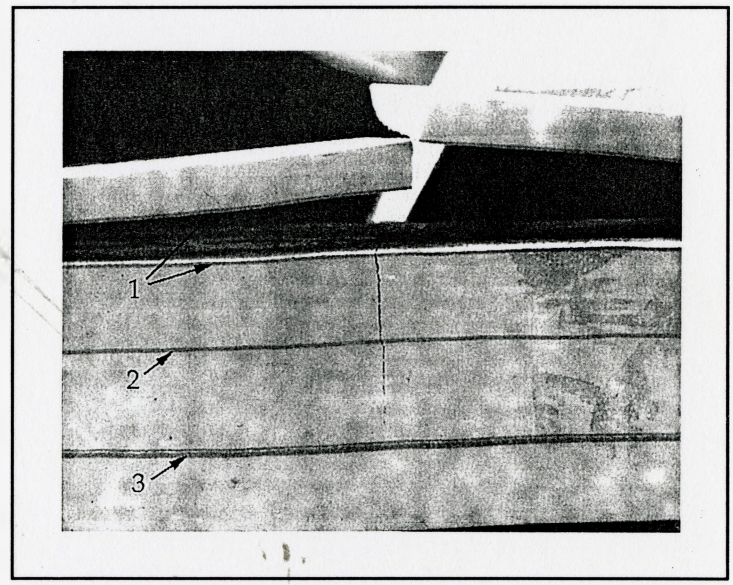

Figure 2.37 Partial fracture of the layered Al_2O_3/Ce-TZP composite (Oechsner *et al.*, 1996).

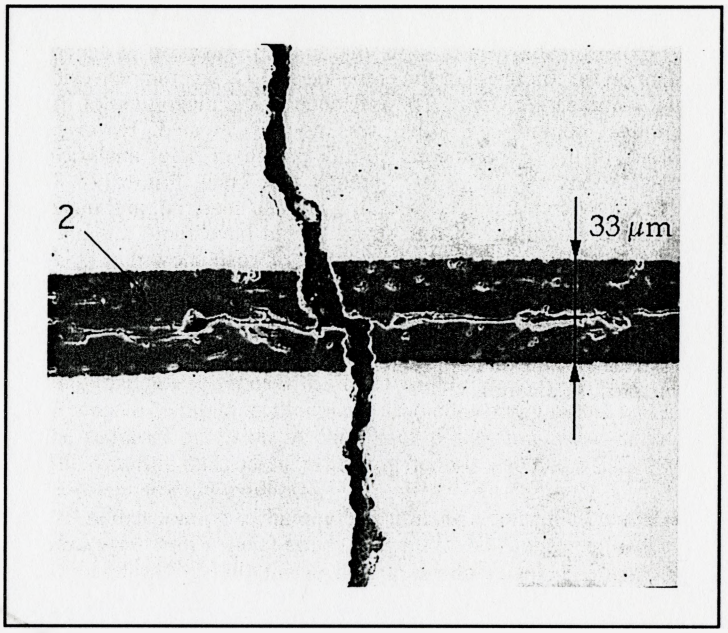

Figure 2.38 Crack penetration through a 33 μm Al_2O_3 layer (edge crack in Al_2O_3) (Oechsner *et al.*, 1996).

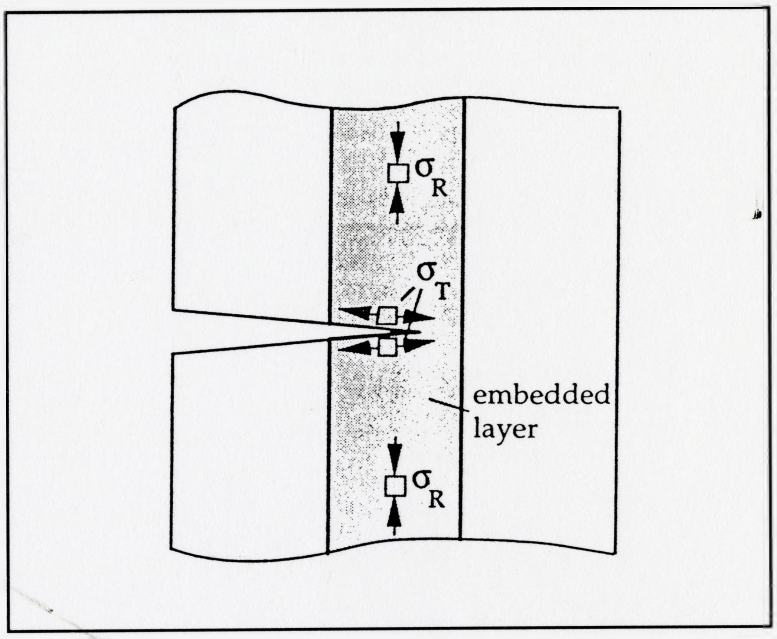

Figure 2.39 Schematic diagram of the tensile stresses at the newly formed crack surface (Oechsner *et al.*, 1996).

MZ% (low residual stress) showed no edge cracking or crack bifurcation. The remaining samples exhibited both bifurcation and edge cracks. **Figure 2.41** shows a sample with crack deflection along a compressed centre layer.

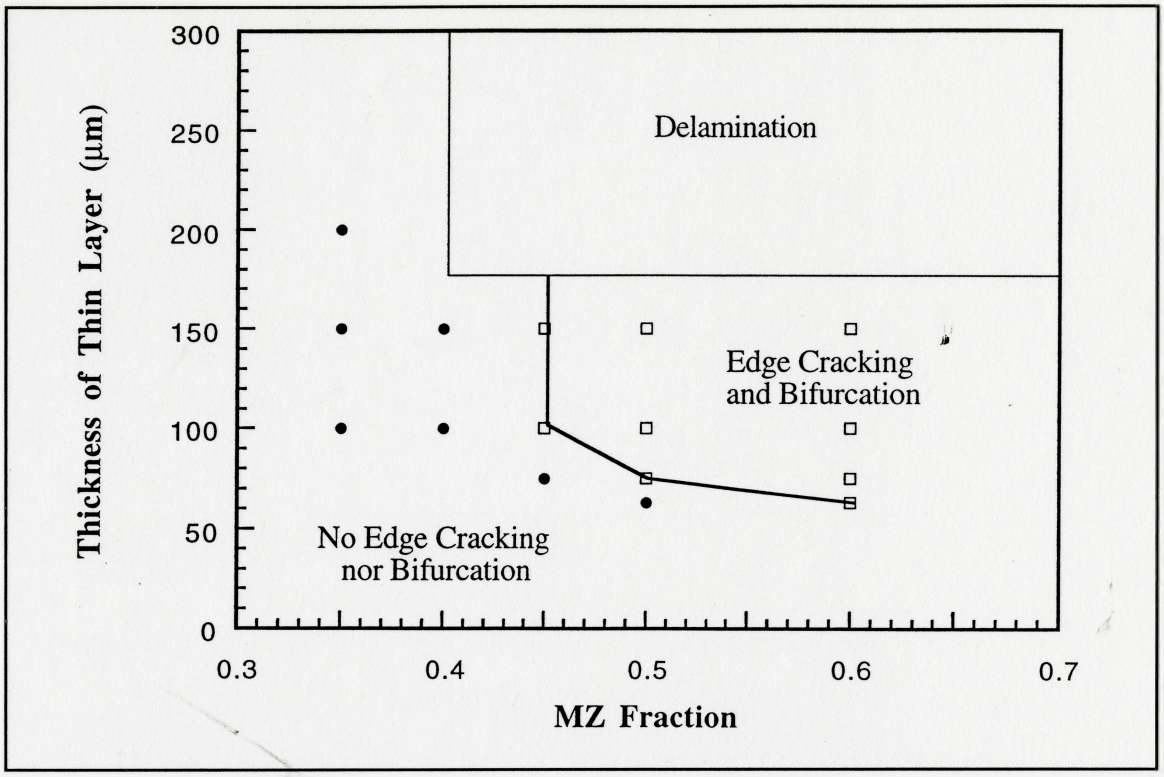

Figure 2.40 Map of fracture behaviour in terms of layer thickness and m-ZrO_2 volume fraction (Sánchez-Herencia, 1998).

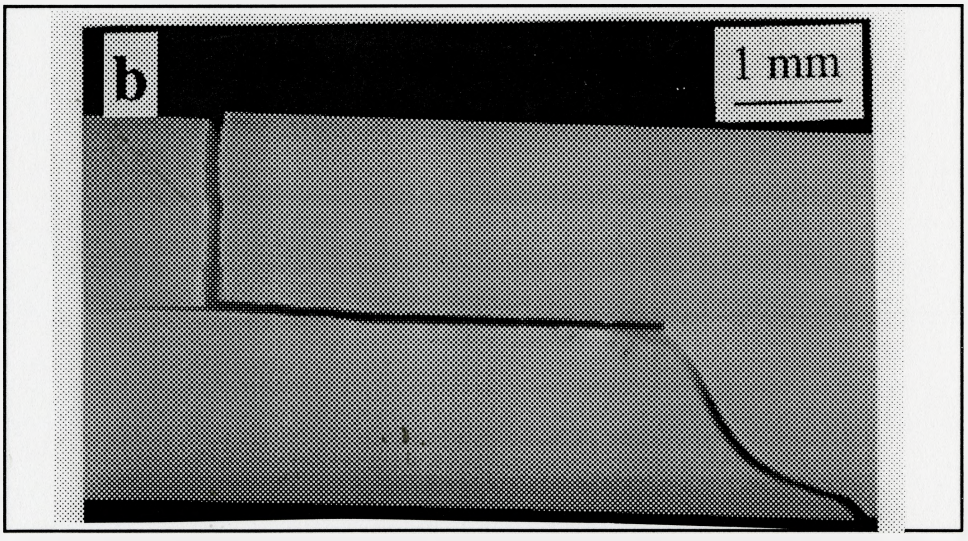

Figure 2.41 Cross-section of a fractured sample showing crack bifurcation at the m-ZrO_2 layer (Sánchez-Herencia, 1998).

2.5 Electrophoretic Deposition (EPD)

2.5.1 Mechanisms of EPD

Electrophoretic deposition (EPD) is a useful technique for shaping ceramics into layered composites. Ceramic particles with surface charge in a colloidal suspension move in an applied electric field (electrophoresis) and deposit onto the oppositely-charged electrode.

Colloidal particles in suspension can develop surface charge by several means. One mechanism is the dissociation or ionization of surface groups. In the case of oxide particles, surface reactions involve amphoteric hydroxl groups which depend on the pH of the suspension. The latter can be written (Sarkar and Nicholson, 1996);

$(M\text{-}OH)^0_{surface} + H^+ \rightleftharpoons (M\text{-}OH_2)^+_{surface}$ (Low pH) (2.40a)

$(M\text{-}OH)^0_{surface} + OH^- \rightleftharpoons (M\text{-}O)^-_{surface}$ (High pH) (2.40b)

Ions of opposite charge surround a particle in suspension as a result of this surface charge. The combination of the charged particle and this 'double layer' of counterions is known as the *lyosphere*. If an electric field is applied, the particles move towards the electrode of opposite charge, the lyosphere is distorted and a 'shear' layer develops. The difference in potential between this shear layer surface and the particle surface is known as the *zeta potential* (ζ).

The DLVO theory is useful to model the stability of charged particles in suspension, which follows the work of Derjaguin and Landau (1941), and Verwey and Overbeek (1948). The model is based on the balance between the energy of attraction and repulsion between particles. The attraction between two particles is based on the London-van der Waals electrostatic attraction energy (V_A) which is given by;

$$V_A = -\frac{A}{6D}\frac{r_1 r_2}{r_1 + r_2} \qquad (2.41)$$

where **A** is the Hamaker constant, **D** is the separation distance between particles, and $\mathbf{r_1}$ and $\mathbf{r_2}$ are the particle radii. There is a repulsive force between two particles of the same charge if the two ionic double layers overlap and increase the free energy (decrease in ionic entropy). The osmotic pressure which develops because of increased ionic concentration between the particles, exerts an ionic repulsion energy (V_R). The magnitude of V_R is a function of the zeta-potential. The addition of V_A and V_R over distance from the particle surface causes a 'potential energy barrier' (V_{max}) to develop at intermediate distances between the particles (**Figure 2.42**). The local energy maximum keeps colloidal suspensions stable. During deposition, particles are forced to coagulate in a dense mass at the surface of a charged electrode. For deposition to occur, particles must overcome the energy barrier in Figure 2.42. A proposed mechanism of deposition is that co-ions (suspension ions with the same sign as the particles) discharge, locally increasing the pH and flocculating the particles (De and Nicholson, 1998).

In general, the dielectric constant of the suspension medium should be as high as possible. Although H_2O has a high dielectric constant ($e \approx 80$), it electrolyses in the dc field producing bubbles at the electrode surface. Therefore organic liquids such as methanol, ethanol, propanol, or acetone are generally used (Sarkar and Nicholson, 1996).

2.5.2 The EPD of Layered Composites

Layered ceramic composites were first produced using EPD by the McMaster Ceramic Engineering Research Group.

Sarkar *et al.* (1992) and Nicholson *et al.* (1993) used EPD to produce Al_2O_3/TZ3Y multilayer composites. Al_2O_3 and ZrO_2 are well suited to EPD since they have common surface charge characteristics. The zeta potential-pH curves for Al_2O_3 and ZrO_2 (TZ3Y) in ethanol have been measured by Wang (1994) and are shown in **Figure 2.43**. Both Al_2O_3 and ZrO_2 have a positive surface charge at pH < 5.0, ie; they can both deposit on electrodes of the same sign.

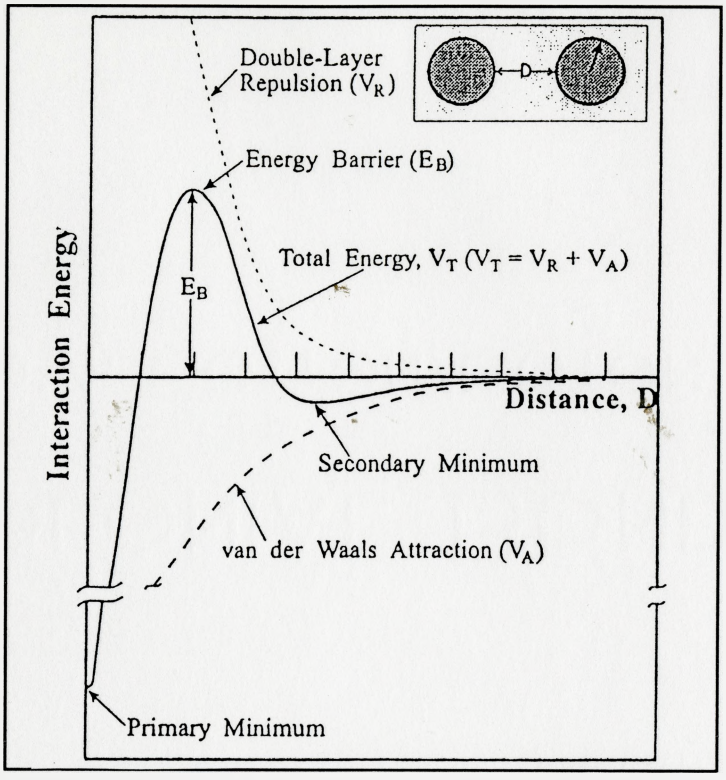

Figure 2.42 The interaction energy as a function of the separation distance, D, between particles (Sarkar and Nicholson, 1996)

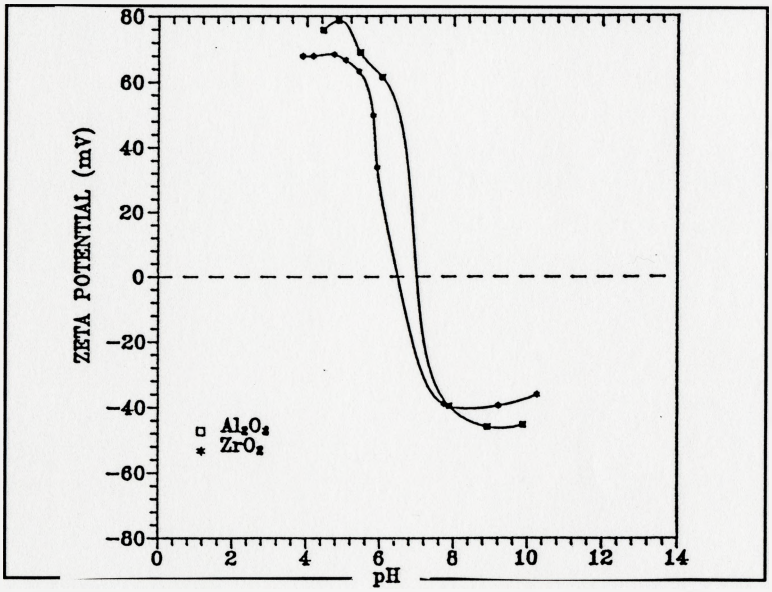

Figure 2.43 Zeta potential measurements for Al_2O_3 and ZrO_2 as a function of pH (Wang, 1994)

Deposits were made using 10wt% suspensions of Al_2O_3 and TZ3Y in ethanol (pH≈3.5) onto graphite electrodes. Laminated deposits were synthesized by sequentially depositing Al_2O_3 and TZ3Y suspensions. Green deposits were ~ 60% dense. The composites were sintered in air at 1550°C for 6 hours. The Al_2O_3 and TZ3Y layers were 2 to 15 μm thick, with well-bonded interfaces, as illustrated in **Figure 2.44**.

The rates of deposition of Al_2O_3 and TZ3Y at different current densities are shown in **Figure 2.45** (Whitehead, 1994). The higher deposition rate of Al_2O_3 is attributed to its higher zeta potential.

Whitehead (1994) deposited Al_2O_3 and TZ3Y on conductive Au-coated Al_2O_3 fibres to make non-planar, laminated composites. Ritcey (1996) used EPD to control the layer thickness of 3-layer sandwich composites of Al_2O_3 and 8mol%Y_2O_3-ZrO_2.

Fischer *et al.* (1995) give an example of the use of EPD to fabricate Al_2O_3/TZ3Y multilayer composites from *aqueous* suspensions. Close inspection of their microstructures revealed pores and 'areas of imperfect deposition' due to gas evolution at the electrode.

Examples of the application of EPD to other materials include multilayer composites of TZ3Y and $LaAl_2O_4$ (Bissinger, 1995), mullite and SiC fibre preforms (Boccaccini and Ponton, 1995), and SiC with graphite interlayers (Vandeperre and Van Der Biest, 1998).

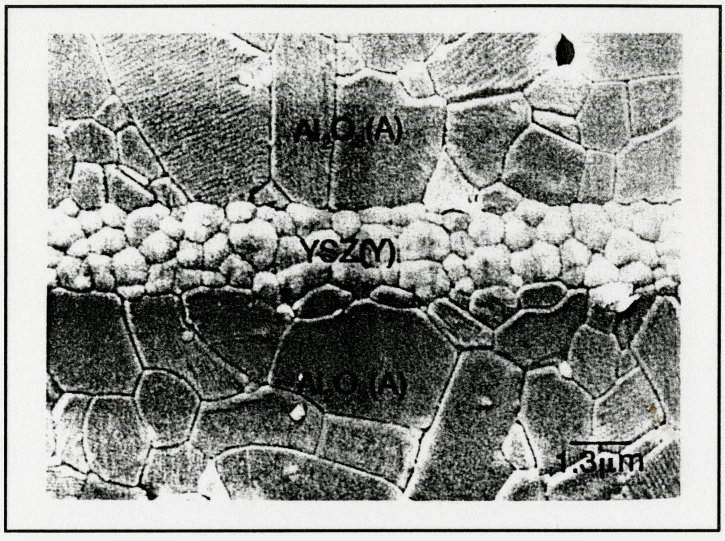

Figure 2.44 SEM micrograph of an Al_2O_3/TZ3Y layered composite (Sarkar *et al.*, 1992).

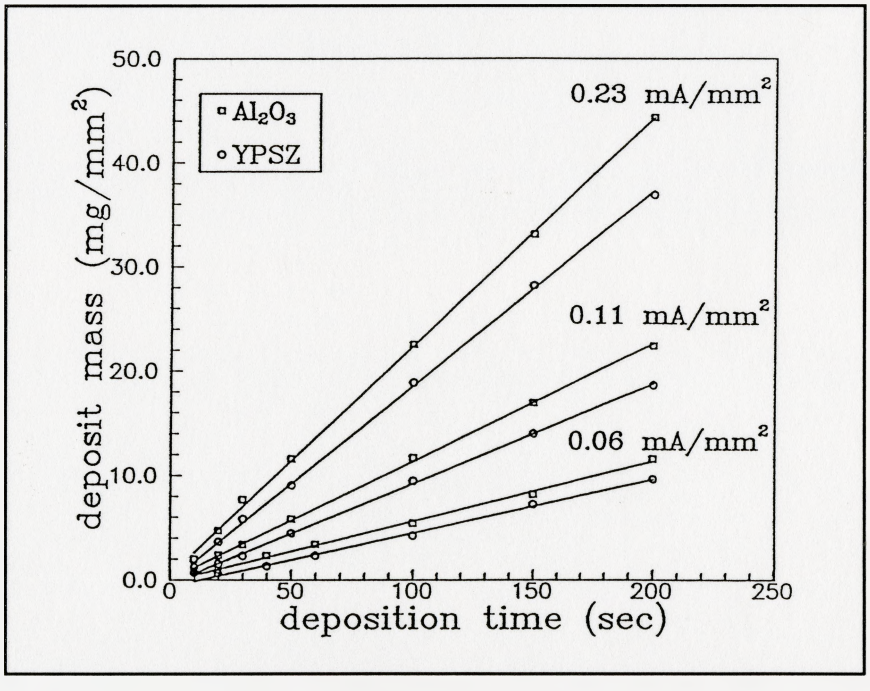

Figure 2.45 EPD deposition rates measured for Al_2O_3 and TZ3Y at different current densities (Whitehead, 1994).

Chapter 3: Experimental Procedure

3.1 The Synthesis of Multilayer Al_2O_3/TZ3Y Composites

3.1.1 EPD Processing

Multilayer composites of Al_2O_3 and 3mol%Y_2O_3-ZrO_2 (TZ3Y) were synthesized by EPD from colloidal suspensions in ethanol. The Al_2O_3 powder (AKP-50, Sumitomo Chemical Co. Ltd, Japan) had an average particle size of 0.26 ± 0.39 μm. The TZ3Y powder (Tosoh Corporation, Tokyo, Japan) had an average particle size of 0.17 ± 0.38 μm (Scott, 1997). Both powders were washed in distilled water and centrifuged at 4500 rpm (Beckman, GS-15) to remove ionic species absorbed on the surface. This washing was continued until the conductivity of the supernatant was close to that of distilled water (≈4μS). The clean powders were dried at 100°C for 24 hours and suspensions (~20 vol% solids) prepared in absolute ethanol and mixed in a vibromill with zirconia balls for 24 hours. The suspensions were then diluted to ~5 vol% solids for use in EPD. Both Al_2O_3 and TZ3Y acquire a positive charge for pH < 5.0 (Figure 2.37; p.54). The pH of the suspensions was adjusted to ~4.0 by adding 1:10 acetic acid/ethanol and 1:40 hydrochloric acid/ethanol solutions.

The EPD experimental setup is shown in **Figure 3.1.** The (depositing) cathode was a polished, stainless steel plate (2.5 x 3.5 cm) and the back face was covered in non-conductive plastic. A Ni plate was used as the anode. The separation between the electrodes was ~2 cm. A constant-current power supply (Keithley 237) supplied the potential for deposition. The steel electrode was initially coated with a thin layer of colloidal graphite to assist removal of the ceramic deposit after drying.

Deposition was carried out at 1-2 mA. The voltage increased from ~40 to 120 V due to

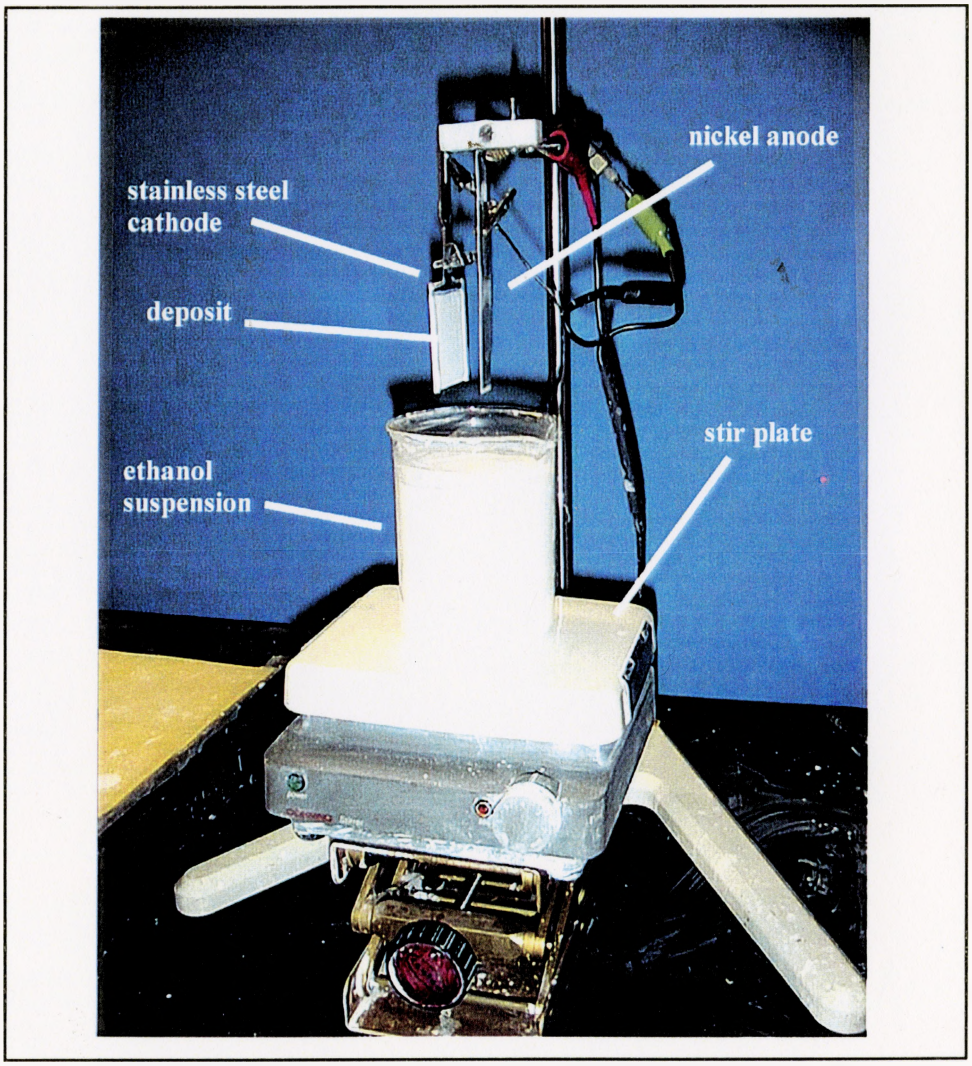

Figure 3.1 Experimental setup for electrophoretic deposition (EPD).

increasing deposit thickness. The electrodes were raised and the suspensions of Al_2O_3 and TZ3Y alternated to produce a layered composite. Deposits were 3-4 mm thick after 1-2 hours deposition, depending on the deposition rate and the laminate geometry.

The cathode (with the green deposit) was removed when the deposition was complete and placed inside a covered stainless steel chamber (see **Figure 3.2**). The chamber was immersed in liquid nitrogen to completely freeze the ethanol in the deposit to facilitate drying without cracking. Once frozen, the deposit was removed from the chamber and dried at room temperature in a covered glass dish for 2-3 days. Densification was achieved by pressureless sintering (1700S-E, CM Furnaces, Inc.) in air at 1550°C for 6 hours, with heating and cooling rates of 300°C/hour.

3.1.2 The Preparation of Fracture Samples

The sintered ceramic 'tiles' were cut into bars (2 x 2 x 25 mm) with a diamond-edged, high-speed saw. The samples were ground flat (Discoplan-TS, Struers Ltd.), then lapped on a polishing wheel (PM2, Logitech Ltd.) using 600 grit SiC. The sides were polished to 1 μm finish using diamond paste on polishing wheels. Finally, all samples were annealed at 1250°C for 2 hours (ramp 300°C/hour) to remove surface stresses caused by grinding and polishing. SEM samples were ground on a metal-bonded diamond wheel and a nylon wheel with colloidal diamond suspensions was used to polish to 0.1 μm (to avoid grain pullout of the Al_2O_3 layer).

Samples for grain size measurement and microstructure evaluation were thermally etched at 1250°C for 10 hours.

Sharp notches of constant depth were cut in eight samples of monolithic Al_2O_3 and TZ3Y and six samples of a multilayered composite (C15), by laser machining. The notches were cut in the monolithic samples for testing fracture toughness (Section 3.3.4), and in the laminated composites for *in situ* observation of crack propagation (Section 3.3.5).

A KrF laser (248 nm wavelength) was used (Lumonics Ltd., Kanata, Ontario) to cut

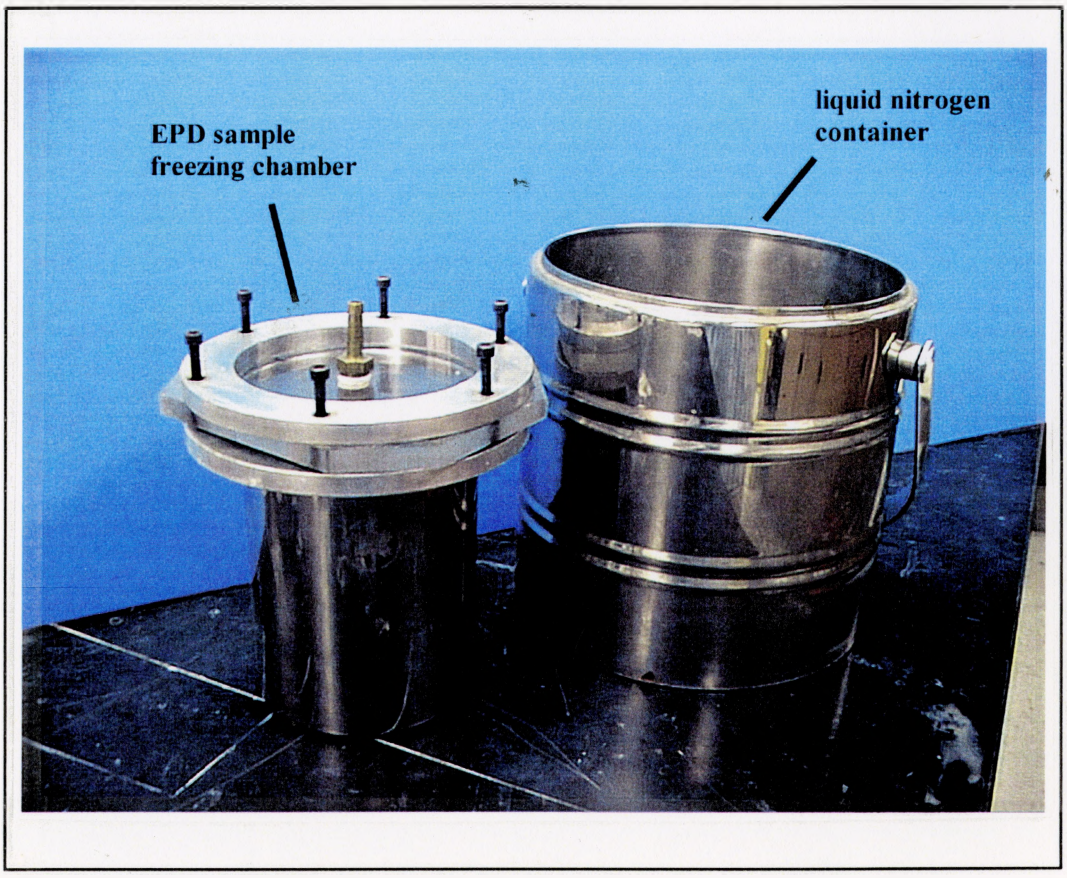

Figure 3.2 Stainless steel chamber for freezing ceramic deposits in liquid nitrogen.

across the width of the samples (perpendicular to the layer plane for composite samples) with a power density of ~ 14 J/cm^2. The notches were approximately triangular in cross-section with a surface width 20 - 50μm and depth 50 - 75μm. A micrograph of a notch cross-section in Al_2O_3 is shown in **Figure 3.3**. The samples were annealed at 1250°C for 2 hours to relieve residual stresses that may develop at the notch tip.

3.2 Material Characterization

3.2.1 The Measurement of Physical Properties

An ultrasonic technique was used to measure the elastic modulus (E) and Poisson ratio (ν) for the monolithic Al_2O_3 and TZ3Y samples. An ultrasonic transducer (5 MHz) reflected a transmitted signal from the opposite free surface of a sample and the 'time of flight' was measured using an oscilliscope. The longitudinal wave velocity (V_L) and the shear wave velocity (V_S) were calculated by;

$$V_L = \frac{2d}{T_L}$$
$$V_S = \frac{2d}{T_s} \qquad (3.1)$$

where $\mathbf{T_i}$ is the reflection time and **d** the sample thickness. The elastic constants were calculated by (Patel, 1997)

$$E = 2\rho V_S^2(1+\nu) \qquad (3.2a)$$

$$\nu = \frac{(V_L^2 - 2V_S^2)}{2(V_L^2 - V_S^2)} \qquad (3.2b)$$

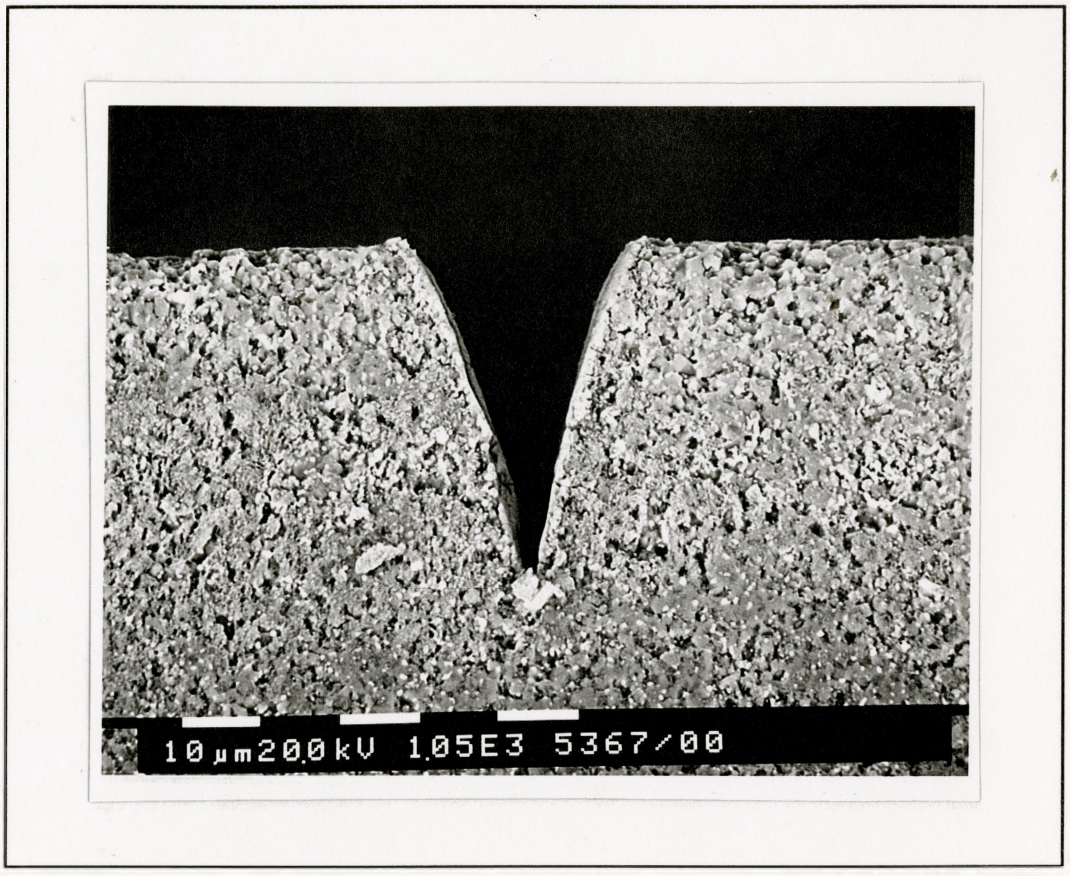

Figure 3.3 ESEM micrograph of cross-section of a notch machined by laser (1050 X) in Al_2O_3 (surface covered with debris).

The density (ρ) of the monolithic Al_2O_3 and TZ3Y materials was measured by the Archimedes principle in H_2O, ie;

$$\rho = \frac{W_d}{W_d - W_s} \times \rho_{H_2O} \qquad (3.3)$$

where W_d is the dry weight, W_s the weight submerged in water, and ρ_{H2O} the density of water (~ 1.0 g/cm^3).

3.2.2 Grain Size Measurement

The grain size of the TZ3Y and Al_2O_3 layers in the multilayered composites was measured using ASTM E112-96. The Hilliard circle method involves counting the number of grain boundary interceptions (N) on the circumference of a circle applied randomly to a polished microstructure. The circles should be large enough for at least 35 interceptions. The grain size parameter, L, for a circle of radius, r, is given by;

$$L = \frac{2\pi r}{N} \qquad (3.4)$$

3.2.3 Piezospectroscopic Residual Stress Measurements

A fluorescence spectroscopic technique (Section 2.3.2) was used to measure the residual stress in the Al_2O_3 layers of each multilayered composite. An argon ion laser (514 nm) within a Raman spectrometer (THR 1000, ISA Instruments SA, Inc.) was used to excite the fluorescence of the Cr^{3+} in Al_2O_3. The fluorescence was measured along the edge of the Al_2O_3 layers, ie; from the side of the sample (as illustrated in **Figure 3.4**).

An optical microscope on the Raman spectrometer facilitated accurate positioning of the

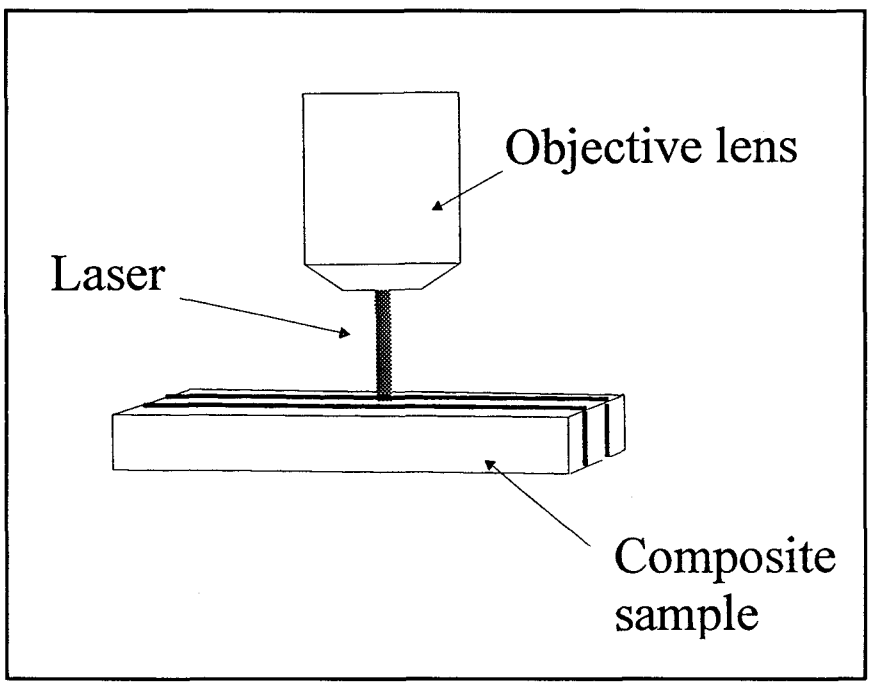

Figure 3.4 The orientation of fluorescence spectroscopy measurements on the edge of a layered composite sample.

laser spot on the sample surface. The laser spot size was assumed ~30 μm in diameter for the 10X objective lens (Ma and Clarke, 1993). Thus, it was assumed that a large number of grains were sampled in each measurement.

Fluorescence spectroscopy is sensitive to temperature so the power of the laser was minimized to avoid local heating of the sample surface (Ma and Clarke, 1993). Two spectroscopy measurements were made at the same position using 6 mW and 20 mW to test the effects of laser power. An insignificant difference was found in the measured frequency and the remainder of the measurements were made at 10mW. Variations of room temperature can cause instrumental shift so a neon lamp (2110QA2, Electrosonic) of wavenumber 14430 cm^{-1} was used as a characteristic wavelength. This standard was measured before and after each spectroscopy measurement (Ma and Clarke,1993).

The measured fluorescence spectra were fit to Lorentzian curves (using Origin 5.0 software) to identify exact R1 and R2 peak positions. The neon spectra were fit to Gaussian curves and the position of the R1 and R2 peaks located relative to the characteristic neon peak. Measurements of ν_s (Equation 2.32; p.33) were made using one or two samples from each multilayered composite and on Al_2O_3 layers near the midpoint of the sample cross-section. Four monolithic Al_2O_3 deposits (assumed to have no macroscopic residual stress) were tested to determine an average ν_o. Equation 2.33;p.33 was used to calculate the shift, $\Delta\nu$, of R1 and R2 for each sample. The average hydrostatic stress was calculated using Equation 2.28;p.26 from $\Delta\nu_{R1}$ and $\Delta\nu_{R2}$ and the appropriate piezospectroscopic coefficients (listed in Table 2.4; p.31).

3.3 Mechanical Testing

3.3.1 Indentation-Strength in Bending (ISB)

The indentation-strength in bending (ISB) technique (Section 2.1.1) was used to measure

the damage tolerance of the monolithic and composite samples. Indentation loads of 200 g to 20 kg were applied by a hardness testing machine (T 3212 B, Zwick Inc.) with a Vickers diamond. A micro-hardness machine (M-400-H2, Leco Ltd.) was used for indentation loads of 100 g. The strength in 4-point bending was tested immediately after indentation (**Figure 3.5**). An optical microscope confirmed failure initiated from the indentation site.

3.3.2 Flexural Strength at Room Temperature

4-point bend tests at 25 °C were performed at 0.100 mm/min using a screw-driven compression machine (Model 10053, Wykeham Farrance Engineering Ltd.), with compliance 0.5 μm/N (Huang and Nicholson, 1993). The 4-point bend apparatus (**Figure 3.6**) consisted of steel pins resting in grooves machined into stainless steel platens (top separation 10 mm, bottom separation 20 mm). A 500 lb load cell was used to record the applied load. A linear voltage displacement transducer (LVDT) was used to measure deflection. A data acquisition board was used to record the output of the load cell and the LVDT.

The stress on the ceramic sample (σ_a) was calculated using the standard relationship for modulus of rupture, ie;

$$\sigma_a = \frac{3}{4}\frac{LP}{bd^2} \qquad (3.5)$$

where **L** is the distance between the lower knife-edges (20 mm), **P** is the applied load, and **b** and **d** are the sample cross-sectional width and height, respectively (Anderson, 1995).

3.3.3 Flexural Strength at High Temperatures

The high temperature bend strength was measured in 4-point bending using a different screw-driven compression machine (**Figure 3.7**) (WF10055, Wykeham Farrance Engineering Ltd.),

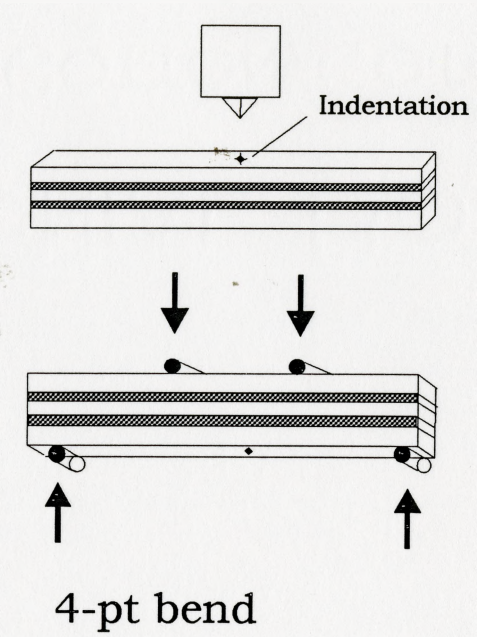

Figure 3.5 The indentation-strength in bending (ISB) technique; Vickers indentation followed by 4-point bend testing.

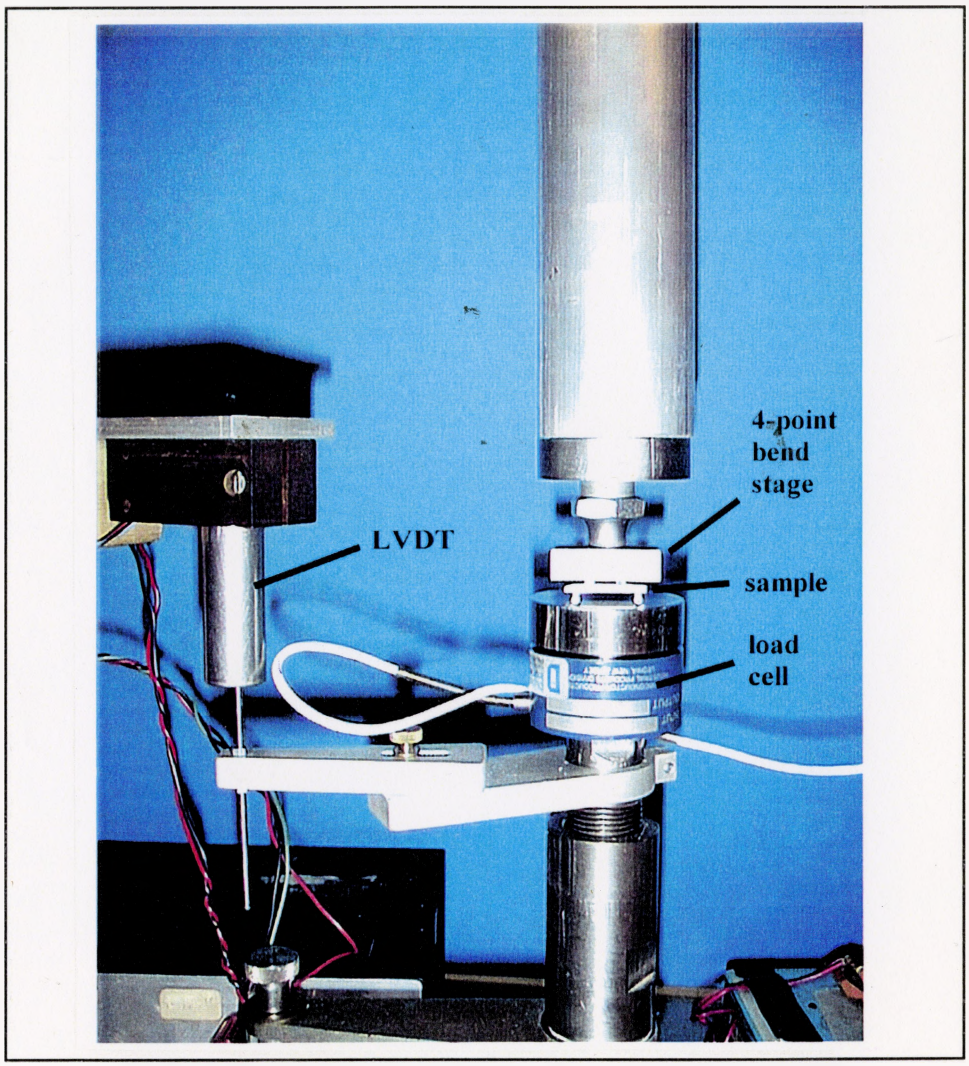

Figure 3.6 4-point bend stage for testing room temperature strength.

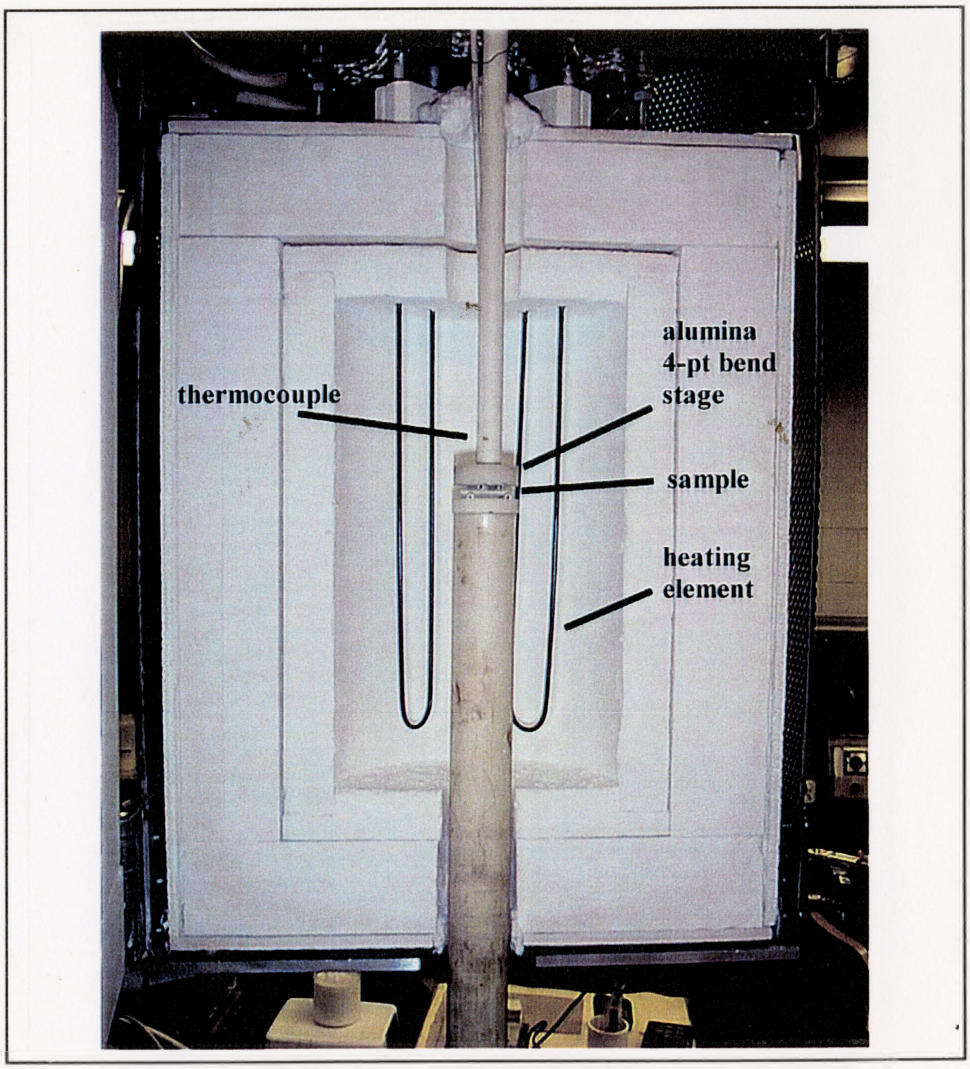

Figure 3.7 4-point bend stage and furnace for testing high temperature strength.

fitted with a 'clam-shell' $MoSi_2$-heating-element furnace (Zircar Products, Inc.). The 4-point bend apparatus was machined from alumina with the same testing dimensions as the low temperature unit. A schematic diagram of the high temperature testing equipment is shown in **Figure 3.8**. Thermal expansion of the test rig applies a load to the sample during heating to the test temperature and this can cause failure. Thus a feedback loop was used to maintain a low, *constant* load on the sample during heating. A program, compiled in C (see Appendix A), operated on a 386 PC and controlled the movement of the compression machine platen through a serial RS232 communication port. The sample was fixed with a low load (~6 N) before heating and a set-point voltage defined. During heating, the instantaneous load cell voltage was recorded (~1/s) via the data acquisition board. A speed was set for the downward motion of the platen, depending on the voltage *difference* from the set-point, until the set-point load was reached. Three speed settings (0.0100, 0.0250, and 0.0500 mm/min) were used. As a result, load limits were generally kept within ~10 N of the set-point load for heating rates of 7.5 to 10°C/min.

Test temperatures were 200°C to 1300°C. The furnace was allowed to stabilize for 20 minutes on reaching the required temperature. The 4-point bend test was performed at a cross-head speed 0.100-0.200 mm/min so failure occurred within 60 s. The data acquisition board was used to record the load cell and LVDT voltages. Indentation-strength (ISB) samples were indented (P = 10 kg) *prior* to heating to the test temperature.

3.3.4 Fracture Toughness Measurements

The fracture toughness of notched samples of Al_2O_3 and TZ3Y were tested in 4-point bending at room temperature. Sharp notches were used to minimize inaccuracies associated with blunt notches cut by diamond blades (Pabst, 1973). Samples were loaded to failure at 0.200 mm/min and the depth of the notch was measured from the fracture cross-section using an optical microscope. The toughness (T_o) was calculated knowing the fracture strength (σ_f) for a given notch

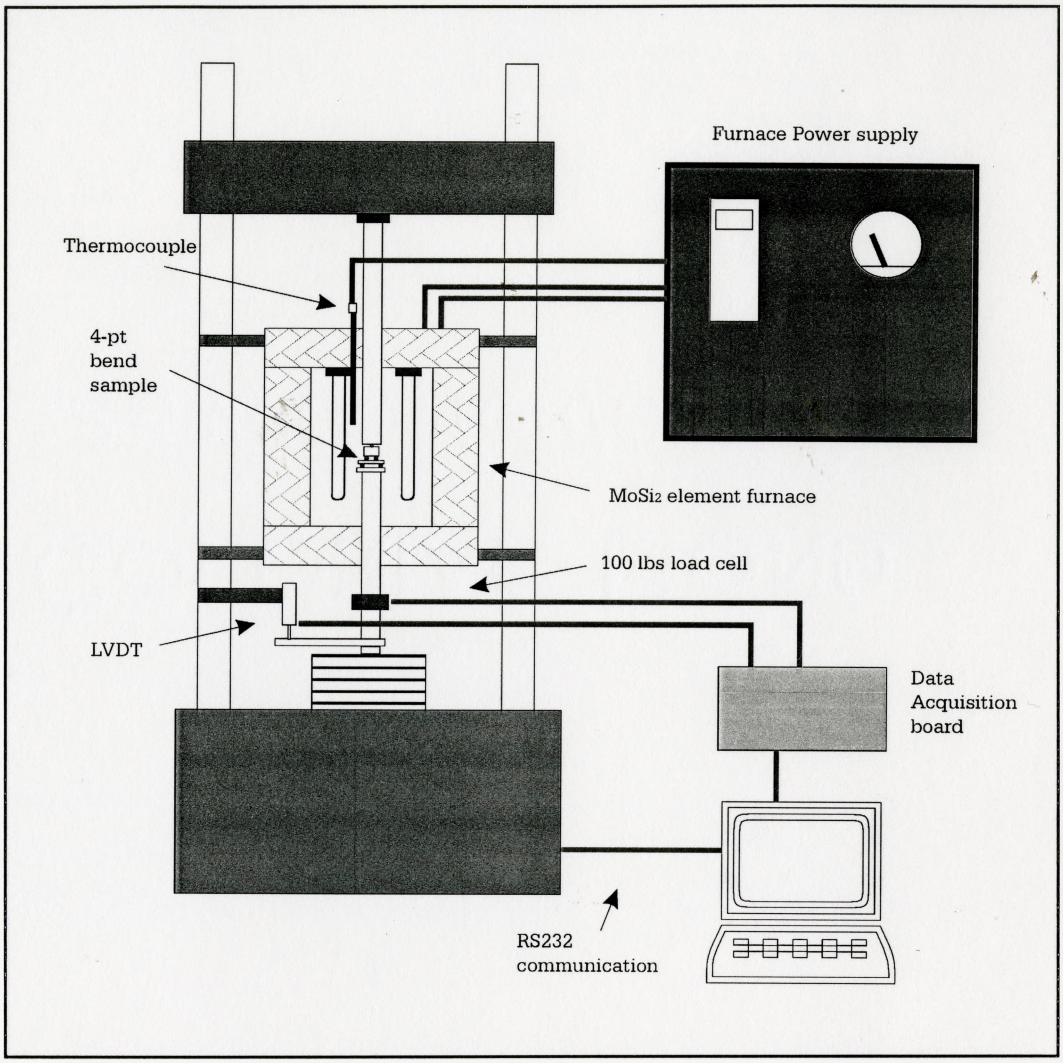

Figure 3.8 Schematic of experimental setup for heating to high temperatures.

length (c), ie;

$$T_o = K_{IC} = F(c/d)\sigma_f\sqrt{c} \qquad (3.6)$$

where **d** is the sample thickness and the geometrical function, F(c/d), is given by (Anderson, 1995), ie;

$$F(c/d) = [1.99 - 2.47(c/d) + 12.97(c/d)^2 - 23.17(c/d)^3 + 24(c/d)^4] \qquad (3.7)$$

3.3.5 *In Situ* Observations of Crack Propagation

It was necessary to observe samples *in situ* during fracture to detect stable crack growth *prior* to catastrophic failure. A 4-point compression stage designed to operate within an Environmental Scanning Electron Microscope (ESEM) (ES 2020, Philips Electroscan) was used to fracture multilayered Al_2O_3/TZ3Y composite samples. The 4-point bend stage was equipped with a 1000 lb load cell and an LVDT to measure deflection **(Figure 3.9)**. A data acquisition board was used to record the load and deflection during testing.

Six samples of composite C15 (37 μm Al_2O_3 layers, 48vol% Al_2O_3) were specially notched (Section 3.1.2) so the notch tip was known to be the initial source of fracture. Samples were loaded until stable cracks appeared at the notch tip or until catastrophic failure.

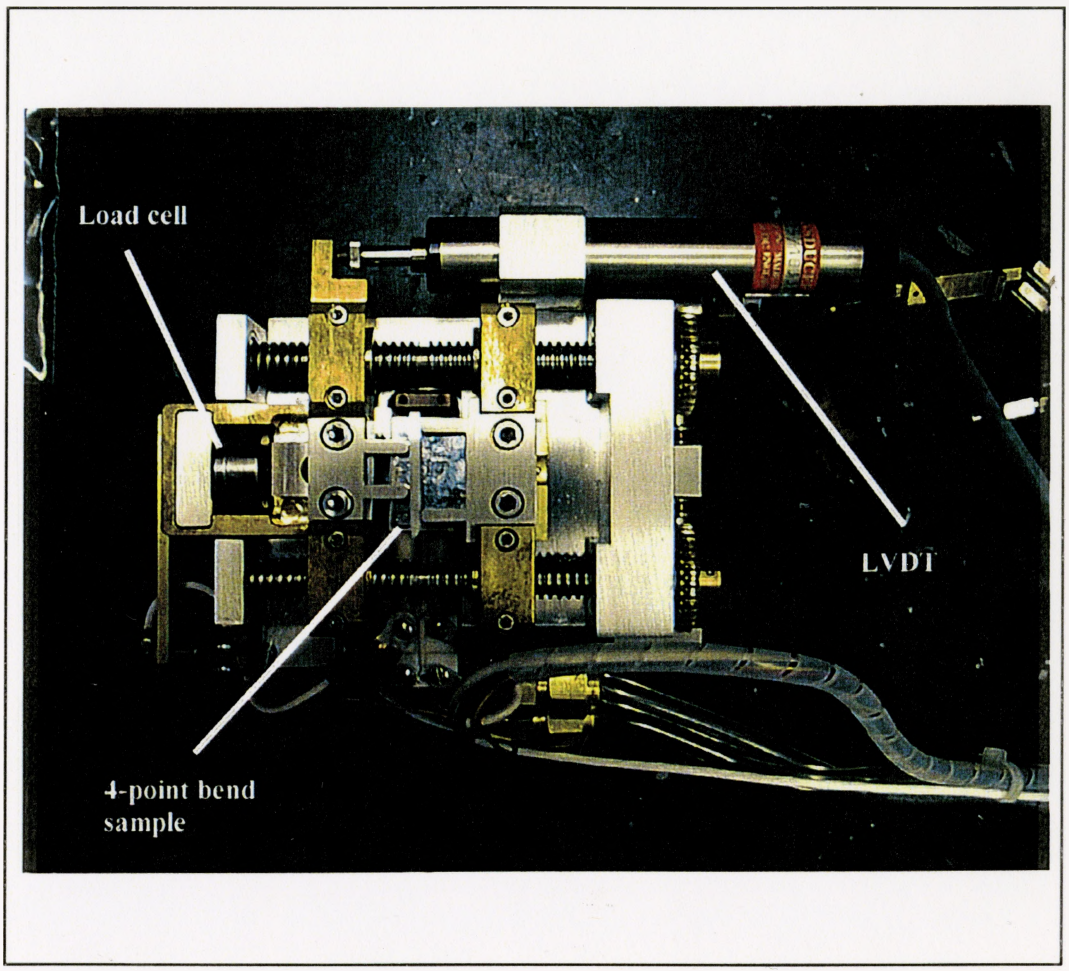

Figure 3.9 4-point bend stage for *in situ* fracture observation in the ESEM.

Chapter 4: Results and Discussion

4.1 Characterization of EPD Ceramics

4.1.1 Monolithic Al_2O_3 and TZ3Y

The procedure for electrophoretic deposition (EPD) was discussed in Section 3.1.1, and the measurement of physical properties in Section 3.1.2. The results for monolithic Al_2O_3 and TZ3Y are listed in **Table 4.1** (errors represent a 95% confidence interval).

	E (GPa)	ν	α (°C^{-1})	ρ (g/cm^3)	T_o (MPa m$^{0.5}$)
Al_2O_3	388 ± 13	0.26 ± 0.01	8.39 x 10^{-6}	3.95 ± 0.04	2.8 ± 0.5
TZ3Y	221 ± 12	0.31 ± 0.008	11.4 x 10^{-6}	6.04 ± 0.02	4.5 ± 0.2

Table 4.1

The measured results for E and ν are within the range of results reported in the literature (Oechsner *et al.*, 1996; Hillman *et al.*, 1996; Moya *et al.*, 1997; Chen and Mecholsky, 1993).

The values for α were not measured in this study and are average quantities (25-1000°C) from Hillman *et al.* (1996).

The theoretical densities of α-Al_2O_3 and t-ZrO_2 are 3.99 and 6.10 g/cm^3, respectively (Richerson, 1992). The average density in Table 4.1 indicates that the monolithic samples are ~99% dense, which agrees with previous results of EPD (Nicholson *et al.*, 1993; Whitehead, 1994; Ritcey, 1995).

The measured toughness of Al_2O_3 agrees well with values reported in the literature, ie; Whitehead (1994) reported 2.91 ± 0.49 MPa m$^{0.5}$, Ritcey (1995) reported 2.30 ± 0.06 MPa m$^{0.5}$, and Chen and Mecholsky (1993) reported 2.8 MPa m$^{0.5}$. The measured toughness for TZ3Y is slightly lower than those in the literature; ie. Hillman *et al.* measured 6.2 MPa m$^{0.5}$, Anderson *et*

al. (1990) reported 4.2 to 5.9 M Pa $m^{0.5}$ (depending on sintering conditions).

4.1.2 Multilayered Composites

Two kinds of defects appeared following densification of the Al_2O_3/TZ3Y composites; delamination and curling. Delamination through the layers is an extension of edge cracking and is related to the *geometry* of the composite (Oechsner *et al.*, 1996). Some minor curling was observed in all sintered deposits. This problem was usually associated with deposits from new suspensions and is believed to be caused by a gradient in particle size (differential densification between the two sides of a deposit causes the non-planarity) but no analysis was done to verify this explanation.

15 composites with different layering design (labeled C1-C15) were prepared for fracture testing in 4-point bend. The cross-sections of each composite are shown in **Figure 4.1(a-o)** (width of each picture ~2.8 mm). The Al_2O_3 layers (dark) were generally thinner than those of TZ3Y which also formed the outer layers. Figure 4.1 shows some asymmetry in the outer TZ3Y layers due to the slight non-planarity of the sintered deposits.

The measured Al_2O_3 volume fraction, layer thickness and calculated residual stress for composites C1-C15 (in order of increasing Al_2O_3 volume fraction) are listed in **Table 4.2** (errors represent a 95% confidence interval). The compressive stress in Al_2O_3 is very high and the tensile stress in TZ3Y is negligible for those composites with low Al_2O_3 volume fraction (Equations 2.28; p.26).

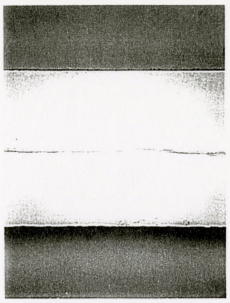

(a) Composite C1

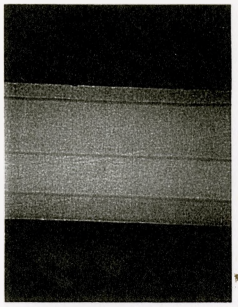

(b) Composite C2

(c) Composite C3

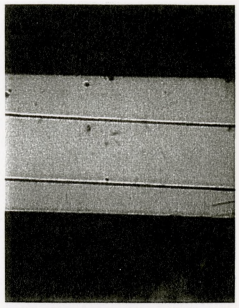

(d) Composite C4

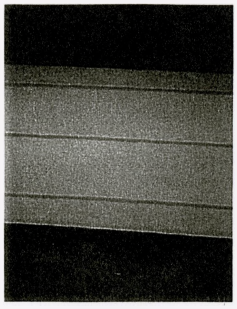

(e) Composite C5

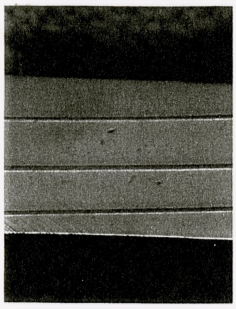

(f) Composite C6

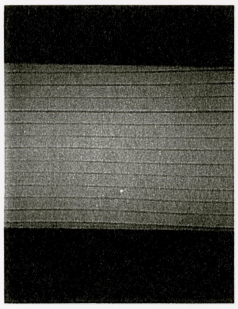

(g) Composite C7

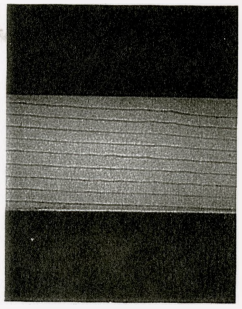

(h) Composite C8

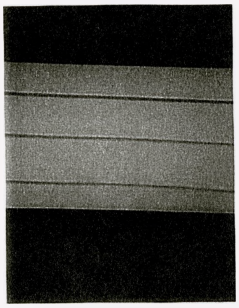

(i) Composite C9

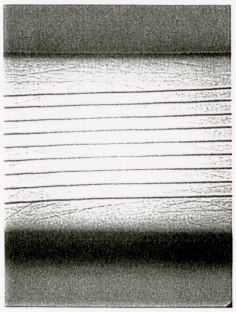

(j) Composite C10

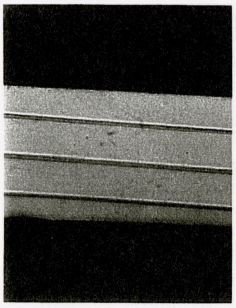

(k) Composite C11

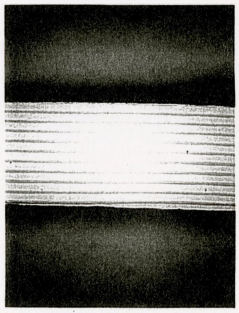

(l) Composite C12

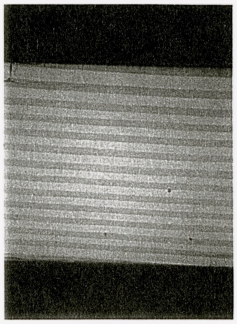

(m) Composite C13

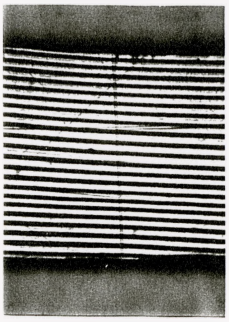

(n) Composite C14

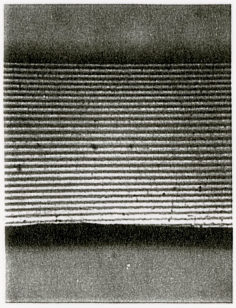

(o) Composite C15

Figure 4.1(a-o)
Optical micrographs of composite cross-sections.
(width of field 2.8 mm)

Name	Average Al_2O_3 Volume Fraction (Vol %)	error (Vol %)	Average Al_2O_3 Layer Thickness (um)	error (um)	Average stress in Al_2O_3 (compressive) (M Pa)	Average stress in TZ3Y (tensile) (M Pa)
C1	2.36	0.14	46.12	3.52	1791	33
C2	3.59	0.40	46.26	5.60	1740	50
C3	4.15	0.18	51.94	6.13	1718	58
C4	4.48	0.27	37.77	3.20	1704	62
C5	6.11	0.90	36.38	2.78	1641	84
C6	6.38	0.51	40.15	3.00	1630	88
C7	6.65	0.80	10.17	2.22	1620	92
C8	7.78	0.62	15.13	1.61	1578	107
C9	8.24	0.69	39.16	3.66	1561	113
C10	9.37	0.78	23.75	1.97	1521	129
C11	9.78	1.22	45.47	5.51	1506	134
C12	26.32	1.39	31.07	3.40	1025	349
C13	43.67	5.96	85.39	14.31	667	560
C14	46.51	1.88	53.95	2.69	618	594
C15	48.44	4.88	36.80	3.86	586	616

Table 4.2

ESEM micrographs (**Figure 4.2, a-o**) of Al_2O_3 layers in each composite show shallow edge cracks along the centre of layers in C1-C6, C9 and C11. The appearance of these cracks is similar to those observed by Ho *et al.* (1995), Oechsner *et al.* (1996) and Sánchez-Herencia (1998). The relationship of these cracks to the composite geometry is discussed in Section 4.3.

Scanning electron micrographs (ESEM) of the interface between Al_2O_3 and TZ3Y layers are shown in **Figure 4.3 (a-d)**. There is evidence of minor porosity at grain boundaries but the interfaces are dense and well-bonded. High perfection interfaces are a feature of the EPD process. The microstructures in Figure 4.3 can be compared to those in Figure 2.13; p.27 and Figure 2.29; p.44 produced by tape casting and centrifugal slip casting, respectively.

Figure 4.3 indicates the average Al_2O_3 grain size is larger than TZ3Y. The results of the grain size measurements (Section 3.2.2) for each composite are shown in **Figure 4.4** (error bars represent 95% confidence intervals). The average TZ3Y grain size varies little (average 0.67μm ±

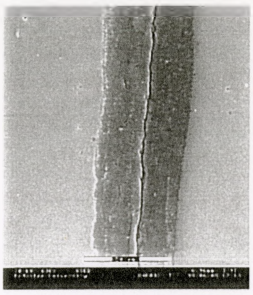

(a) Composite C1

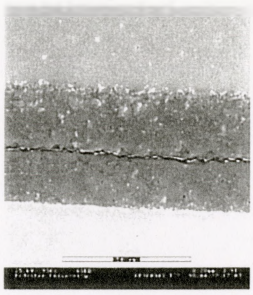

(b) Composite C2

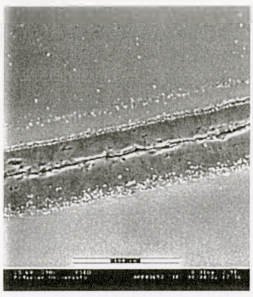

(c) Composite C3

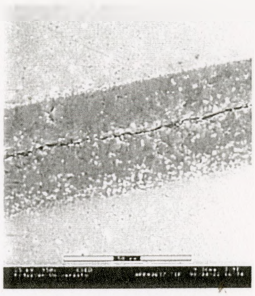

(d) Composite C4

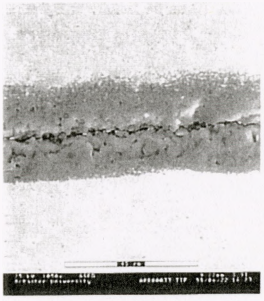

(e) Composite C5

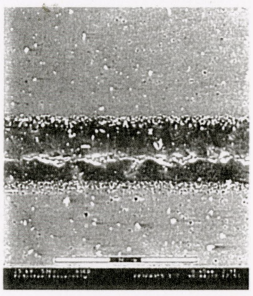

(f) Composite C6

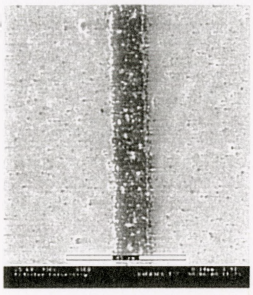

(g) Composite C7

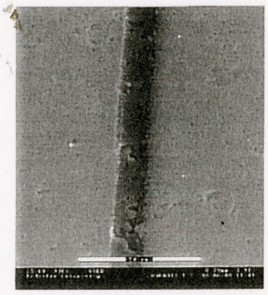

(h) Composite C8

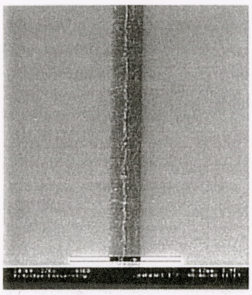

(i) Composite C9

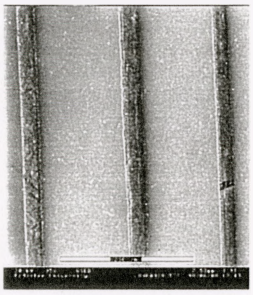

(j) Composite C10

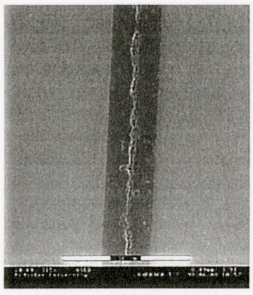

(k) Composite C11

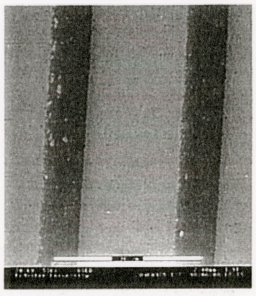

(l) Composite C12

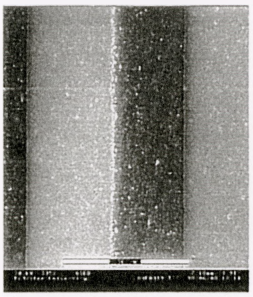

(m) Composite C13

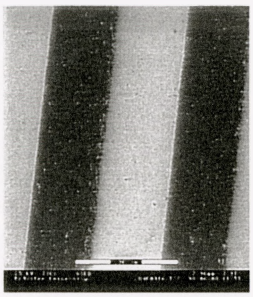

(n) Composite C14

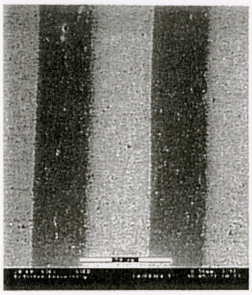

(o) Composite C15

Figure 4.2(a-o)
ESEM micrographs of Al_2O_3 layers in composites C1-C15.

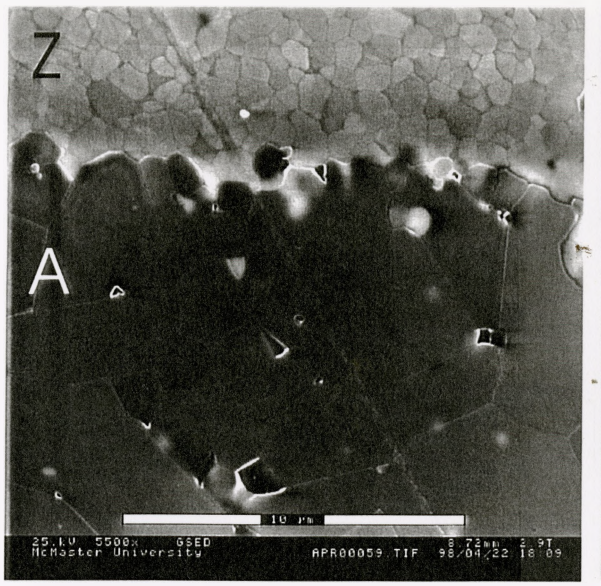

(a) Composite C11 (5500 X)

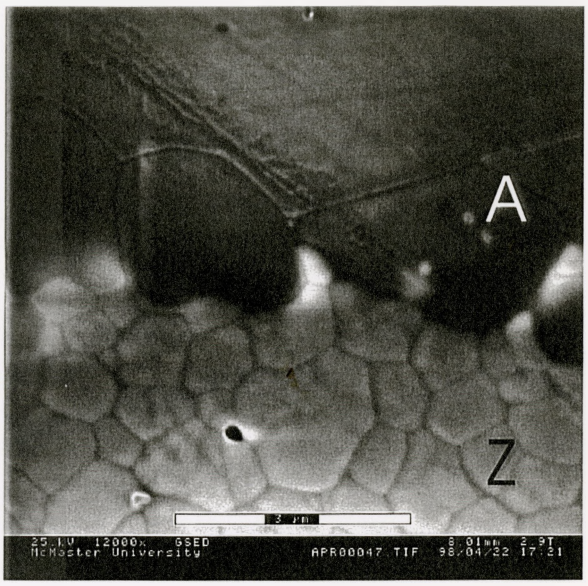

(b) Composite C6 (12000 X)

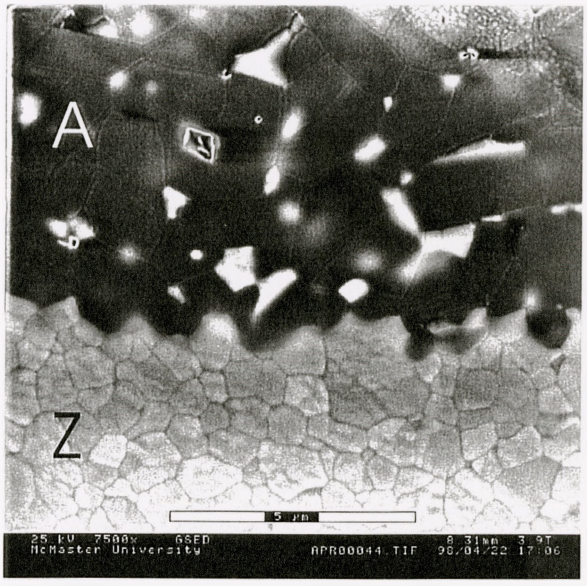

(c) Composite C2 (7500 X)

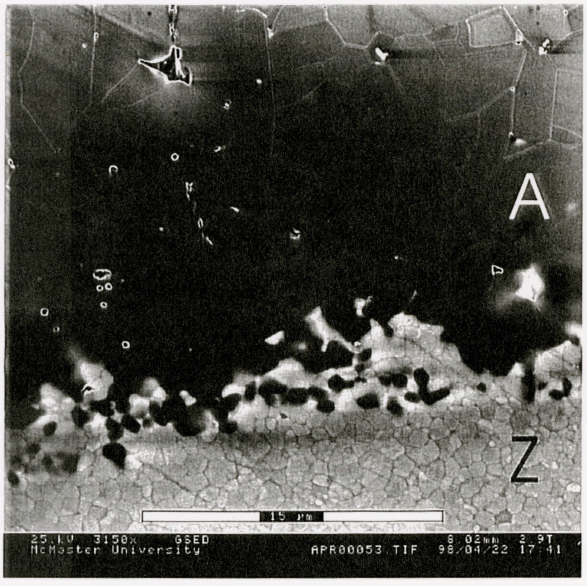

(d) Composite C3 (3150 X)

Figure 4.3 (a-d) ESEM micrographs of the Al_2O_3/TZ3Y interfaces.

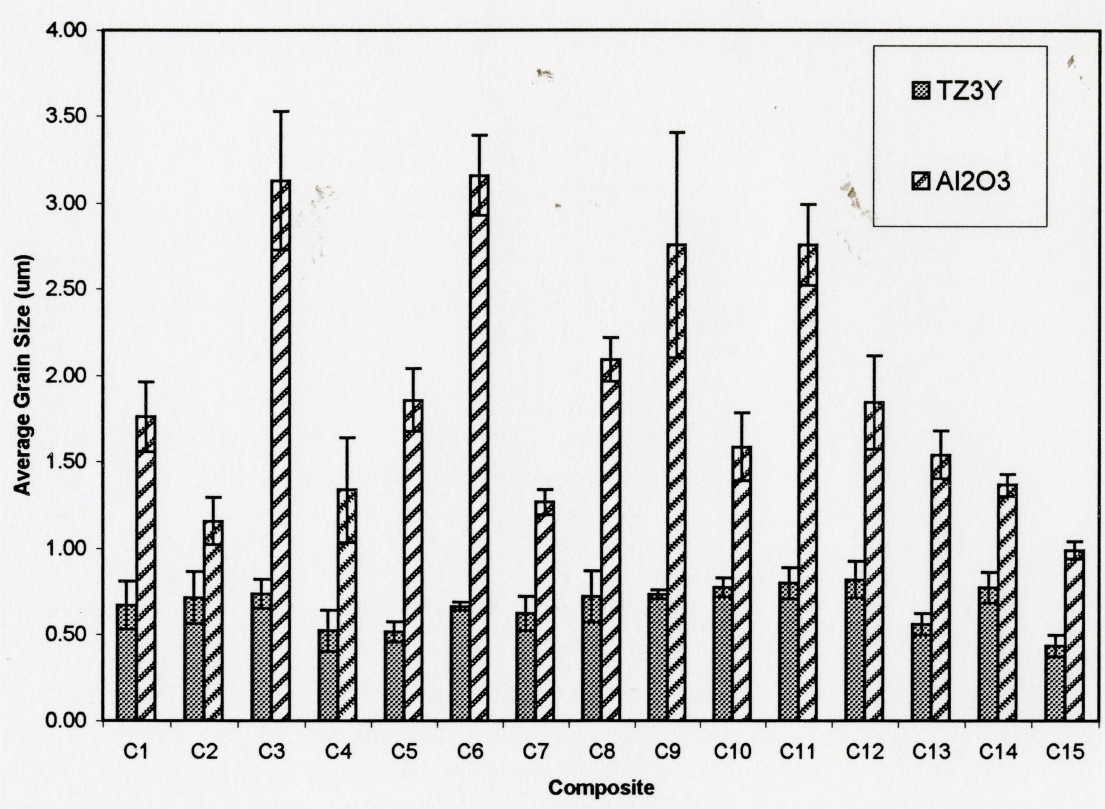

Figure 4.4 Grain size measurements for Al_2O_3 and TZ3Y layers in composites C1-C15.

0.07) but the average Al_2O_3 grain size varies from 0.99 to 3.2 μm. Sintering at 1550°C for 6 hours results in grain growth of the dense layers of 100% Al_2O_3 (Figure 4.3a,b,d). Figure 4.2 suggests there has been minor mixing of TZ3Y grains into the Al_2O_3 layer (and vice versa) for composites C2, C4, C7, and C13-C15. Small additions of TZ3Y grains will prevent grain growth in the Al_2O_3, as observed by Jiménez-Melendo *et al.*, 1997. Minor mixing between the two colloidal suspensions can occur during sequential deposition especially after a number of layers have been built from the same suspension. The homogeneity of very thin Al_2O_3 layers (ie; ≈10μm in C7) is more sensitive to interfacial mixing than thick layers.

4.2 Residual Stress Measurements

The piezospectroscopic fluorescence technique for measuring stress in Al_2O_3 (with Cr^{3+} impurity) was discussed in Section 2.3.2 (theory) and Section 3.2.3 (procedure). Measurements of the shift ($\Delta\nu$) in fluorescence spectra were made for Al_2O_3 layers in composites C1-C15 and monolithic Al_2O_3 samples A-D. The spectra for certain composite and monolithic samples in terms of the absolute wavenumber (cm^{-1}) are shown in **Figure 4.5** (normalized to the same intensity). The spectra for monolithic Al_2O_3 (assumed to be free of macrostress) appear on the right. The spectra corresponding to the composite samples are shifted to the left in proportion to residual stress in the Al_2O_3 layers. The average hydrostatic stresses (σ_{Hyd}) in the samples were determined from $\Delta\nu$ (averaged for R1 and R2) and using Equations 2.32;p.33 and 2.33;p.33.

Calculation of σ_{Hyd} (to compare with the measured quantities) is complicated by the fact that fluorescence spectroscopy is limited to the surface of polycrystalline ceramics. The probe sensitivity function (Lipkin and Clarke, 1996) must be determined to identify the actual depth of measurement but this calibration was beyond the scope of the present study.

The biaxial residual stress ($\sigma_{xx} = \sigma_{zz} = \sigma_r$) acting within the layers (away from the free surface) was calculated using Equations 2.28;p.26. In Figure 2.12;p.25, $\sigma_{xx} = 0$ at the free surface ($x = 0$), and increases to $\sigma_{xx} = \sigma_r$ with x. A tensile stress at the surface, σ_{yy}, acts normal to the layer plane (Figure 2.15;p.29, Ho *et al.*, 1995). At the surface (x=0), $\sigma_{yy} = -\sigma_r$ and becomes negligible at $x/t \approx 1$ (Figure 2.17; p.30). Thus, calculation of σ_{Hyd} is complicated by **three** factors; the effective depth of the spectroscopic measurement, the decrease of $\sigma_{yy}(x)$, and the increase of $\sigma_{xx}(x)$, from the surface. All three factors act over a scale of the same order of magnitude.

It is impossible to accurately calculate σ_{Hyd} without a numerical or analytical solution for the stress and knowledge of the probe sensitivity (ie; Sergo *et al.*, 1997). However, there are **two** practical limits to the calculation of σ_{Hyd} (hereafter referred to as σ_{max} and σ_{min}) which depend on

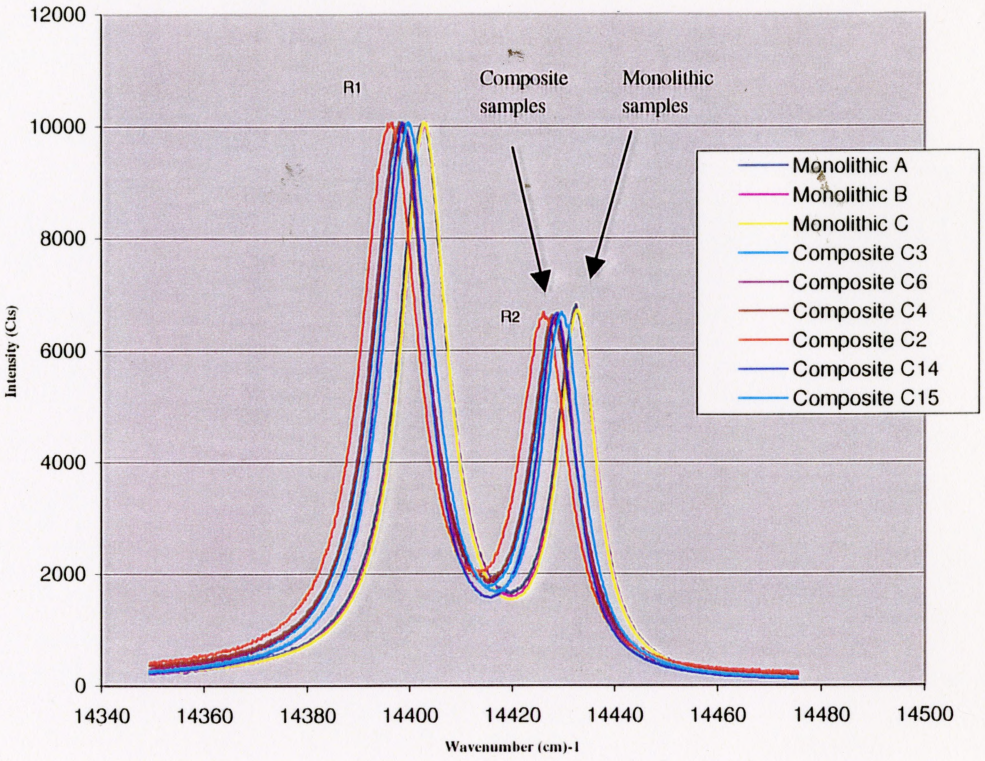

Figure 4.5 Fluorescence spectra measured for certain composite and monolithic Al_2O_3 samples (each spectrum normalized to the same intensity).

the choice of boundary conditions. A *maximum* condition can be defined, ie;

$\sigma_{yy} \approx 0$

$\sigma_{xx} \approx \sigma_{zz} = \sigma_r$

$\therefore \sigma_{max} = 2/3(\sigma_r)$

A *minimum* condition can also be defined,

$\sigma_{yy} \approx -\sigma_r$

$\sigma_{xx} \approx \sigma_{zz} = \sigma_r$ (or, equivalently, $\sigma_{yy} \approx 0$, $\sigma_{xx} \approx 0$, and $\sigma_{zz} = \sigma_r$)

$\therefore \sigma_{min} = 1/3(\sigma_r)$.

A third condition also exists for $\sigma_{yy} \approx -\sigma_r$, $\sigma_{xx} = 0$ and $\sigma_{zz} = \sigma_r$ (so that $\sigma_{Hyd} = 0$), but this case can be ignored since Figure 4.5 clearly indicates $\Delta\nu \neq 0$.

The calculated results for σ_{max} and σ_{min} and the measured results for $\Delta\nu$ and σ_{Hyd}, are listed in **Table 4.3** (the measurement errors arise from curve fitting). The results for σ_{max}, σ_{min} and σ_{Hyd} are plotted in terms of Al_2O_3 volume fraction in **Figure 4.6** (monolithic samples = 100 vol% Al_2O_3).

In general the measurements of σ_{Hyd} lie within the limits of σ_{max} and σ_{min}. There is significant scatter within the data but σ_{Hyd} appears more closely represented by σ_{min} than σ_{max}. These results indicate that the probe volume is *not* significantly larger than the scale of $\sigma_{xx}(x)$ or $\sigma_{yy}(x)$, and free surface effects cannot be ignored.

Variation in the data is a combination of error in measurement and differences between samples. There is a measurement error associated with the position of the laser spot which is difficult to position precisely on the layer midpoint. Figure 2.17;p.30 indicates that σ_{yy} varies across the layer thickness (Ho *et al.*, 1995). This measurement error is more pronounced for thinner layers (<40μm), since the laser spot size is ~30μm.

Measured stresses in the monolithic samples show an inherent variation (± 75 M Pa). Monolithic Al_2O_3 is assumed to contain no macrostress, but thermal residual stresses also develop

Table 4.3

Name	Al_2O_3 Vol.% (%)	error (%)	Calculated σ_r (M Pa)	Calculated σ_{min} (M Pa)	Calculated σ_{max} (M Pa)	Measured Average Δv (cm-1)	Measured error (cm-1)	Measured σ_{Hyd} (M Pa)	Measured error (M Pa)
A	100	0	0	0	0	-0.11	0.25	14.6	32.8
A	100	0	0	0	0	0.43	0.25	-56.0	32.8
B	100	0	0	0	0	-0.37	0.25	49.2	32.8
B	100	0	0	0	0	0.00	0.25	-0.1	32.8
C	100	0	0	0	0	0.02	0.25	-2.7	32.8
D	100	0	0	0	0	-0.13	0.25	17.4	32.8
D	100	0	0	0	0	0.16	0.25	-21.1	32.8
C1	2.36	0.14	1816.8	605.6	1211.2	-4.11	0.25	541.4	32.9
C2	3.59	0.40	1777.6	592.5	1185.1	-5.28	0.25	695.2	32.8
C2	3.59	0.40	1777.6	592.5	1185.1	-4.63	0.25	609.2	32.8
C3	4.15	0.18	1760.1	586.7	1173.4	-4.59	0.25	604.2	32.8
C3	4.15	0.18	1760.1	586.7	1173.4	-3.84	0.25	505.9	32.8
C3	4.15	0.18	1760.1	586.7	1173.4	-3.44	0.25	453.2	32.8
C4	4.48	0.27	1749.8	583.3	1166.5	-4.78	0.25	629.4	32.8
C4	4.48	0.27	1749.8	583.3	1166.5	-3.73	0.25	490.7	32.9
C5	6.11	0.90	1699.7	566.6	1133.1	-4.61	0.25	606.5	32.8
C6	6.38	0.51	1691.5	563.8	1127.7	-4.92	0.25	647.3	32.8
C6	6.38	0.51	1691.5	563.8	1127.7	-5.15	0.25	678.2	32.8
C6	6.38	0.51	1691.5	563.8	1127.7	-4.60	0.25	605.9	32.8
C7	6.65	0.80	1683.3	561.1	1122.2	-5.93	0.25	780.9	32.9
C8	7.78	0.62	1649.5	549.8	1099.7	-5.22	0.25	687.5	32.8
C9	8.24	0.69	1635.9	545.3	1090.6	-4.41	0.25	580.9	32.8
C10	9.37	0.78	1602.9	534.3	1068.6	-5.29	0.25	696.7	32.8
C11	9.78	1.22	1591.1	530.4	1060.7	-4.52	0.25	594.7	32.8
C12	26.32	1.39	1163.9	388.0	775.9	-3.76	0.25	495.3	32.8
C13	43.67	5.96	802.1	267.4	534.7	-2.62	0.25	344.7	32.8
C14	46.51	1.88	749.6	249.9	499.7	-2.09	0.25	275.7	32.8
C14	46.51	1.88	749.6	249.9	499.7	-2.73	0.25	359.1	32.8
C14	46.51	1.88	749.6	249.9	499.7	-2.52	0.25	331.5	32.8
C15	48.44	4.88	714.8	238.3	476.5	-3.08	0.25	404.9	32.8
C15	48.44	4.88	714.8	238.3	476.5	-2.69	0.25	353.9	32.8

Table 4.3 Results of stress measurements for Al_2O_3 layers and monoliths and calculated values of σ_{max} and σ_{min}.

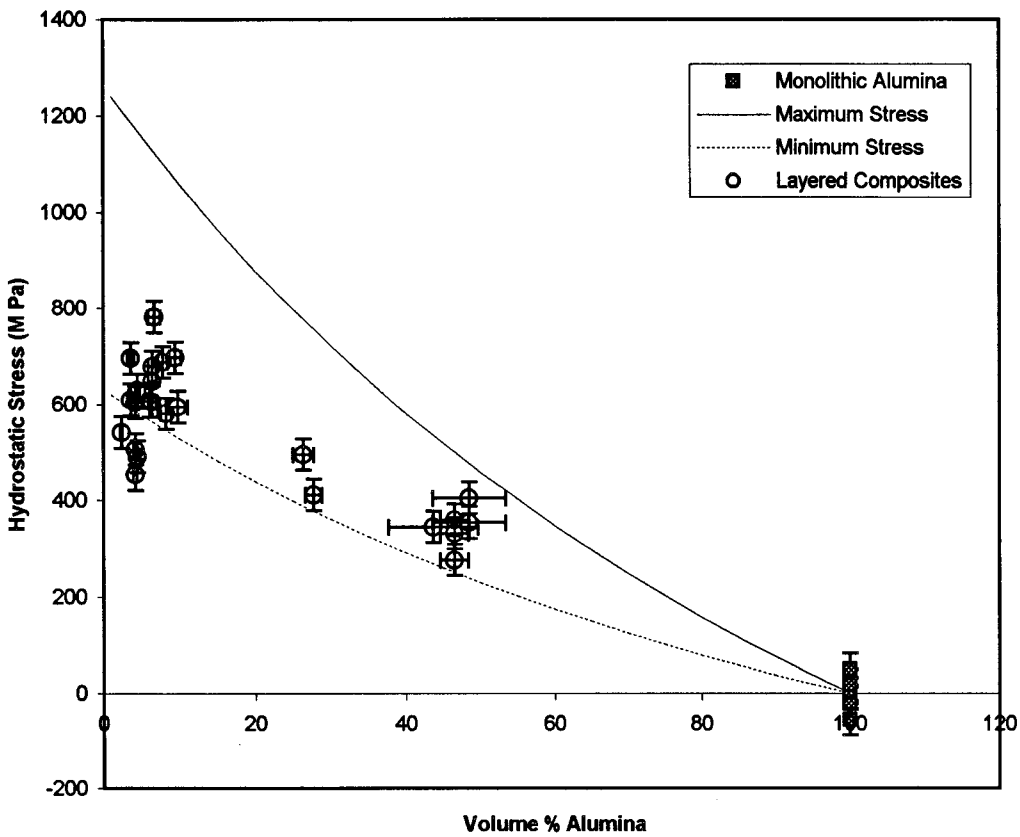

Figure 4.6 Compressive hydrostatic stress measured for composites C1-C15 as a function of the Al_2O_3 volume fraction.. The calculated limits for σ_{max} and σ_{min} are also shown.

in Al_2O_3 as a result of anisotropy in the crystal structure.

There is large variation in the data for composites < 20 vol% Al_2O_3. To determine whether this variation is correlated to other variables, σ_{Hyd} is plotted relative to the average Al_2O_3 layer thickness and grain size in **Figures 4.7(a)** and **4.7(b)**, respectively (error bars omitted for clarity). Linear regression analysis of the data was used to plot curves of best fit. The results indicate that the slope in 4.7(a) is significantly different from zero (95% confidence), but the slope in 4.7(b) is not. There appears to be no measurable influence of Al_2O_3 grain size on the measured stress. A higher hydrostatic stress in thinner layers may be related to the relative size of the probe volume and the layer thickness. For a given probe depth (50-100μm) the influence of the surface tensile stress σ_{yy} is smaller for thin layers than for thick layers. Therefore for thin layers the conditions are closer to the assumptions for σ_{max} than for σ_{min}, even though the calculated values are similar.

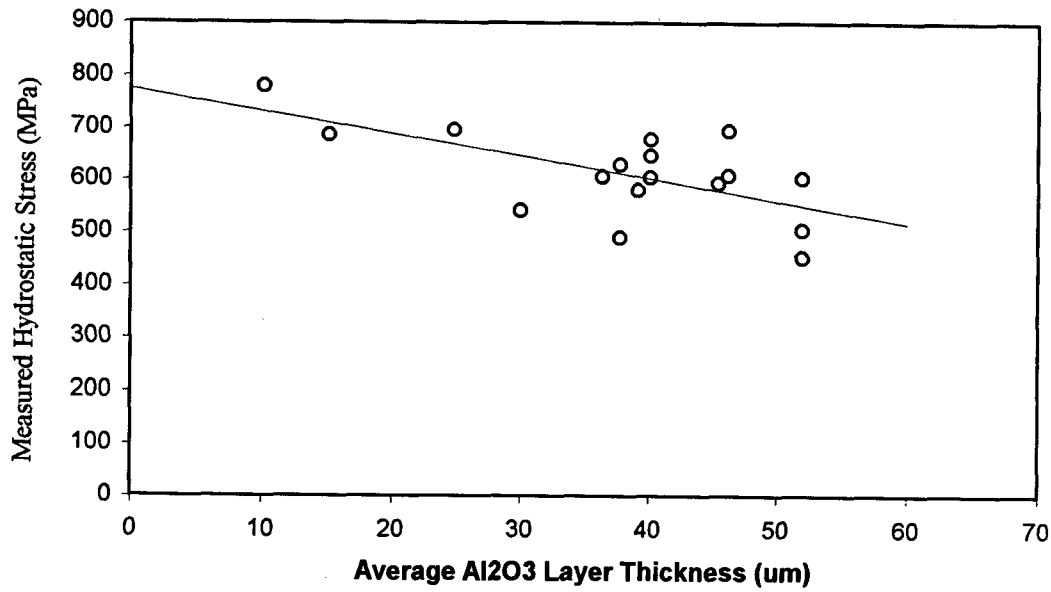

Figure 4.7(a) Compressive hydrostatic stress for composites < 10 Al_2O_3 Vol% as a function of the average Al_2O_3 layer thickness.

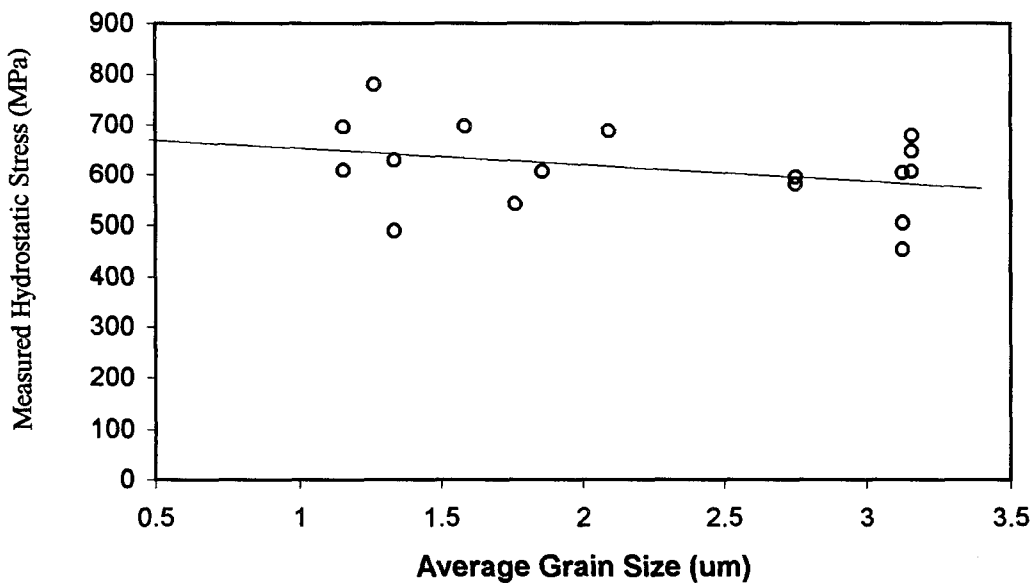

Figure 4.7(b) Compressive hydrostatic stress for composites < 10 Al_2O_3 Vol% as a function of the average Al_2O_3 grain size.

4.3 The Influence of Laminate Design on Flaw Tolerance

The relationship between layer thickness and crack bifurcation was demonstrated by Oechsner *et al.*, (1996) for a multi-layered Al_2O_3/Ce-ZrO_2 composite and by Sánchez-Herencia *et al.* (1998) for a series of three-layered m-ZrO_2/t-ZrO_2 composites. This section examines the influence of layer design on the fracture behaviour and flaw tolerance of Al_2O_3/TZ3Y composites C1-C15 (Table 4.2). The ISB technique (Section 3.3.1) was used to compare the strength of the composites with monolithic TZ3Y. A 10 kg indentation was used to introduce surface cracks into all samples, (except for composite C15 which was notched by laser machining (Section 3.1.2)).

4.3.1 Differences in Fracture Behaviour

The 4-point bend, stress-deflection curves for composites C1-C15 and monolithic TZ3Y are shown in **Figure 4.8 (a-p)** and cross-sections of the fractured samples are shown in **Figure 4.9 (a-p)** (the arrows indicate the indentation site).

Distinction can be made in Figure 4.8 between multi-stage fracture (consisting of at least one *partial* load drop) and catastrophic failure (one *complete* drop). Multi-stage fracture was associated with crack arrest at, and deflection along, the (first) Al_2O_3 layer. **Figures 4.10(a, b)** were taken *in situ* during 4-point loading and show the partial fracture along an Al_2O_3 layer. Figure 4.10b shows a sample in a third stage of fracture. In Figure 4.9 a-f, i and k, the 'parent' crack initiates from the indentation site, intercepts an Al_2O_3 layer and bifurcates along the layer. The bifurcation into two 'branch' cracks was also observed by Oechsner *et al.* (1996). The two branch cracks propagate through the Al_2O_3 layer a significant distance before fracture reinitiates in the next TZ3Y layer (unlike Oechsner *et al.* in Figure 2.36; p.53) . The position of fracture reinitiation did not depend on the initial indentation site. A series of ESEM micrographs of the Al_2O_3 layer in a partially fractured sample (C1) **(Figure 4.11)** indicate that the branch cracks propagate through

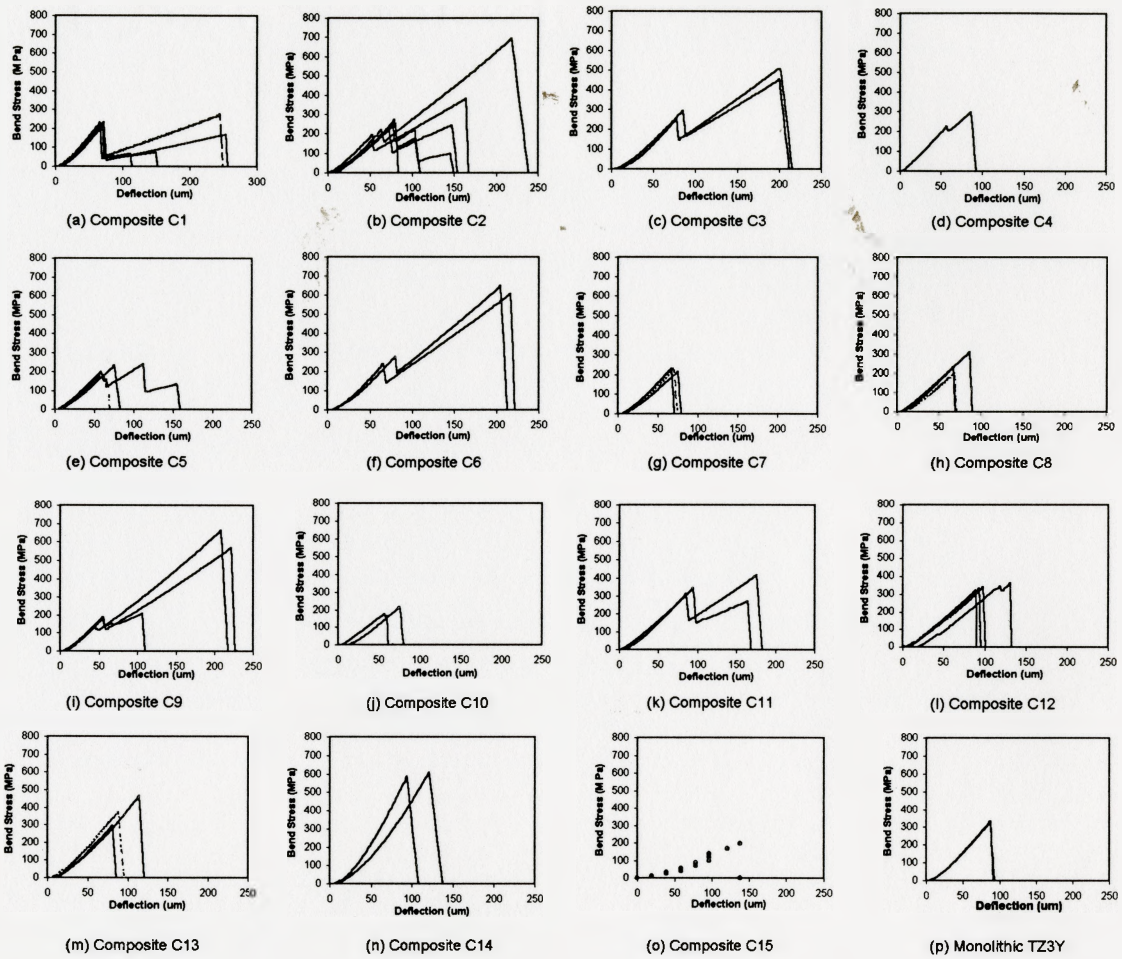

Figure 4.8 (a-p) Stress-deflection curves for Al_2O_3/TZ3Y composites C1-C15 and monolithic TZ3Y.

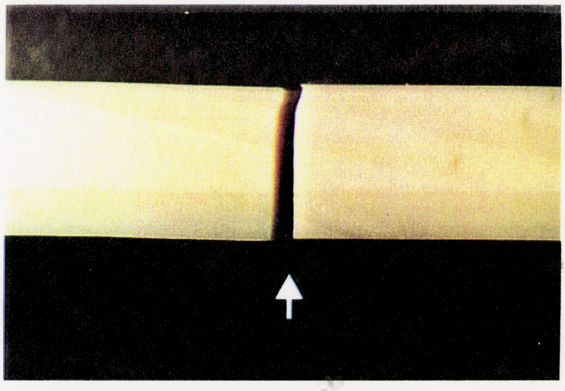

Figure 4.9(a) Monolithic TZ3Y (8x)

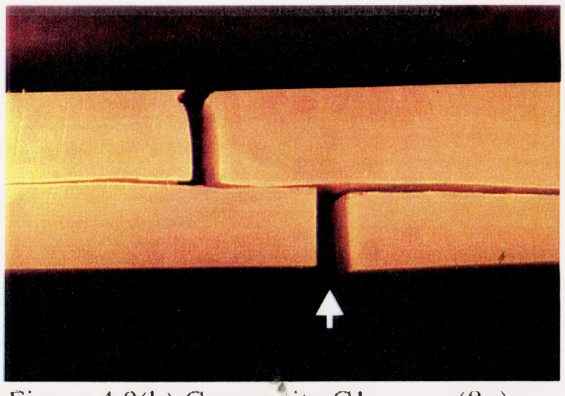

Figure 4.9(b) Composite C1 (8x)

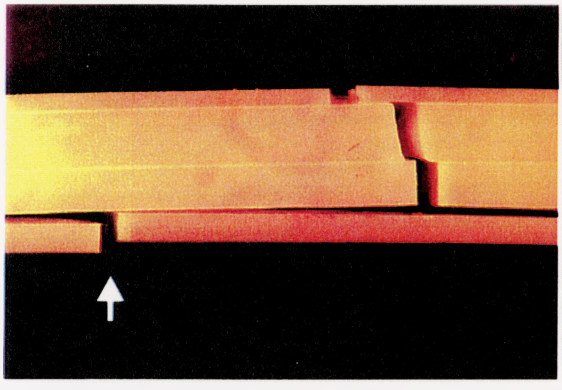

Figure 4.9(c) Composite C2 (8x)

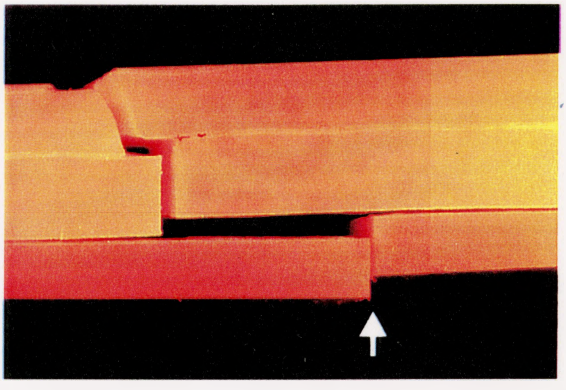

Figure 4.9(d) Composite C3 (8x)

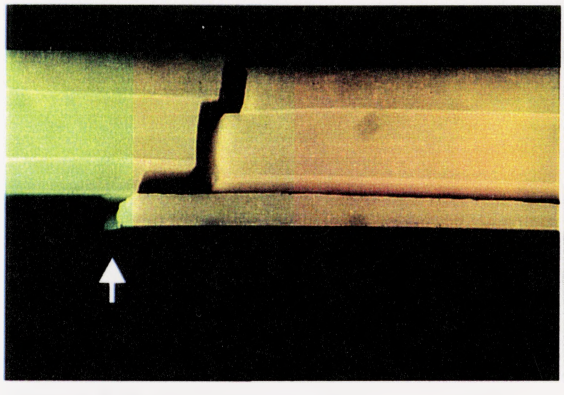

Figure 4.9(e) Composite C4 (8x)

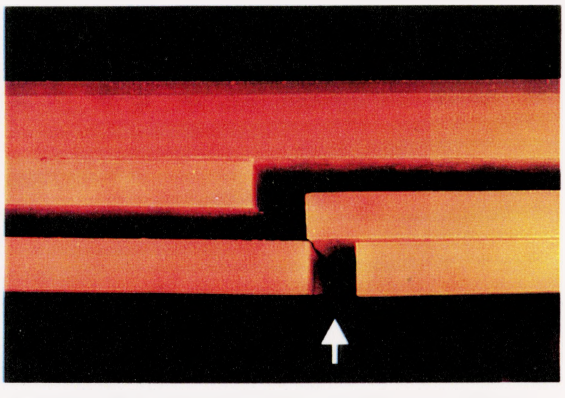

Figure 4.9(f) Composite C5 (8x)

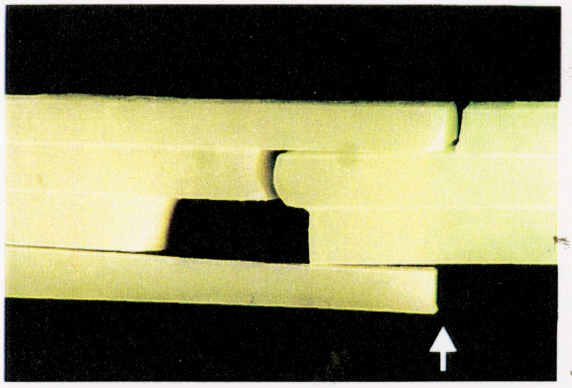

Figure 4.9(g) Composite C6 (8x)

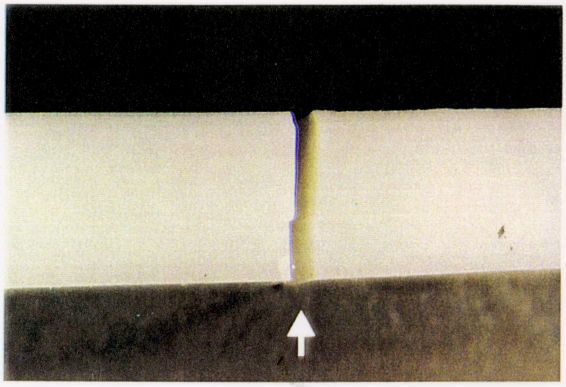

Figure 4.9(h) Composite C7 (8x)

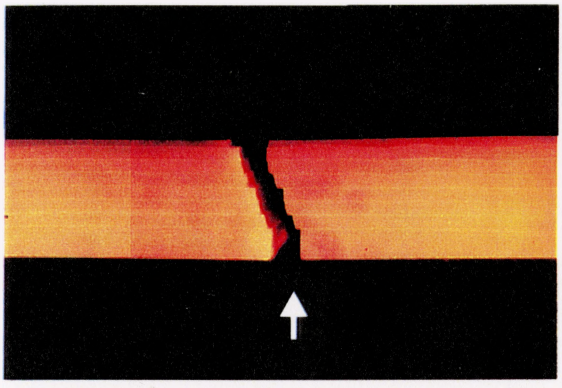

Figure 4.9 (i) Compsite C8

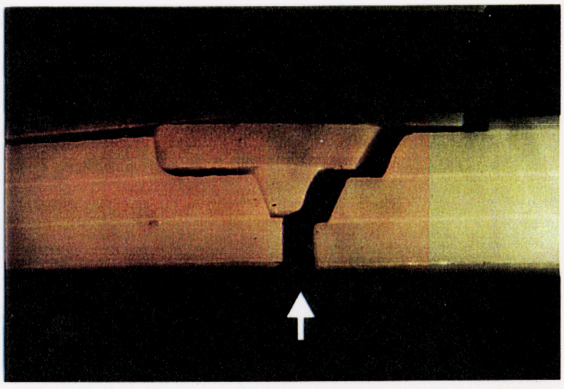

Figure 4.9 (j) Compsite C9

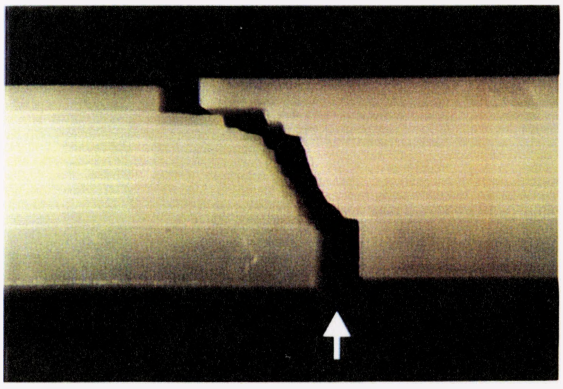

Figure 4.9 (k) Compsite C10

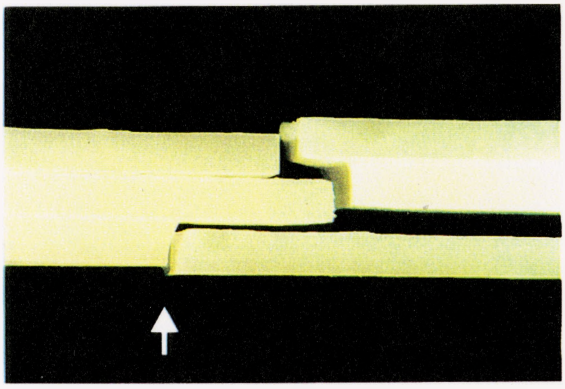

Figure 4.9 (l) Compsite C11

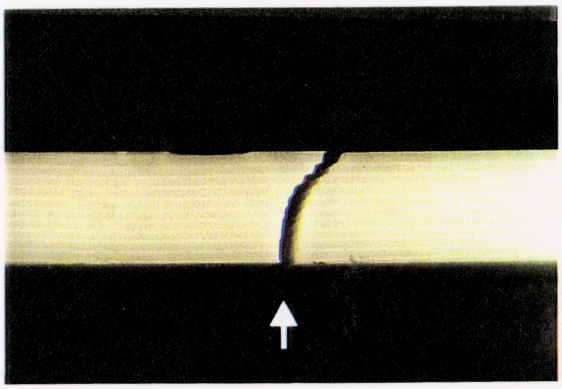

Figure 4.9 (m) Compsite C12

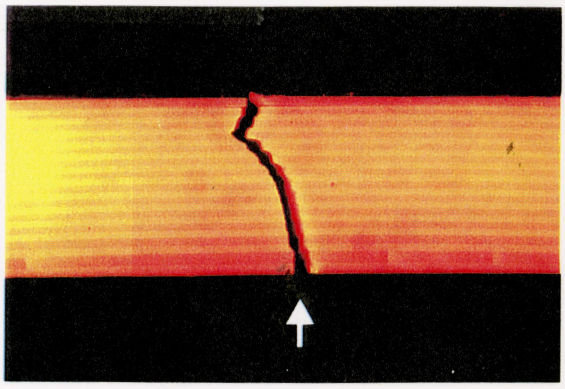

Figure 4.9 (n) Compsite C13

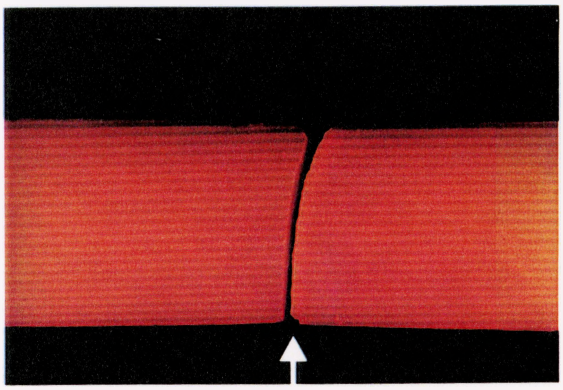

Figure 4.9 (n) Compsite C14

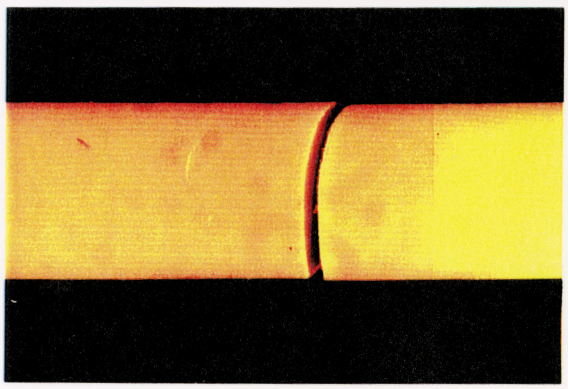

Figure 4.9 (o) Compsite C15

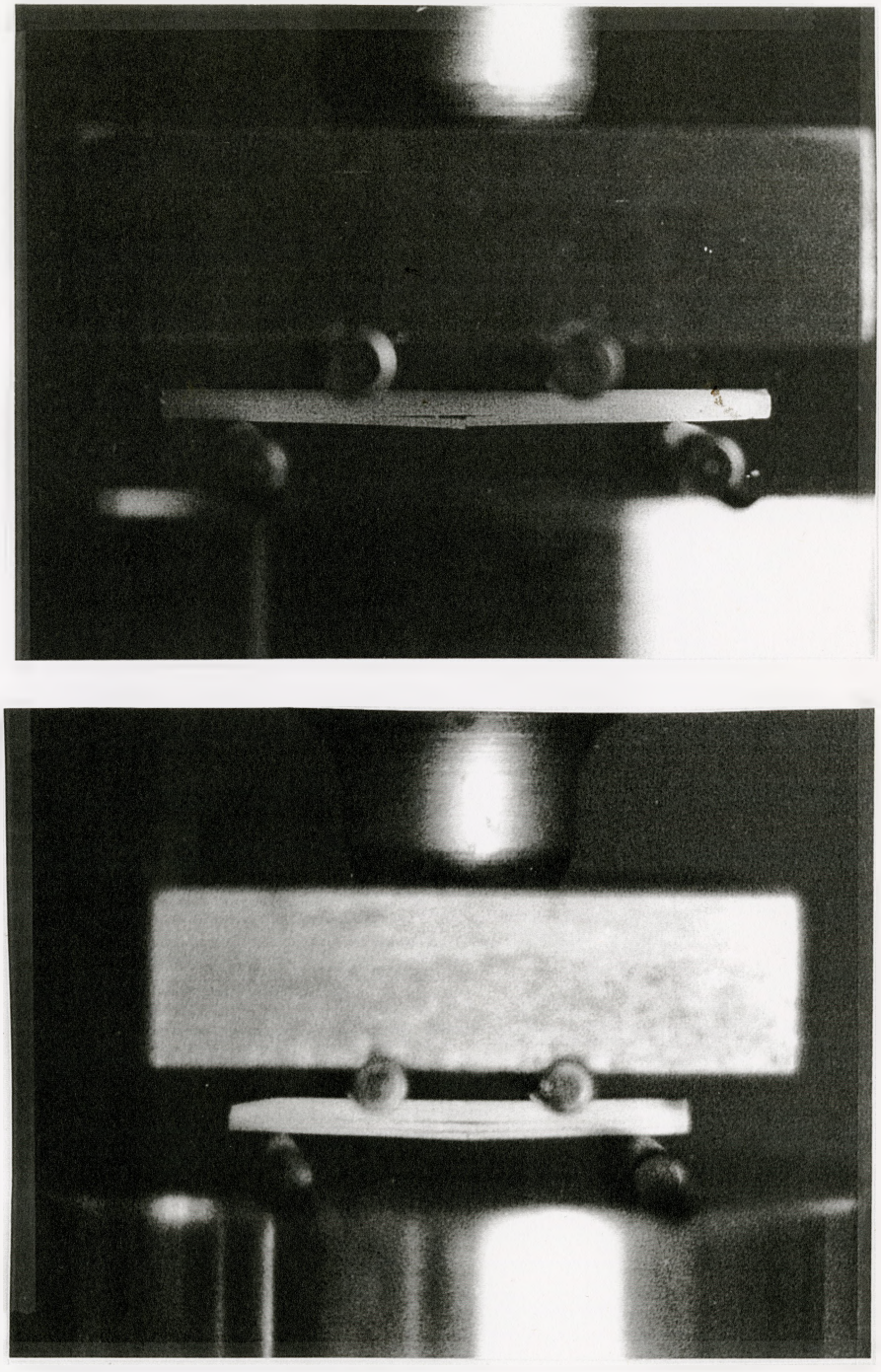

Figure 4.10 (a,b) Optical photographs taken *in situ* during the multi-stage fracture of composite samples tested in 4-point bend.

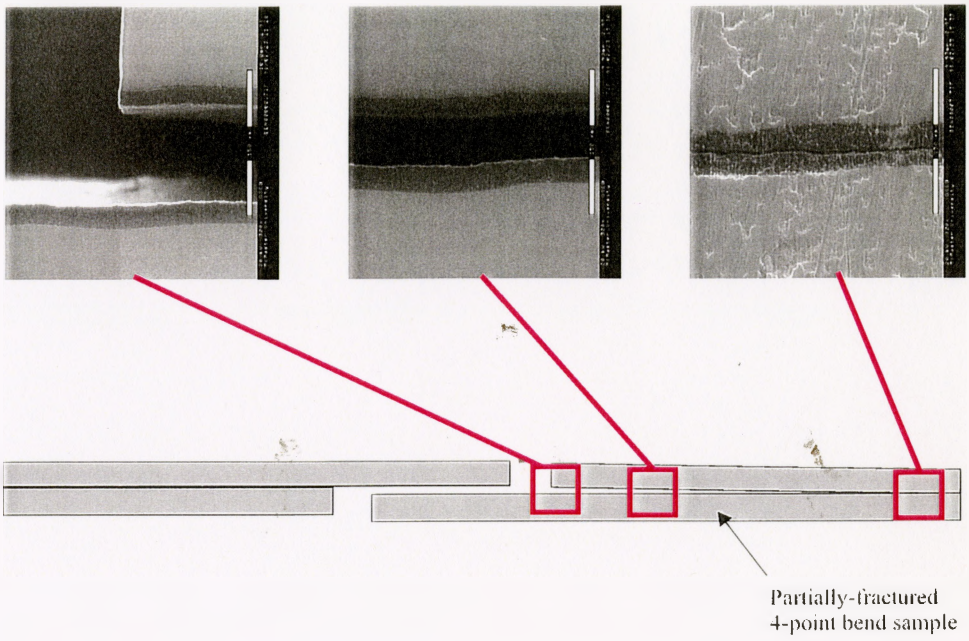

Figure 4.11 ESEM micrographs of bifurcation branch crack through Al_2O_3 layer.

the *centre* of the Al_2O_3 layer.

The partial load drops in multi-stage fracture occur because of the release of strain energy in the sample by cracks branching through the Al_2O_3 layers. The high stiffness of the test machine means that minimum energy is stored in the 4-point bend rig (ie; controlled deflection loading). Fracture of the outer TZ3Y layer, followed by bifurcation and partial delamination, increases the compliance of the composite sample, ie; the internal strain energy is reduced with crack extension and, under conditions of decreasing G(c), crack arrest can occur (Figure 2.4).

4.3.2 The Influence of Layer Design on Fracture Behaviour

Layer design is determined by two parameters; Al_2O_3 volume fraction and layer thickness. **Figure 4.12** is a 'fracture map' showing the differences of fracture behaviour in terms of these two design parameters (compare to Sánchez-Herencia *et al.*, Figure 2.40; p.57). Multi-stage fracture is represented by the blue circles and catastrophic failure by the open circles[2]. A third class of behaviour was added for those composites which delaminated during processing (during sintering (red squares) or during grinding (red circles)).

The compressive residual stress within the Al_2O_3 layers increases with decreasing Al_2O_3 volume fraction (Equation 2.25). Looking *horizontally* across Figure 4.12 at $40 < t < 50$ μm (where t is the Al_2O_3 layer thickness), there is a transition from multi-stage to catastrophic fracture between 10-25 vol% Al_2O_3. At some point there is insufficient residual stress to cause crack arrest, and Figure 4.9 indicates that there is no visible crack deflection in composites C13-C15. Looking *vertically* at 3-10 vol%, multi-stage fracture is only observed in composites with $40 < t < 50$ μm. This observation suggests an influence of scale since these composites have approximately the

---

2

Composites C2, C5 and C12 showed evidence of both multi-stage and catastrophic fracture in different samples. The sample majority was taken to catagorize the overall behaviour.

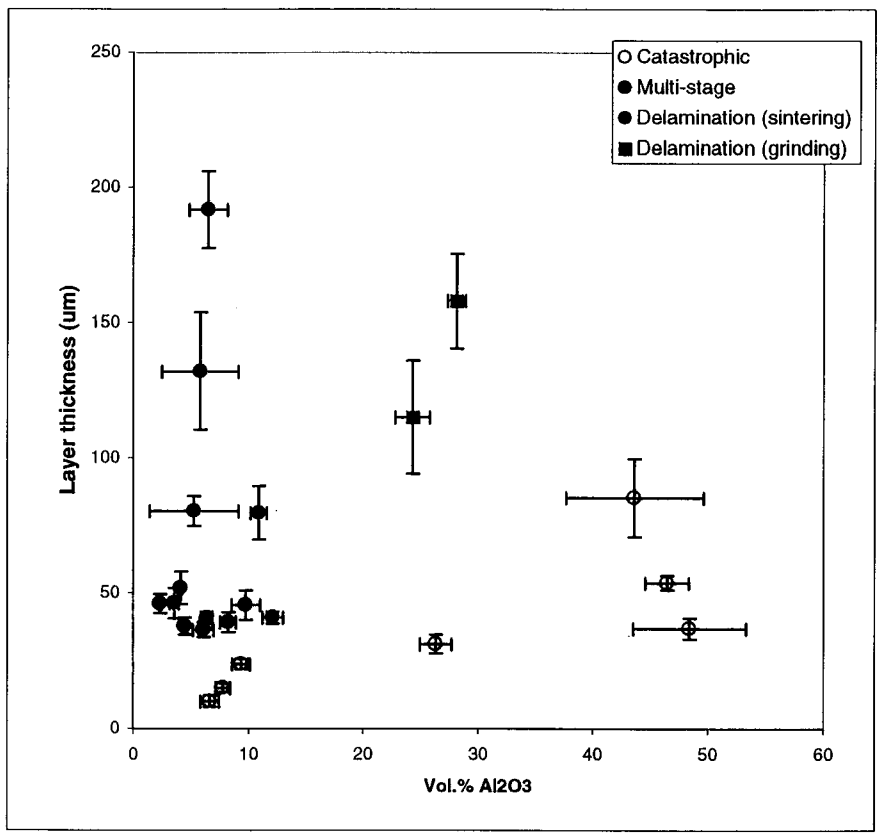

Figure 4.12 Map of the fracture behaviour of all Al_2O_3/TZ3Y composites in terms of Al_2O_3 layer thickness and volume fraction.

same value of σ_r. Spontaneous delamination during sintering occurs for $t > 50$ μm and fracture is catastrophic for those composites with $t < 40$ μm (only small fracture steps are visible).

Figure 4.12 also suggests the composites which delaminated spontaneously during sintering were more unstable than those which survived until grinding. There is a transition from failure in sintering to failure in grinding along the top of the figure as the volume fraction of Al_2O_3 increases (and σ_r decreases).

Oechsner *et al.* (1996) showed that the minimum layer thickness for crack bifurcation is given by Equation 2.38;p.45 because of the similarity to the mechanism of edge cracking. The strain energy release rate for cracks in localized stress fields (ie; edge cracks) is proportional to $\sigma_r^2 t$ (Equation 2.37; p.43). **Table 4.4** lists the layering design and fracture behaviour for each composite. Column A gives the calculated values of $\sigma_r^2 t$ (and the associated error), column B the observed fracture behaviour (ie; multi-stage, catastrophic or delamination) and column C indicates the presence of edge cracks (from Figure 4.2).

The results show that edge cracks were observed *only* in those composites with multi-stage fracture. These results agree with the observations of Sánchez-Herencia *et al.* (1998) Oechsner *et al.* (1996) observed edge cracks in Al_2O_3 layers for composites showing no bifurcation (Figure 2.38;p.54). Spontaneous delamination during processing occurs when edge cracks form at the surface and channel completely through an Al_2O_3 layer.

Figure 4.13 is a graph of $\sigma_r^2 t$ for each composite arranged according to fracture behaviour. There is a distinct transition from catastrophic failure to multi-stage fracture between $55 < \sigma_r^2 t < 98$ ($x10^6$ Pa^2m)[3]. The transition from multi-stage fracture to complete delamination is not as well defined ($\sigma_r^2 t \approx 130$), which indicates a fine balance between the two states. There is

---

[3] Unless otherwise stated, all values of $\sigma_r^2 t$ are assumed to have the units $x10^6$ Pa^2m.

Table 4.4								A		B	C
Name	Samples Tested (#)	Al2O3 Volume Fraction (Vol %)	error (Vol %)	Al2O3 Layer Thickness (um)	error (um)	Compressive Stress (M Pa)	error (M Pa)	$\sigma^2 t$	error	Fracture Behaviour	Edge Cracks? (Y/N)
TZ3Y	3	0		0		0	0	0.0	0.0	catastrophic	
C1	4	2.36	0.14	46.1	3.5	1791	20	147.9	7.3	multi-stage	Y
C2	6	3.59	0.40	46.3	5.6	1740	20	140.1	9.2	multi-stage (5/6)	Y
C3	2	4.15	0.18	51.9	6.1	1718	20	153.2	9.7	multi-stage	Y
C4	1	4.48	0.27	37.8	3.2	1704	20	109.7	7.1	multi-stage	Y
C5	3	6.11	0.90	36.4	2.8	1641	21	97.9	7.0	multi-stage (2/3)	Y
C6	2	6.38	0.51	40.2	3.0	1630	20	106.7	7.0	multi-stage	Y
C7	4	6.65	0.80	10.2	2.2	1620	21	26.7	6.6	catastrophic	N
C8	3	7.78	0.62	15.1	1.6	1578	20	37.7	6.2	catastrophic	N
C9	4	8.24	0.69	39.2	3.7	1561	20	95.5	7.5	multi-stage	Y
C10	2	9.37	0.78	23.8	2.0	1521	20	54.9	6.4	catastrophic	N
C11	2	9.78	1.22	45.5	5.5	1506	21	103.2	9.3	multi-stage	Y
C12	5	26.32	1.39	31.1	3.4	1025	22	32.6	7.6	catastrophic (4/5)	N
C13	4	43.67	5.96	85.4	14.3	667	43	38.0	22.1	catastrophic	N
C14	2	46.51	1.88	53.9	2.7	618	23	20.6	7.6	catastrophic	N
C15	6	48.44	4.88	36.8	3.9	586	37	12.7	11.9	catastrophic	N
C16		12.1	0.89	40.8	14.2	1427		83.2		Delamination	
C17		24.3	0.80	115.2	21.7	1075		133.2		Delamination	
C18		28.1	0.72	158.1	5.5	884		152.7		Delamination	
C19		10.9	3.32	79.8	21.1	1649		171.9		Delamination	
C20		5.3	1.49	80.4	9.8	1673		224.8		Delamination	
C21		5.8	3.84	132.2	17.4	1651		360.4		Delamination	
C22		6.5	1.65	191.9	2.2	1626		507.1		Delamination	

Table 4.4 Composite layer design (Al_2O_3 vol% and layer thickness, t) , calculated residual stress (σ_r) compared to the observed fracture behaviour, and the appearance of edge cracks for composites C1-C22.

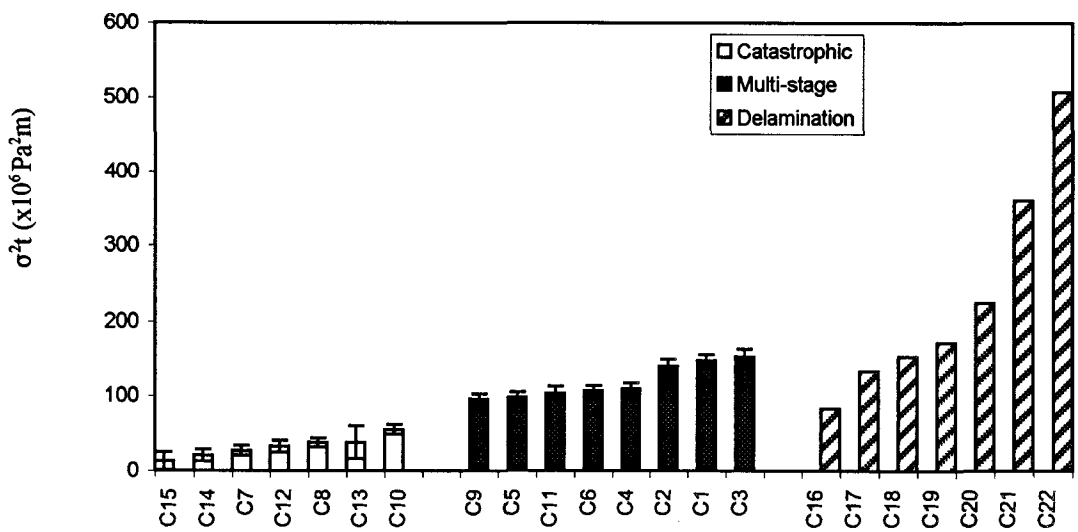

Figure 4.13 Calculated values of the geometry parameter $\sigma_r^2 t$ for all Al_2O_3/TZ3Y composites.

signficant error associated with the average for $\sigma_r^2 t$. However, variations in layer thickness *within* samples, microstructural factors (ie; grain size) or differences in sintering conditions may also contribute to the 'fuzziness' of the transition.

Conclusions can be made about the relative stability of the delaminated samples (Figure 4.13). Composites C17 ($\sigma_r^2 t = 133 \pm 27$) and C18 ($153 \pm 22$) both failed during grinding (external forces). Composites C19-C22 ($172 < \sigma_r^2 t < 507$) were less stable and failed during sintering (spontaneously, with no external forces). An exception to this pattern is composite C16 which failed during sintering. In this case, $\sigma_r^2 t$ (83 ± 2.8) is well below the delamination transition point (≈ 130) identified for the other composites. The reason may that $\sigma_r^2 t$ is an *average* quantity. There may have been one layer that was thicker than the average and for which a higher *local* value of $\sigma_r^2 t$ would exist and cause delamination fracture. Experimental verification from the delaminated composite is difficult.

Distinction can be made between single crack deflection and crack bifurcation (double deflection). **Figure 4.14** shows ESEM micrographs of deflection 'steps' in the path of an unstable crack. Steps are also visible in the cross-sections of certain catastrophic fracture samples in Figure 4.9. Composites C12, C8, C13 and C10 ($32.6 < \sigma_r^2 t < 54.9$) show small deflection steps, but C15, C14 and C7 ($12.7 < \sigma_r^2 t < 26.7$) do not. As a result, there appears to be a transition for crack deflection for $\sigma_r^2 t > 26.7$.

Composite C7 in Figure 4.9(h) is interesting because there is a single 'jog' in the crack path. ESEM micrographs of this sample **(Figure 4.15)** indicate that the jog occurs at a layer which is measurably thicker (14.9 ± 0.5 μm) than the average (10.2 ± 2.2). The calculated value of $\sigma_r^2 t$ for this thicker layer is 39.1 ± 6.0 whereas the average is 26.7 ± 6.6 (transition point for deflection derived above). This *local* variation in $\sigma_r^2 t$ appears sufficient to cause a small deflection step at the thicker layer.

(a)

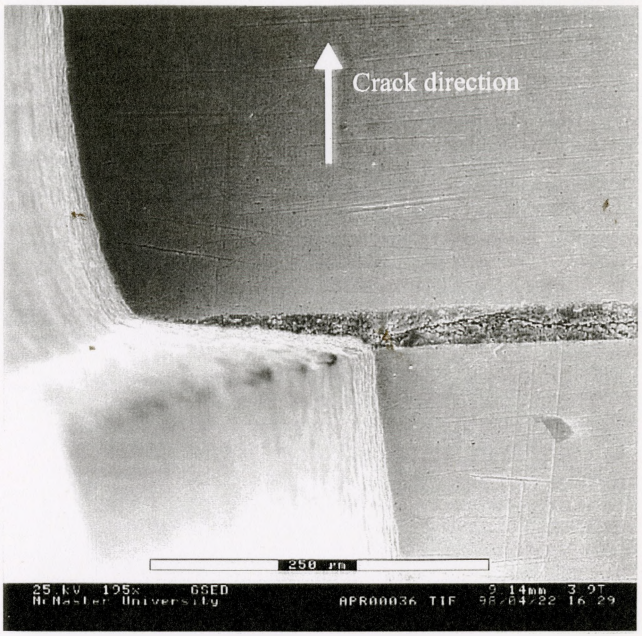

(b)

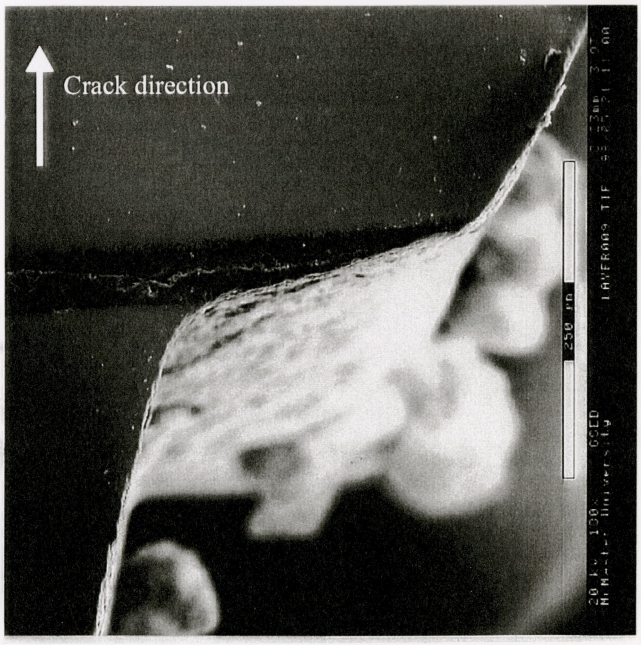

Figure 4.14 (a,b) ESEM micrographs of the deflection steps in the path of an unstable crack.

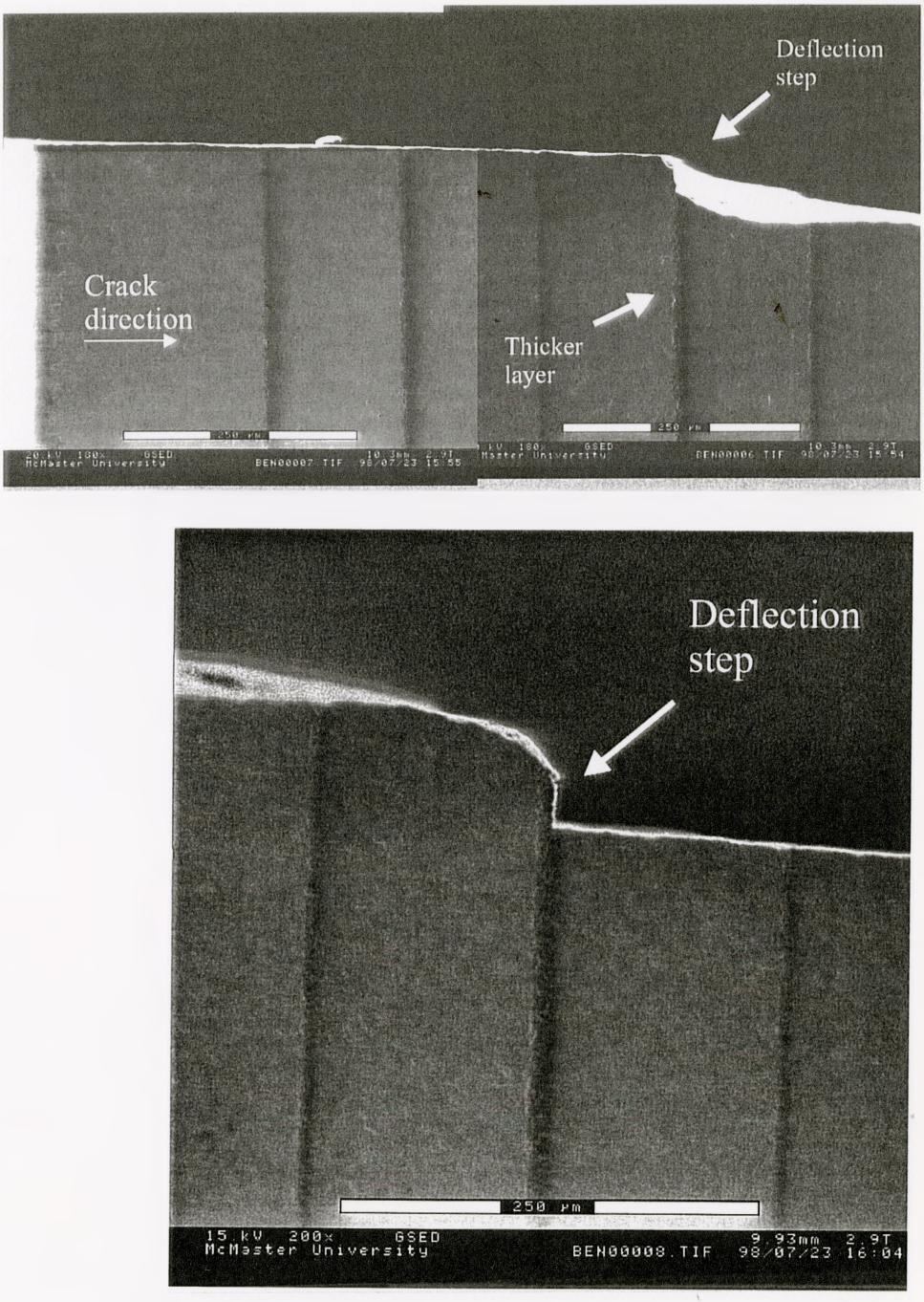

Figure 4.15 ESEM micrographs of a deflection step ('jog') in composite C7.

The transitions in the observed fracture behaviour can thus be summarized as follows;

$0 \leq \sigma_r^2 t \leq 26.7$	**Catastrophic fracture - no deflection**
$32.7 \leq \sigma_r^2 t \leq 54.9$	**Catastrophic fracture - deflection steps**
$95.5 \leq \sigma_r^2 t \leq 153.2$	**Multi-stage fracture**
$133.2 \leq \sigma_r^2 t \leq 152.7$	**Delamination during grinding**
$(\sigma_r^2 t = 83.2)$ and $171.9 \leq \sigma_r^2 t \leq 507.1$	**Delamination during sintering**

These results apply for the 10 kg indentation crack size and may differ for a different crack size due to differences in the kinetic energy of a propagating crack (ie; Figure 2.7; p.14).

4.3.3 The Initial Stage of Multi-Stage Fracture

Column A in **Table 4.5** lists the average stress to *initiate* fracture for those composites that exhibited multi-stage fracture. The tensile stress in the TZ3Y has a weakening effect on the composites and is expected to lower the apparent strength thereof (Equation 2.12; p.5). **Figure 4.16** shows the measured initial fracture strength for composites C1-C11 relative to the calculated tensile stress in the outer TZ3Y layer. Monolithic TZ3Y is represented by $\sigma_r = 0$ and the horizontal line represents the TZ3Y average. As expected, the initial stress to cause fracture in the composites decreases as the residual stress increases. Composite C11 has an initial strength *higher* than monolithic TZ3Y. There is no obvious explanation for why the tensile residual stress in the TZ3Y layer of C11 does not decrease the strength as in the other composites. Figure 4.4 indicates no significant differences in TZ3Y grain size. Additional strength measurements at high temperatures (Section 4.6) do not indicate an inherently higher strength. Possibly there was an error in the indentation load or the 4-point bend measurement.

The net stress intensity (K_{net}) can be expressed as a sum of the applied stress ($K_{applied}$), the indentation residual stress field ($K_{indentation}$) (given by Equation 2.15;p.9) and the thermal residual

Table 4.5	A	B	C
Name	Average Initial Fracture Stress (M Pa)	Average Final Fracture Stress (M Pa)	Stress Drop (M Pa)
TZ3Y		313.3	0
C1	226.8	145.6	187.0
C2	230.4	308.5	93.3
C3	273.6	479.0	119.0
C4	224.9	298.4	22.9
C5	189.1	168.1	65.8
C6	260.4	627.2	92.9
C7		225.7	0
C8		246.4	0
C9	236.7	518.8	38.6
C10		191.4	0
C11	339.9	354.9	172.6
C12	347.0	334.0	4.9
C13		478.0	0
C14		597.8	0
C15		185.5	0

Table 4.5 Initial and final fracture strength for composites C1-C15.

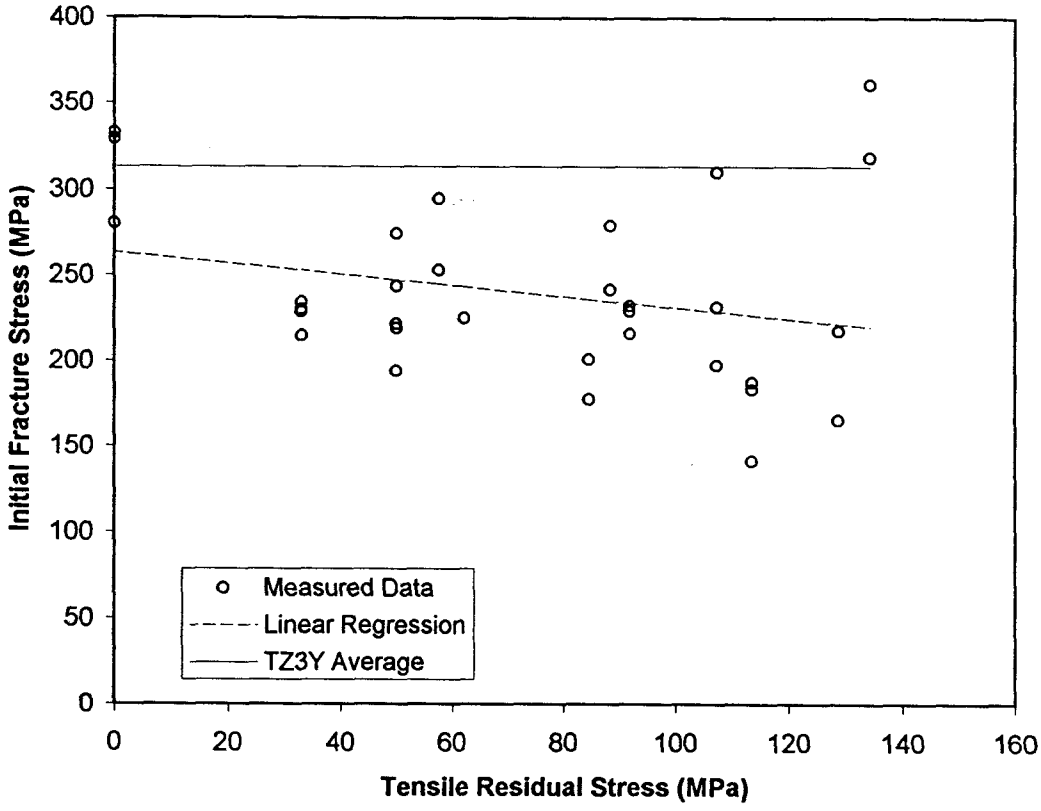

Figure 4.16 The stress for initial fracture for composites C1-C12 as a function of the calculated tensile residual stress in TZ3Y.

stress ($K_{thermal}$) (Equation 2.11;p.5), ie;

$$K_{net} = K_{applied} + K_{indentation} + K_{thermal} \qquad (4.1)$$

where $K_{applied} = \psi\sigma_f c^{1/2}$ and $K_{thermal} = \psi\sigma_r c^{1/2}$ for a uniform residual stress field (Equations 2.12;p.5 and 2.13;p.5). At the point of fracture, $K_{net} = T_o$ and $\sigma_a = \sigma_f$, which gives the result;

$$\begin{aligned} K_{applied} + K_{thermal} &= T_o - K_{indentation} \\ \psi\sigma_f c^{1/2} + \psi\sigma_r c^{1/2} &= T_o - K_{indentation} \\ \therefore \sigma_f &= (-1)\sigma_r + \left[\frac{T_o - K_{indentation}}{\psi c^{1/2}}\right] \end{aligned} \qquad (4.2)$$

Linear regression of the data in Figure 4.16 gives a slope of -0.32 ± 0.47 (95% confidence interval). The large variation of data makes it difficult to compare with Equation 4.2. There may also be error associated with the assumption of the uniformity of σ_r. Nevertheless, the trend in Figure 4.16 suggests the composites *initially* behave like monolithic TZ3Y (under tension) before the unstable cracks from the indentation intercept the Al_2O_3 layers.

4.4.4 Fracture through the Al_2O_3 Layers

Figure 4.17(a) and **(b)** illustrate the single deflection and double bifurcation of cracks found in catastrophic and multi-stage failure, respectively. In Figure 4.17(a), deflection occurs at point A to form a step (of length L_d), before kinking out of the layer at point B (and repeating at each Al_2O_3 layer. In Figure 4.17(b), bifurcation occurs at point C. Branch cracks (of length L_b) propagate through the Al_2O_3 layer and arrest before the stress is raised sufficiently to reinitiate fracture at point E (corresponding to the 'final' fracture stress).

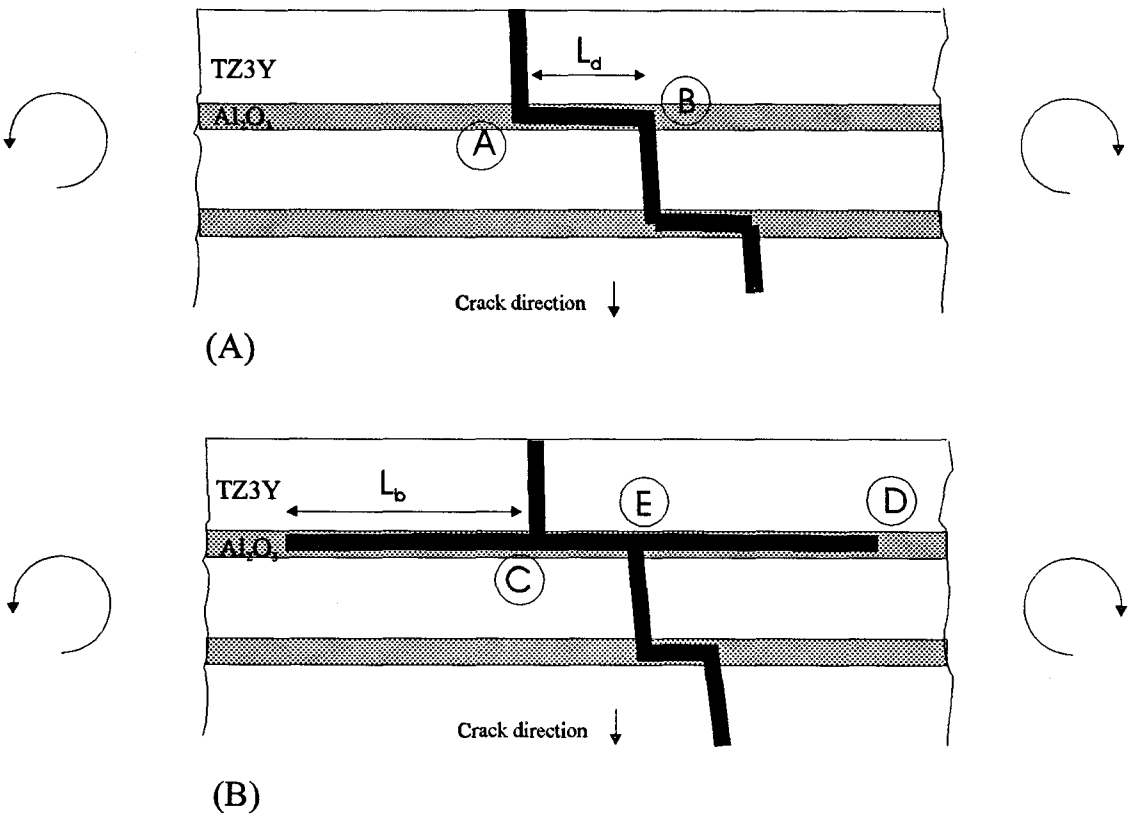

Figure 4.17 Schematic of the crack paths for (a) catastrophic failure, and (b) multi-stage fracture.

The average final fracture stress of the composites is listed in column B of Table 4.5. The average initial and final strength results for composites C1-C11 are plotted in **Figure 4.18** as a function of $\sigma_r^2 t$. The data for C12-C15 are not included because of the inconsistency of indentation in the thinner outer layers. The final strength results are scattered with no apparent relationship to $\sigma_r^2 t$.

The strain energy release rate for *edging* (Figure 2.31; p.46) reaches a maximum and decreases with crack length (Figure 2.32; p.46). It has been shown (Section 4.3) that $\sigma_r^2 t$ has an important influence on causing the initial crack bifurcation (point C on Figure 4.17b). However, there appears no relationship to the stress to *reinitiate* fracture from within the Al_2O_3 (at point E) into the next TZ3Y layer.

The magnitude of the *partial* load drop ($\Delta\sigma$) is related to the crack length L_b in Figure 4.17b. $\Delta\sigma$ is also related to the thickness of the outer TZ3Y layer, which is not constant in each case. Column C lists the average partial load drop for composites C1-C15 (zero indicates catastrophic failure). There is no obvious correlation between $\Delta\sigma$ and $\sigma_r^2 t$ **(Figure 4.19a)**. **Figure 4.19b** suggests that there is a correlation between $\Delta\sigma$ and the Al_2O_3 layer thickness, t. The rapid increase in $\Delta\sigma$ with layer thickness (at $t \approx 40$ μm) may be because thicker layers of Al_2O_3 tend to be more homogeneous than thin layers (ie; R_o is constant). Inhomogenieties such as TZ3Y grains or imperfect interfaces, are more serious in thinner layers and may limit the growth of branch cracks (and the size of $\Delta\sigma$). The reinitiation of fracture (point E) is probably from such defects in the Al_2O_3 layer. It is interesting to note that point E on the fracture sample in Oechsner *et al.* (1996) is directly below the bifurcation point, C. Observable porosity in the Al_2O_3 layer may provide defects to reiniate fracture immediately following bifurcation.

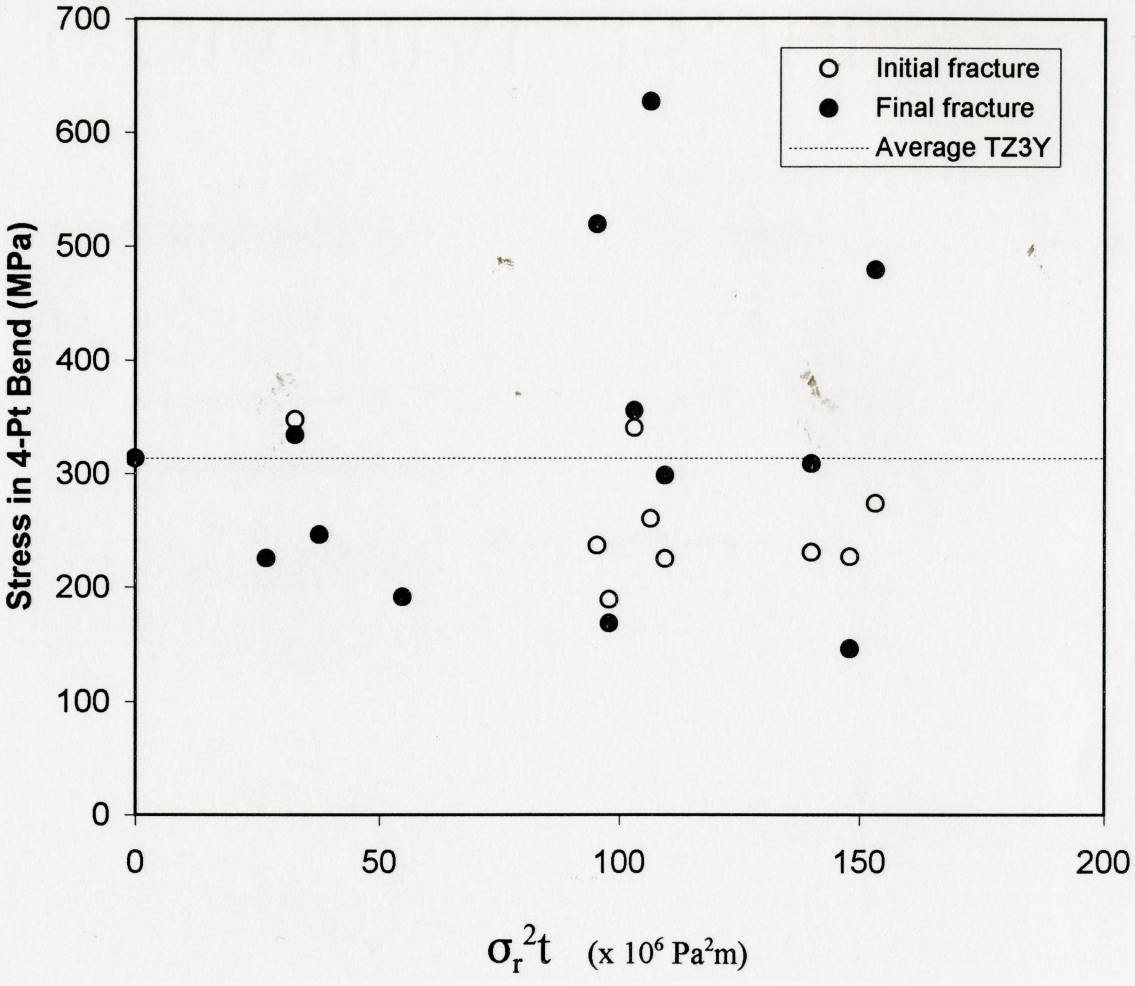

Figure 4.18 The stress for initial and final fracture for composites C1-C12 as a function of the geometry parameter $\sigma_r^2 t$.

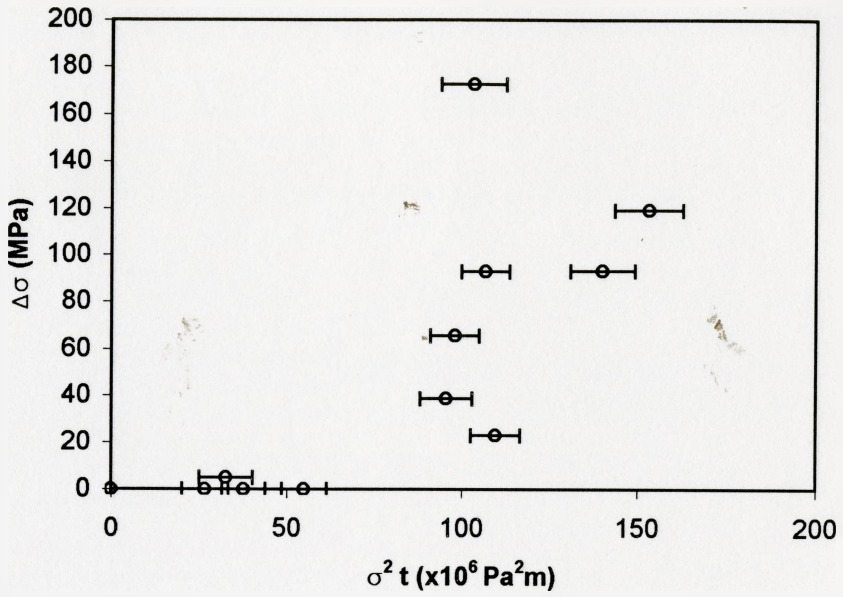

Figure 4.19(a) Average partial stress drop ($\Delta\sigma$) as a function of the geometry parameter $\sigma_r^2 t$.

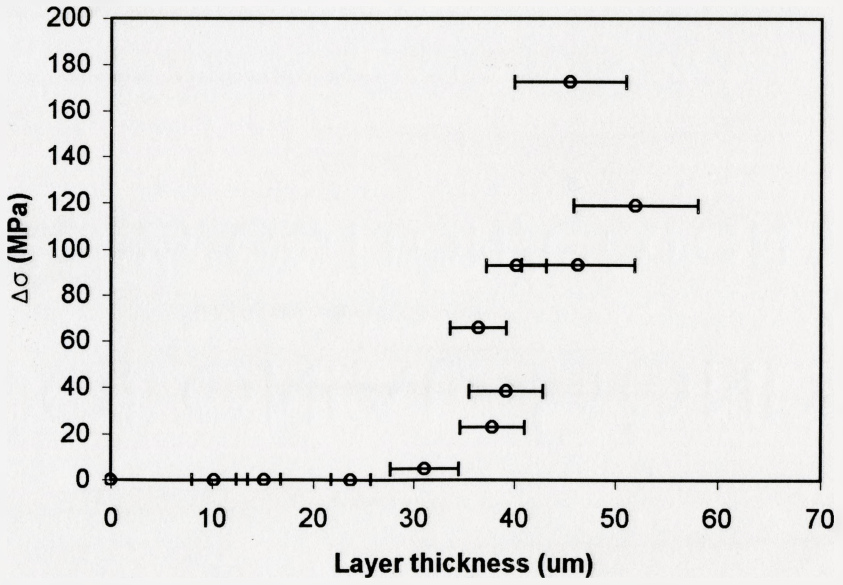

Figure 4.19(b) Average partial stress drop ($\Delta\sigma$) as a function of the average Al_2O_3 layer thickness, t.

4.4 *In Situ* Observation of Crack Propagation

The results of Section 4.3 showed that multi-layered composites with $\sigma_r^2 t < 30$ (for P = 10 kg) failed catastrophically with no evidence of crack deflection. However, the stress-deflection curves from 4-point bend testing cannot indicate the presence of stable crack propagation *prior* to the catastrophic (unstable) failure. Six samples of composite C15 (labeled A-F) were notched by laser machining (Section 3.1.2) and loaded in 4-point bend in an ESEM (Section 3.3.5) to determine if stable 'pre-cracks' form prior to catastrophic failure. A sharp notch was used to facilitate observation of the crack tip from the side of the sample. Such observations are impossible for indentation cracks embedded in the surface.

ESEM micrographs of fractured samples (A - F) are shown in **Figures 4.20 to 4.25.** Samples A and B (Figures 4.20 and 4.21) were preliminary tests and the load-deflection data is not available. Even though debris from the laser machining covered the surface (particularly sample A), it is apparent that pre-cracks appear in both samples after a load is applied. The cracks 'pop-in' at significant load then stop at the interface with the next Al_2O_3 layer (Figures 4.20(d) and 4.21(c)). Increasing the load further caused the samples to fail catastrophically with no further crack arrest.

The remaining samples were carefully polished to remove the laser machining debris then tested with simultaneous measurement of applied load and deflection. A pre-crack also appeared from the notch tip (situated in an Al_2O_3 layer) in samples C and D (Figures 4.22 and 4.23), at applied stresses of 102 MPa and 138 MPa, respectively. The pre-crack extended across the next TZ3Y layer in both cases and arrested at the next Al_2O_3 layer. Figure 4.21(d) indicates that the crack in Sample D has propagated into the Al_2O_3 a short distance. The crack length did not appear to change until catastrophic failure (at stresses of 153 MPa and 194 MPa for C and D,

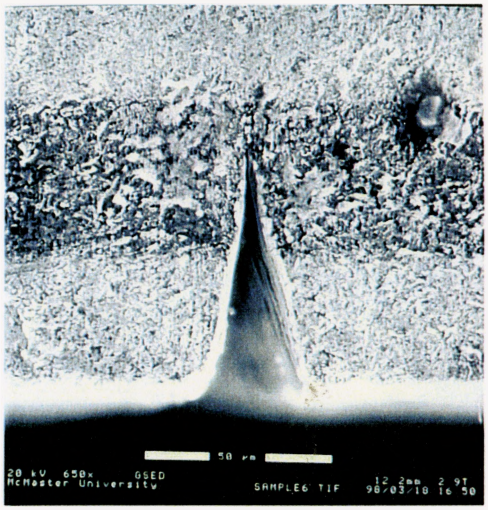

(a) A cross-section of the notch before 4-point loading (surface of sample is covered in debris from laser machining).

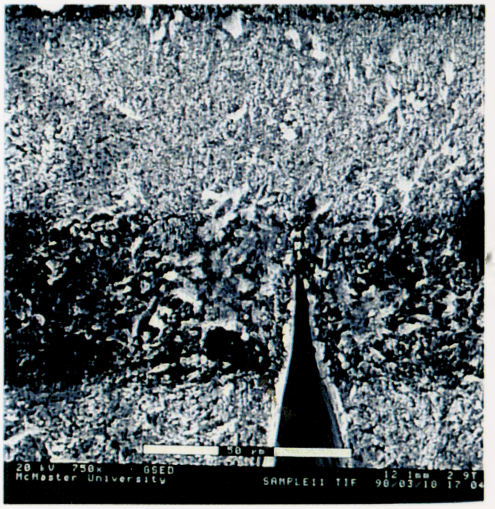

(b) The tip of the notch is located in an Al_2O_3 layer near an Al_2O_3/TZ3Y interface.

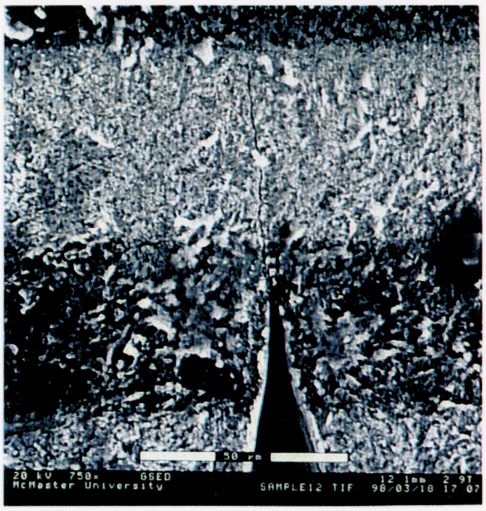

(c) After loading in 4-point bending, a crack appears at the notch tip and extends across the next TZ3Y layer.

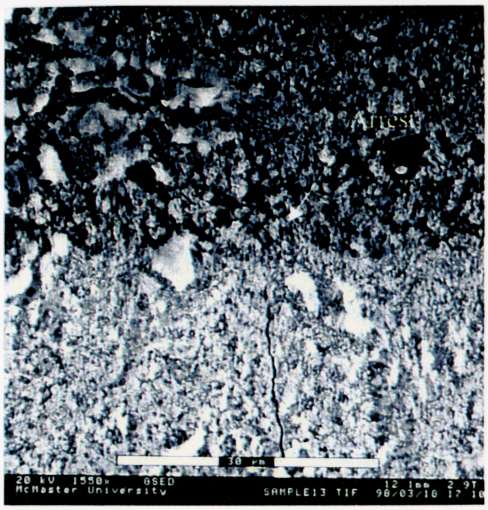

(d) Close examination of the crack tip shows that it has arrested at the TZ3Y/Al_2O_3 interface. Further application of load had no effect on the crack until catastrophic failure.

Figure 4.20 (a-d) C15 sample A

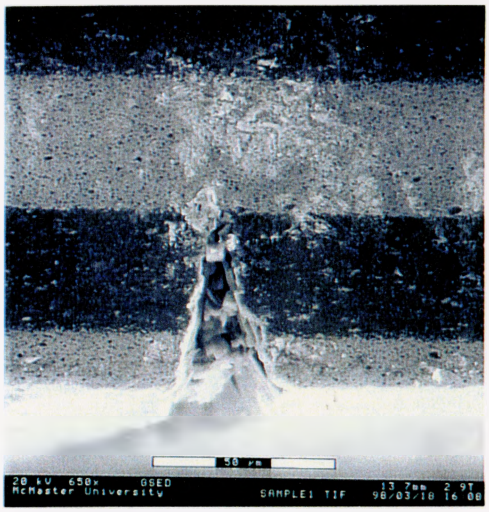

(a) A cross-section of the notch before loading in 4-point bend. The notch tip is located in an Al_2O_3 layer.

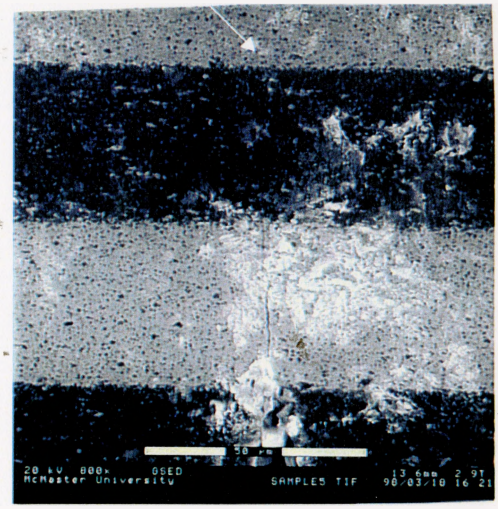

(b) After an applied stress, a crack extends across the next TZ3Y layer.

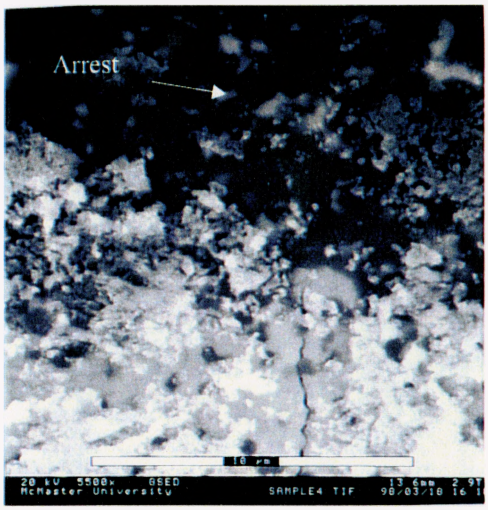

(c) Closer examination of the crack tip indicates it has extended into the Al_2O_3 layer a short distance.

Figure 4.21 (a-c) C15 sample B

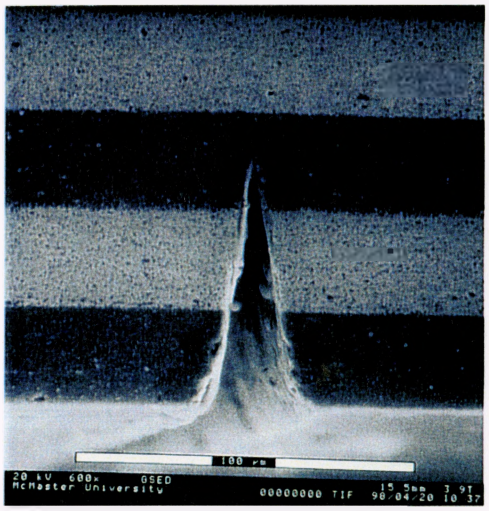

(a) A cross-section of the notch before loading in 4-point bend.

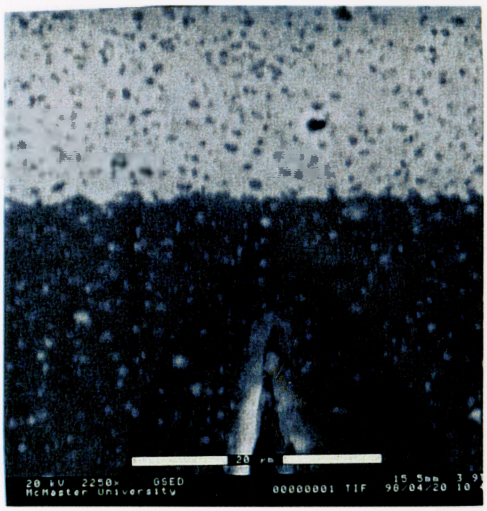

(b) The notch tip is located in an Al_2O_3 layer and there is no crack before a load is applied.

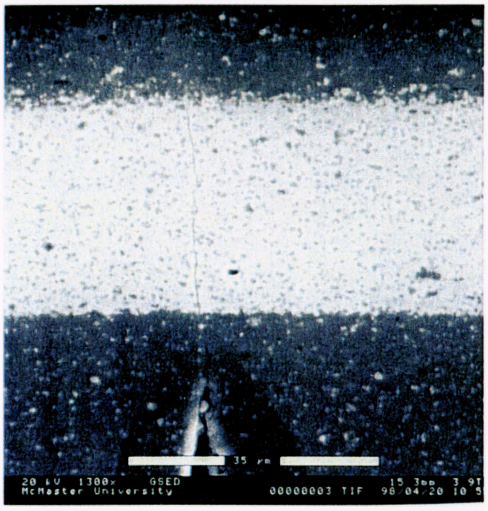

(c) At an applied load of 102 M Pa a crack appears at the notch tip and extends across the next TZ3Y layer.

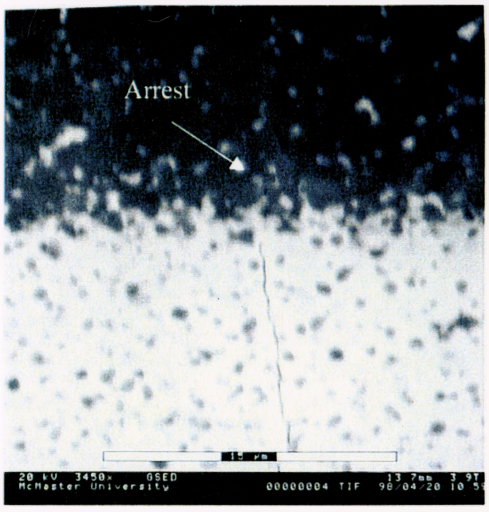

(d) Closer examination of the crack tip indicates it has arrested at the TZ3Y/ Al_2O_3 interface.

Figure 4.22 (a-d) C15 sample C

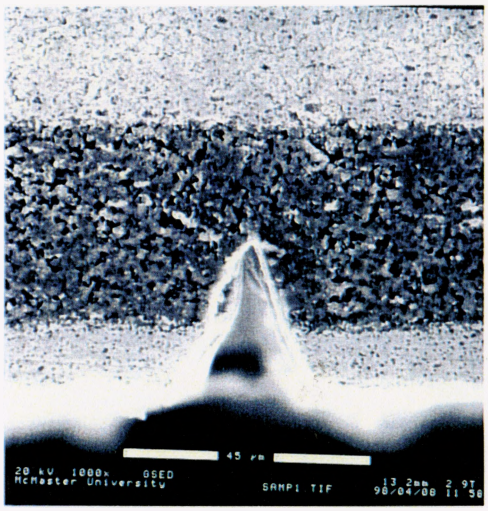

(a) A cross-section of the notch before loading in 4-point bend.

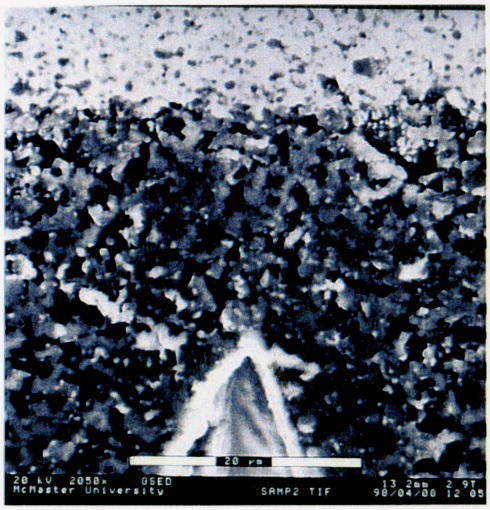

(b) The notch tip is located in an Al_2O_3 layer and there is no crack before a load is applied.

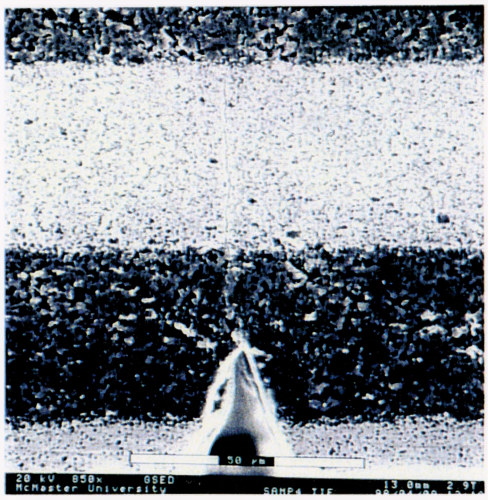

(c) At an applied stress of 138 M Pa a crack appears at the notch tip and extends across the next TZ3Y layer.

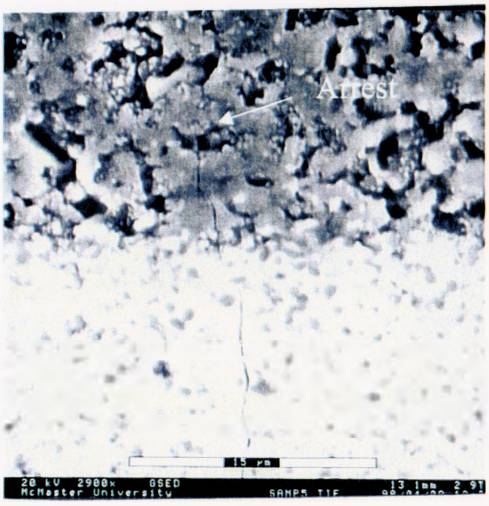

(d) Closer examination of the crack tip indicates it has arrested a short distance into the Al_2O_3 layer.

Figure 4.23 (a-d) C15 sample D

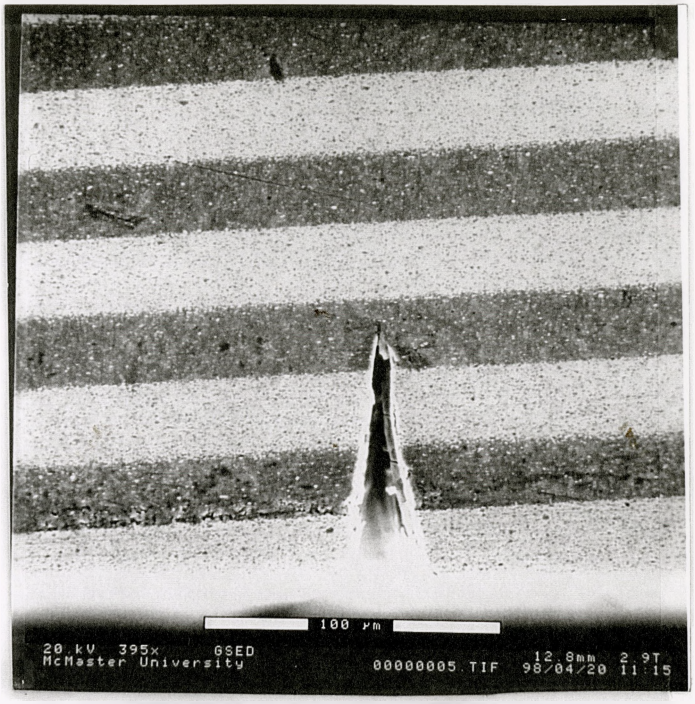

Figure 4.24 Sample E exhibited no pre-crack before catastrophic failure.

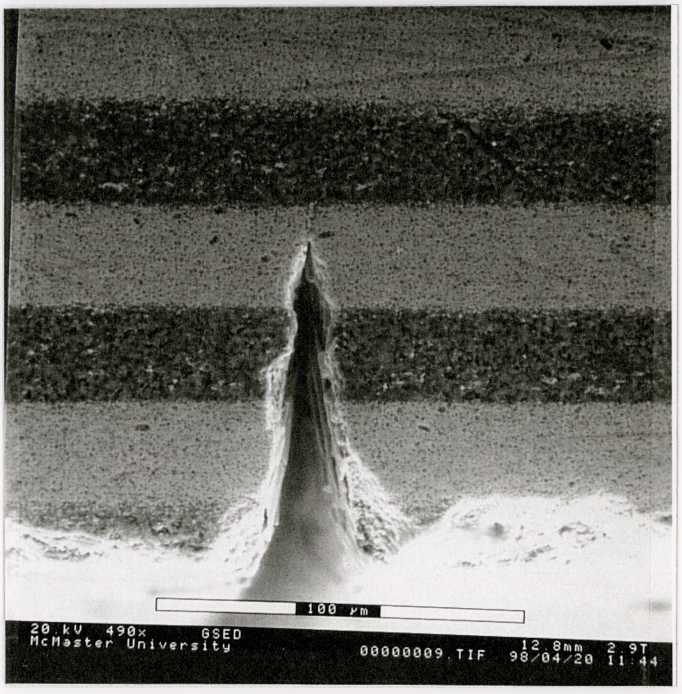

Figure 4.25 Sample F exhibited no pre-crack before catastrophic failure.

respectively). Samples E and F (Figures 4.24 and 4.25) showed no stable crack growth prior to catastrophic failure at stresses of 196 MPa and 199 MPa, respectively.

In samples A-D there is arrest of pre-cracks at the first Al_2O_3 layer encountered. The volume fraction of Al_2O_3 is relatively high in composite C15 and the average tensile stress in the TZ3Y layers ($\approx$616 MPa) is not negligible (Equation 2.28b; p.26). The average compressive stress in the Al_2O_3 layers is 586 MPa. The applied load in bending is sufficient to initiate fracture in the TZ3Y layer before the Al_2O_3 layer because of the high residual tensile stress in the former. This behaviour is similar to the initial failure of the matrix phase in a fibre composite.

The modulus of Al_2O_3 (388 GPa) is higher than TZ3Y (221 GPa) and this difference will influence the stress intensity at a crack tip approaching an Al_2O_3 layer (Section 2.3.1). A layer of higher stiffness causes a decrease in G(c) immediately ahead of the interface (Figures 2.21 and 2.23). The closely-spaced Al_2O_3 layers may also influence the size and shape of the transformation zone in the TZ3Y (Section 2.3.3) but experimental measurements thereof were beyond the scope of the present work.

4.5 The Influence of Flaw Size on Strength

The initial flaw size influences the kinetic energy that must be dissipated for crack arrest. Therefore, it is important to test the influence of indentation load on the strength (flaw tolerance) for those Al_2O_3/TZ3Y composites that exhibit multi-stage fracture (Section 4.3). ISB measurements were performed using indentation loads, P, of 100 g to 20 kg to compare the damage tolerance of composites C3, C4 and C6 with monolithic Al_2O_3 and TZ3Y.

The ISB results for monolithic Al_2O_3 and TZ3Y are shown in **Figure 4.26.** At some point, as P is reduced, the indentation cracks reach the magnitude of natural flaws in the microstructure. The thick dotted line in Figure 4.26 represents the strength of the material due to failure from natural flaws. The data points for the *lowest* indentation load represent the strength with no indentation cracks, ie; an average of 618 MPa and 1007 MPa for Al_2O_3 and TZ3Y, respectively. These results agree with other studies (Whitehead, 1994; Govilla, 1995; Ritcey, 1996).

A log-log plot of σ_f versus P has a slope of -1/3 for an ideal brittle material (Equation 2.16; p.9). The slopes for monolithic Al_2O_3 and TZ3Y are -0.238 ± 0.020 and -0.408 ± 0.071, respectively (95% confidence interval) (Figure 4.26). Fine-grained Al_2O_3 and TZ3Y exhibit no significant R-curve behaviour, ie; they are ideal brittle materials. Deviation from the ideal slope (-1/3) is likely due to the limited number of samples used for measurements. Also, samples came from 2-3 different EPD deposits. Slight variations in preparation conditions can influence the strength and toughness.

The ISB results for composites C3,C4 and C6 are shown in **Figure 4.27** (for simplification, only the curves of best fit for monolithic Al_2O_3 and TZ3Y are shown). The strength in Figure 4.27 represents the applied stress for final fracture (ignoring changes in the moment of inertia). Two-stage fracture was observed for indentation loads over 1 kg. The stress to reinitiate

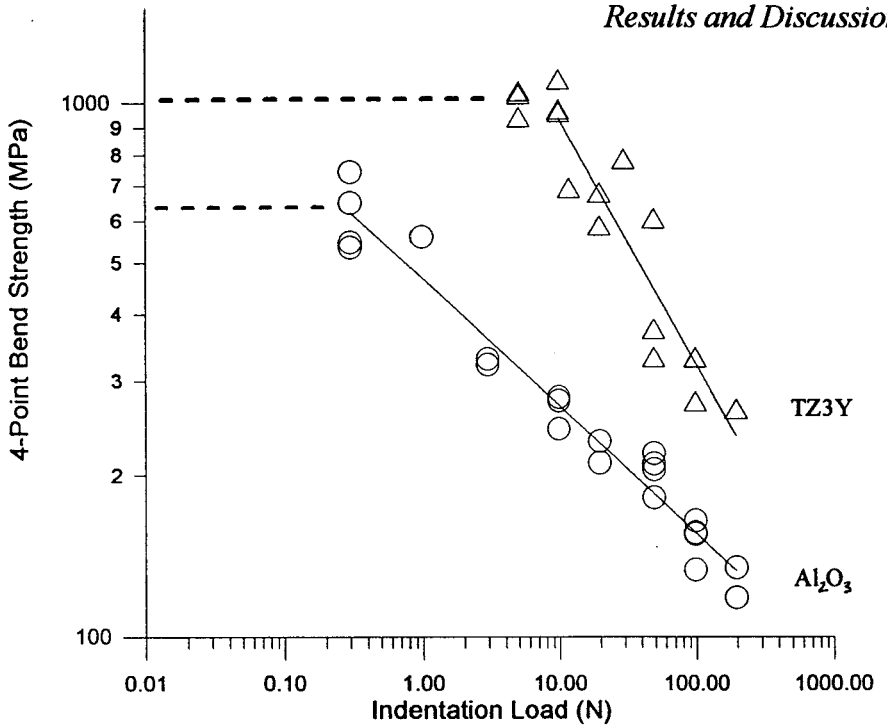

Figure 4.26 Indentation-strength (ISB) results for monolithic Al_2O_3 and TZ3Y.

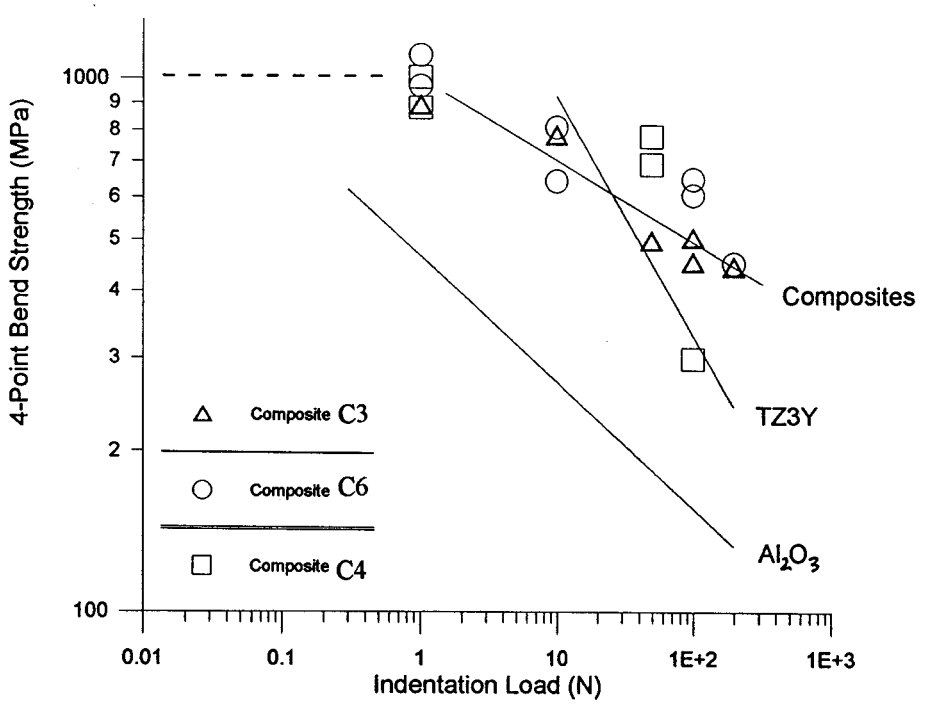

Figure 4.27 Indentation-strength (ISB) results for composites C3, C4 and C6, and the curves of best fit for monolithic Al_2O_3 and TZ3Y.

fracture after arrest and deflection at the fist Al_2O_3 layer was significantly higher than the strength for monolithic TZ3Y (one sample of composite C4 was an exception; it failed at a stress similar to that of TZ3Y). Overall, the composites demonstrate a *damage tolerance* compared with TZ3Y and Al_2O_3, ie; the strength was less dependent on the flaw size. The slope of a curve fit to the composite data as a whole (C3,C4 and C6 together) was -0.144 ± 0.049.

The laminate geometry of composites C3, C4 and C6 did *not* arrest cracks of all sizes (failure was catastrophic for $P \leq 1$ kg). The values of the parameter $\sigma_r^2 t$ in Table 4.4 for C3, C4 and C6 were calculated to be;

C3 153 ± 9.7 $(\times 10^6\ Pa^2m)$

C4 110 ± 7.1

C6 107 ± 7.0

It was found that $95.5 \leq \sigma_r^2 t \leq 153.2$ is the range for crack arrest and multi-stage fracture for P = 10 kg (Section 4.3). The results shown in Figure 4.27 indicate that $\sigma_r^2 t \geq 107$ is sufficient for the cracks associated with P = 5 kg, but not P = 1 kg. The kinetic energy associated with cracks for $P \leq 1$ kg (which includes natural flaws) is too large for arrest at the Al_2O_3 layers.

Crack arrest occurs when the strain energy release rate, G(c), falls *sufficiently* below the resistance to fracture, R(c) enough to account for the kinetic energy of an unstable, propagating crack (Section 2.1.2). Figure 2.7;p.14 illustrated the toughening influence of a ductile layer with a distinct 'step' increase in R(c). The compressive residual stress in an Al_2O_3 layer causes a distinct stepped *decrease* in G(c) in the mode-I orientation and the size of the step is proportional to σ_r^2 (Equations 2.9;p.4 and 2.13;p.5). Increasing σ_r to a sufficient level would arrest cracks initiating from flaws of *all* sizes.

4.6 High Temperature Fracture

In high temperature applications such as turbine blades, surface cracks can be initiated by thermal stress gradients during rapid cooling. The strength of polycrystalline Al_2O_3 and TZ3Y changes dramatically at elevated temperatures (Section 2.2). It is therefore important to characterize the properties of the layered Al_2O_3/TZ3Y composites compared to the monolithic materials. The strength and flaw tolerance at high temperature was tested for two composites which exhibited multi-stage fracture at room temperature (Section 4.3). This section reports and discusses the strength of composite C6 and monolithic TZ3Y at 25-1300°C. ISB measurements (P=10 kg) were used to test the flaw tolerance of composites C6 and C11 (and monolithic TZ3Y) at 25-1300°C.

4.6.1 Monolithic TZ3Y

The 4-point bend strength and the indentation-strength of TZ3Y from 25-1300°C are listed in **Table 4.6**. All results are shown graphically in **Figure 4.28.** The strength of TZ3Y decreases with temperature as transformation toughening disappears and the influence of intergranular phases increases. Differences between these results and those of Huang and Nicholson (1993) in Table 2.2;p.21 and Govilla (1995) in Figure 2.11;p.22, are likely due to microstructural differences (ie; porosity, grain size and SiO_2 impurity).

The superplasticity of TZ3Y over 1200°C is demonstrated in **Figure 4.29 (a-c)** for fracture samples at 800°C, 1000°C and 1300°C. Fracture is linear elastic up to 1000°C. At 1300°C the sample deforms permanently due to superplasticity. The applied stress at the loading rate of 0.20 mm/min reached a level corresponding to steady-state deformation (loading was stopped at the deflection limit of the 4-point bend stage). SiO_2 impurity can form a glassy Y_2O_3-SiO_2 phase at the grain boundaries which causes extensive grain boundary sliding (Huang and

Table 4.6		
Test Temperature (C)	**TZ3Y 4-Pt Bend Strength (M Pa)**	**TZ3Y ISB Strength (M Pa)**
25	1035.7	275.1
25	1047.3	332.1
25	936.6	332.7
400	495.6	274.1
400	603.1	
800	599.4	122.3
800	543.8	107.9
800	639.9	
1000	499.6	134.7
1000	627.2	146.1
1300	218.6	140.0

Table 4.6 High temperature strength of TZ3Y (no indentation) and 10 kg ISB.

Table 4.7			
Test Temperature (C)	**Composite C6 4-Pt Bend Strength (M Pa)**	**Composite C6 Indentation Strength (M Pa)**	**Composite C11 Indentation Strength (M Pa)**
25	1108.0	649.0	288.4
25	970.2	605.4	421.4
200		281.6	
400	639.3	297.5	270.2
400		232.9	177.9
800	434.2	108.9	79.5
800	449.0	136.5	79.3
1000	299.0	137.4	142.0
1000	311.2	153.0	101.8
1300	90.8	126.0	129.0

Table 4.7 High temperature strength of Composites C6 and C11 for no indentation and 10 kg indentation.

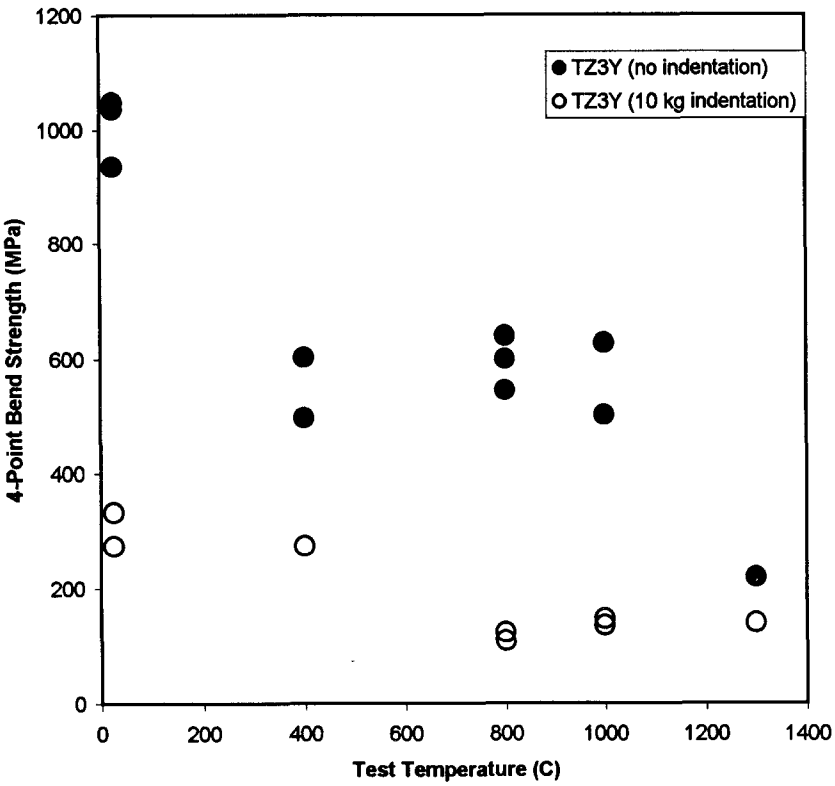

Figure 4.28 4-point bend strength of monolithic TZ3Y as a function of temperature, for standard (no indentation) and 10 kg indentation samples.

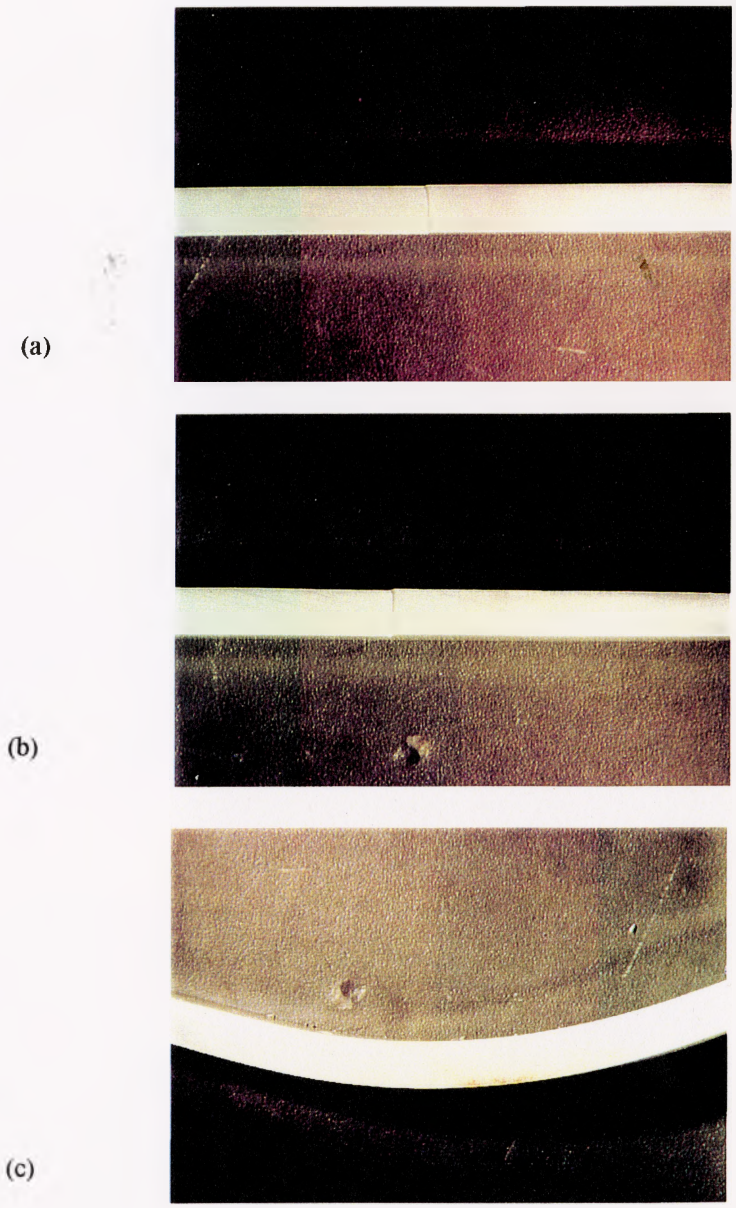

Figure 4.29 Fracture samples of monolithic TZ3Y at (a) 800°C, (b) 1000°C and (c) 1300°C (4 X magnification)

Nicholson, 1993).

The fracture surfaces of monolithic TZ3Y and Al_2O_3 at 25°C are shown in **Figure 4.30 (a,b)**. Both exhibit transgranular and intergranular fracture. The fracture surfaces of TZ3Y at temperatures of 800°C, 1000°C and 1300°C are shown in **Figure 4.30 (c-e)**. There is more intergranular fracture at higher temperature and fracture at 1300°C is completely intergranular. These observations agree with other studies (Whitehead, 1994; Govilla, 1995). The conditions for intergranular fracture in terms of crack deflection were reviewed in Section 2.1.3. An amorphous grain boundary phase appears sufficiently weak at 1300°C to cause a transition to completely intergranular fracture.

4.6.2 Multilayered Al_2O_3/TZ3Y Composites

In Section 4.3 the crack arrest and deflection observed in the fracture of multi-layered composites at room temperature has been shown to be related to the design parameter $\sigma_r^2 t$. As the test temperature increases towards 1200°C, σ_r will decrease (Equation 2.25). **Figure 4.31** is a plot of the calculated change in σ_r (compressive) with temperature in the Al_2O_3 layers of composites C6 and C11 (it is assumed that α is independent of temperature, and that thermal stresses are relaxed above 1200°C (Cai *et al.*, 1997b)).

The standard 4-point bend strength of C6 and monolithic TZ3Y (no indentation) from 25-1300°C is shown in **Figure 4.32.** At 25°C the strength of the monolithic and composite materials are not significantly different. At temperatures > 400°C the strength of the composite appears to fall significantly *below* monolithic TZ3Y which suggests the Al_2O_3 layers weaken the composite at high temperatures. It is likely that failure initiates *within* the Al_2O_3, or from the interface of Al_2O_3 and TZ3Y. These results agree with the observations of Jiménez-Melendo *et al.* (1997) for laminates of Al_2O_3/Al_2O_3+TZ3Y loaded in compression.

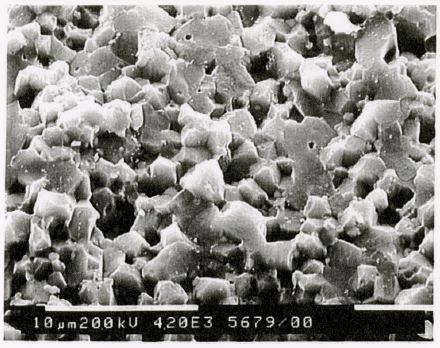

(a) Al_2O_3 (25°C)

(b) TZ3Y (25°C)

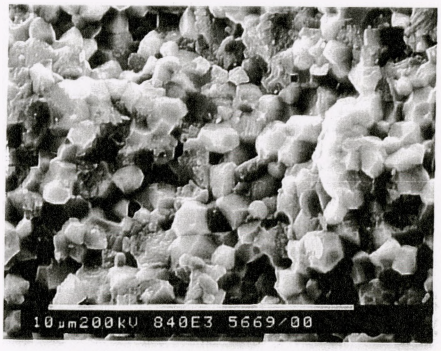

(c) TZ3Y (800°C)

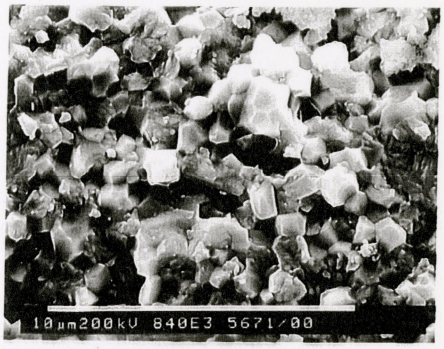

(d) TZ3Y (1000°C)

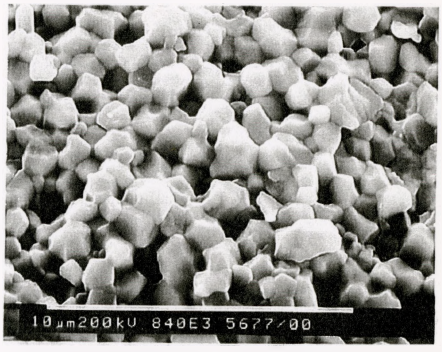

(e) TZ3Y (1300°C)

Figure 4.30 (a-e) ESEM micrographs of fracture surfaces for monolithic TZ3Y and Al_2O_3 at high temperatures.

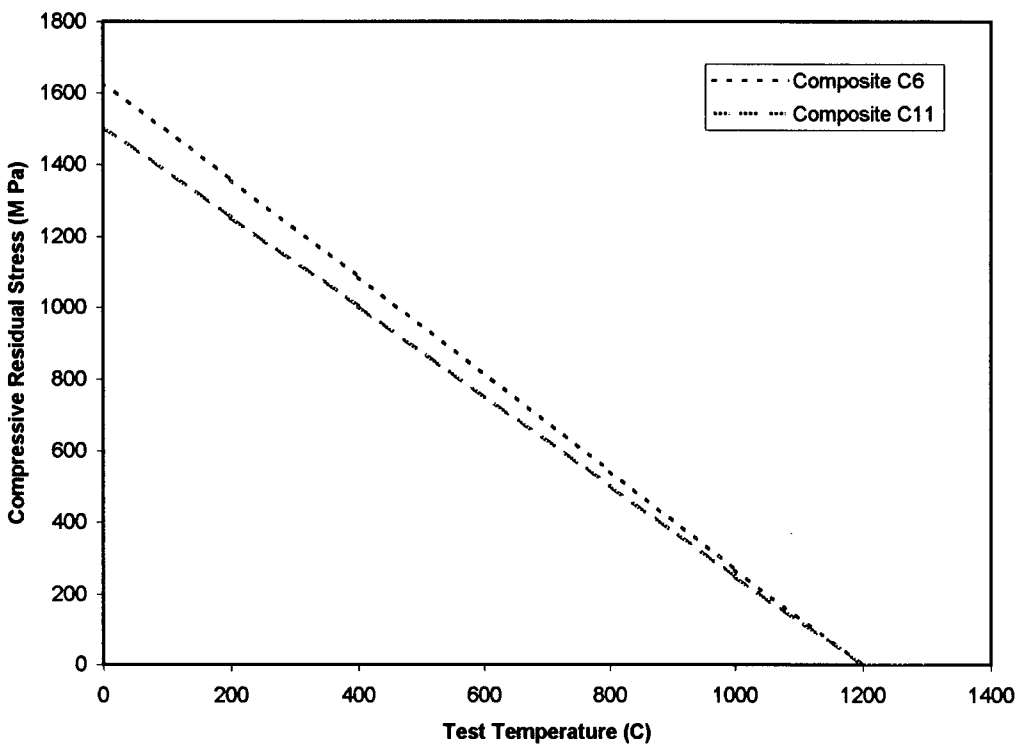

Figure 4.31 The calculated compressive residual stress in the Al_2O_3 layers of composites C6 and C11 as a function of temperature.

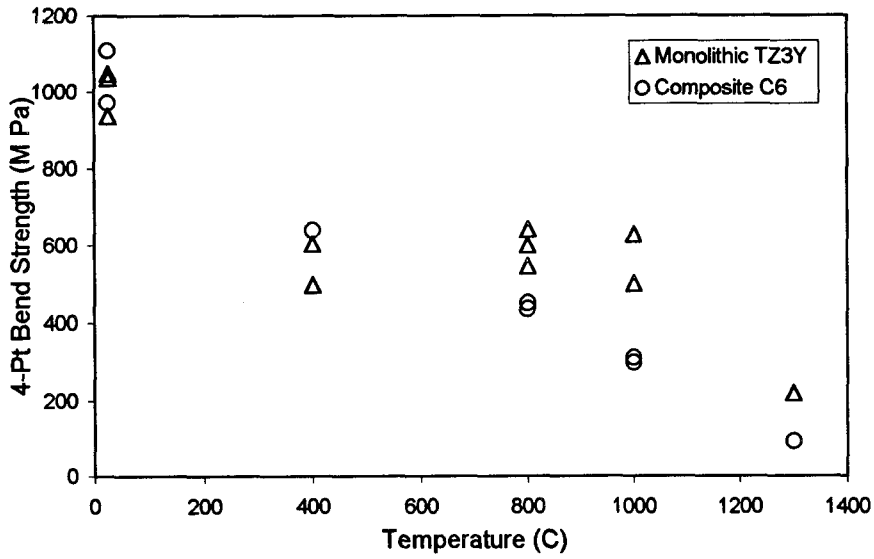

Figure 4.32 4-point bend strength of composite C6 and monolithic TZ3Y as a function of temperature (no indentation).

The ISB measurements (using a 10 kg indentation) for composites C6 and C11 between 25-1300°C are listed in **Table 4.7**; p.128. **Figures 4.33** and **4.34** show the change in indentation-strength with temperature for C6 and C11, respectively, compared to monolithic TZ3Y. Both composites o nly exhibited two-stage fracture at 25°C. Failure at higher temperatures was catastrophic (even at 200°C for composite C6).

The strength of the composites > 25°C are not significantly different from monolithic TZ3Y. Since failure initiates at the same flaw in both monolithic TZ3Y and the composites (ie; the indentation site on the tensile surface), there is no significant difference in strength in Figures 4.33 and 4.34 (unlike Figure 4.32 where the flaws are inherent to the microstructure).

Optical photographs (8X magnification) of fracture cross-sections are shown in **Figures 4.35 (a-f)** and **4.36 (a-e)** for composites C6 and C11, respectively. The superplastic deformation of the monolithic TZ3Y at 1300°C (Figure 4.29c) is not observed for the Al_2O_3/TZ3Y composites (Figures 4.35f and 4.36e). The Al_2O_3 layers effectively stiffen the structure and limit deformation of the TZ3Y. This result is comparable with the influence of β-Al_2O_3 platelets in TZ3Y at 1300°C (Huang and Nicholson,1993).

The deflection steps at the Al_2O_3 layers decrease in size as the test temperature increases (Figures 4.35 and 4.36) and disappear entirely by 1000°C. Above 1000°C there is no obvious influence of the Al_2O_3 layers on the path of the rapidly propagating crack. The reduced length of the deflected cracks is related to the decrease in residual stress with temperature (Figure 4.29; p.133). **Table 4.8** lists the layering geometry of C6 and C11 and the calculated results for $\sigma_r^2 t$ at each test temperature. The far right columns of Table 4.8 list the fracture behaviour in terms of multi-stage fracture and deflection (ie; visible fracture steps in Figures 4.35 and 4.36). Crack **arrest** (ie; multi-stage fracture) disappears for;

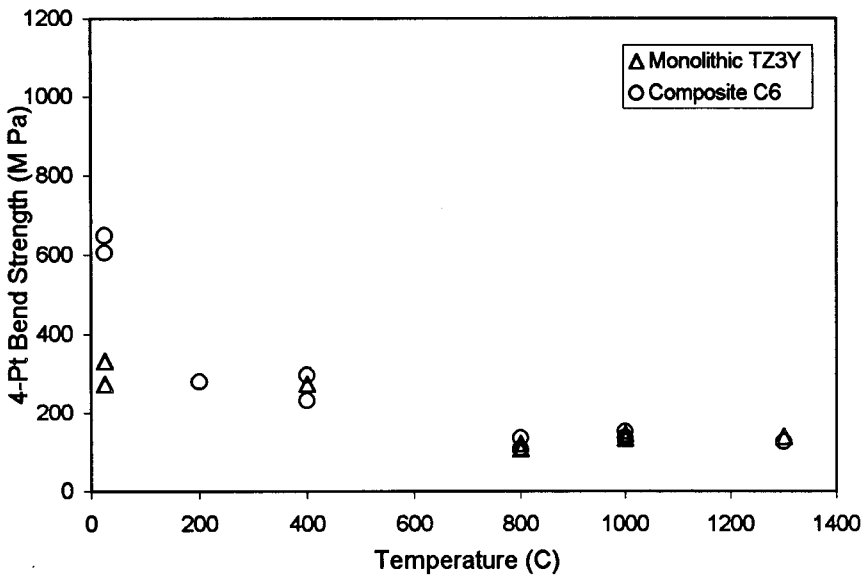

Figure 4.33 ISB strength of composite C6 and monolithic TZ3Y as a function of temperature (10 kg indentation).

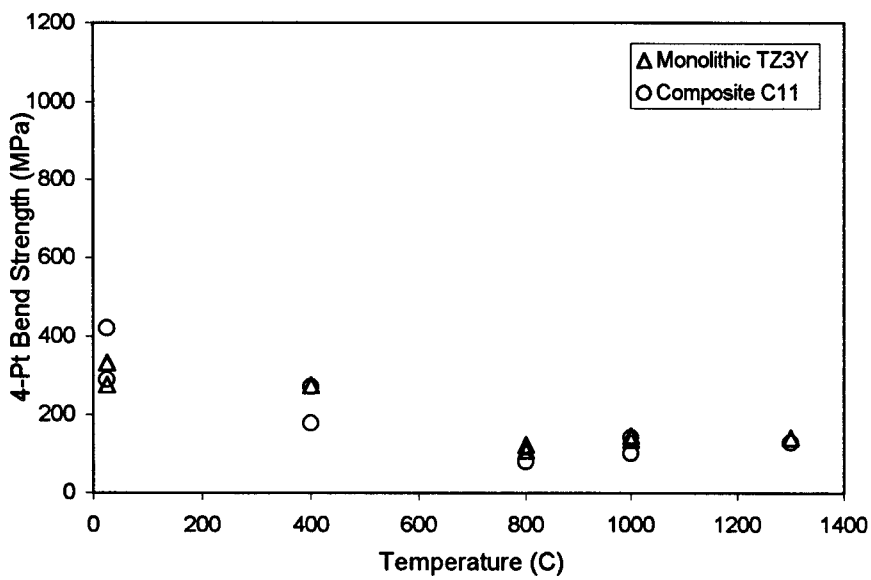

Figure 4.34 ISB strength of composite C11 and monolithic TZ3Y as a function of temperature (10 kg indentation).

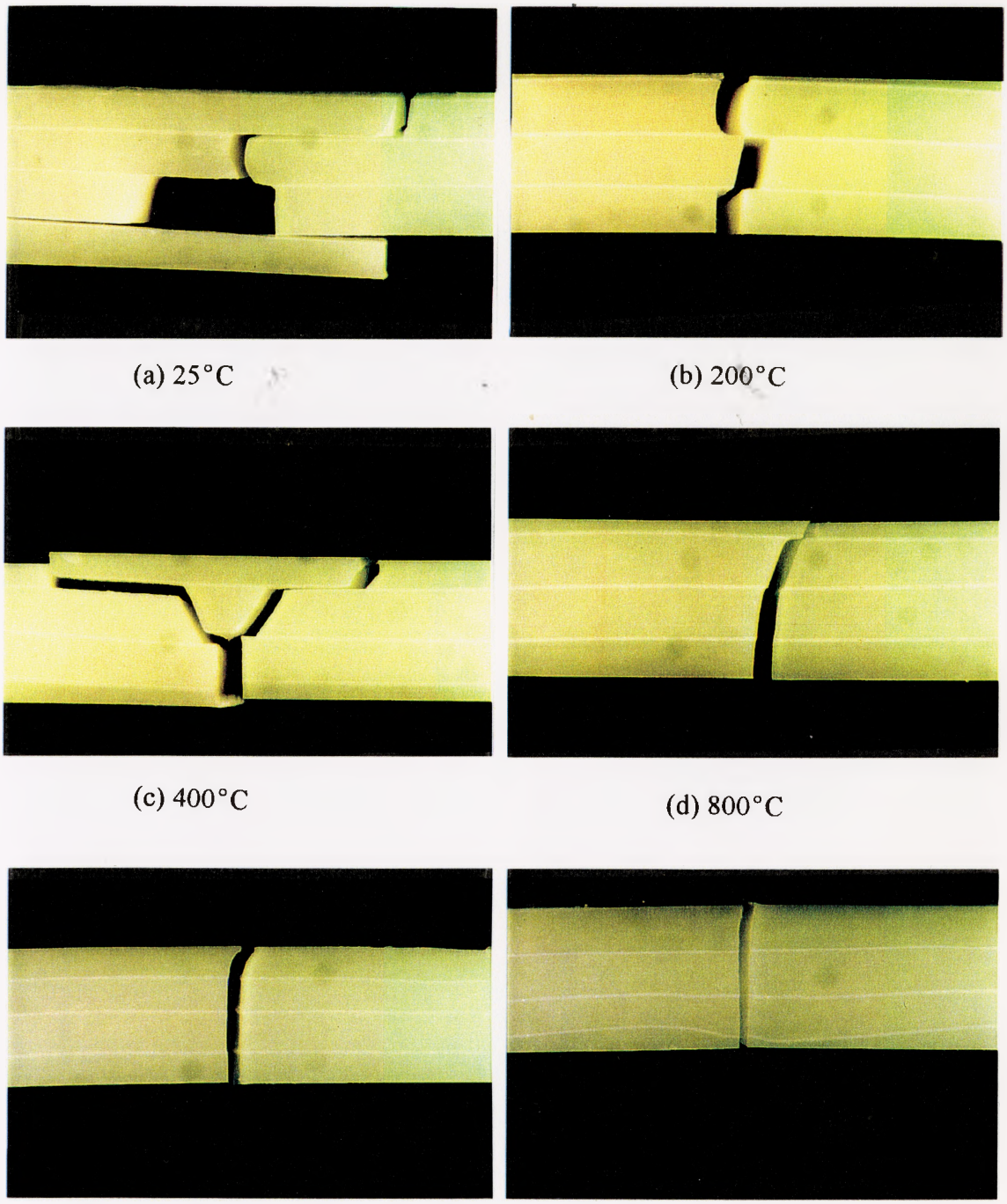

(a) 25°C (b) 200°C

(c) 400°C (d) 800°C

(e) 1000°C (f) 1300°C

Figure 4.35 (a-f) Optical photographs of fractured samples of Composite C6 at high temperatures.

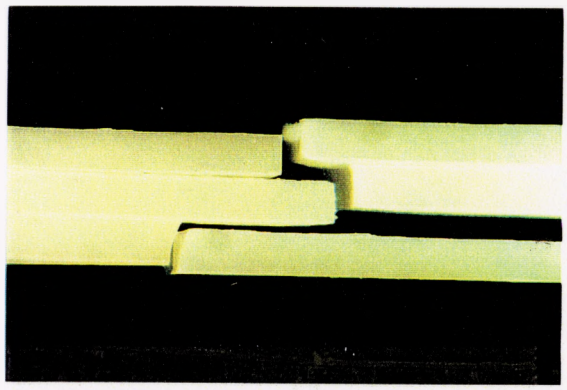

(a) 25°C

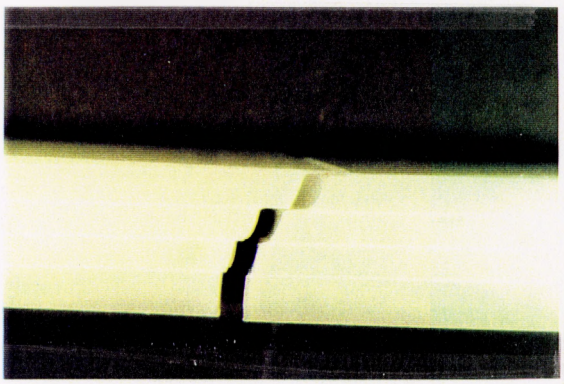

(b) 400°C

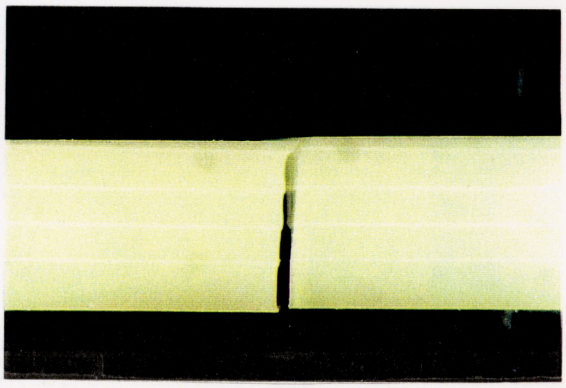

(c) 800°C

(d) 1000°C

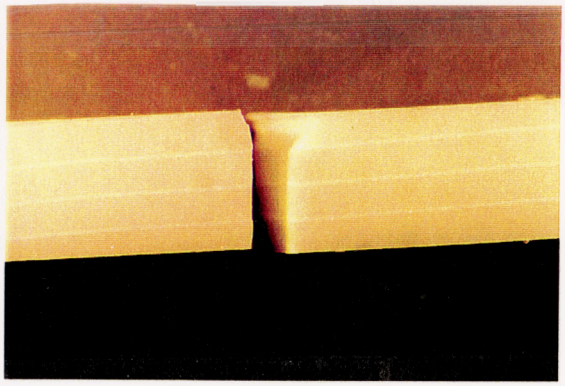

(e) 1300°C

Figure 4.36 (a-e) Optical photographs of fractured samples of Composite C11 at high temperatures.

Table 4.8

Name	Average Al_2O_3 Layer Thickness (um)	error (um)	Average Al_2O_3 Volume Fraction (Vol %)	error (%)	Test temp (C)	Calculated Stress in Al_2O_3 (Compressive) (M Pa)	error (M Pa)	σ^2t (x 10^6 Pa^6m)	error (x 10^6 Pa^6m)	**Fracture Results** Arrest (Y/N)	Deflection (Y/N)
C6	40.2	5.7	6.38	0.51	0	1630.2	20.1	106.8	9.3	Y	Y
	40.2	5.7	6.38	0.51	200	1358.5	20.1	74.2	9.3	N	Y
	40.2	5.7	6.38	0.51	400	1086.8	20.1	47.5	9.3	N	Y
	40.2	5.7	6.38	0.51	800	543.4	20.1	11.9	9.3	N	N
	40.2	5.7	6.38	0.51	1000	271.7	20.1	3.0	9.3	N	N
	40.2	5.7	6.38	0.51	1200	0.0	20.1	0.0	9.3		
	40.2	5.7	6.38	0.51	1300	0.0	20.1	0.0	9.3	N	N
C11	45.5	6.8	9.78	1.22	0	1506.4	21.4	103.3	10.6	Y	Y
	45.5	6.8	9.78	1.22	200	1255.4	21.4	71.7	10.6		
	45.5	6.8	9.78	1.22	400	1004.3	21.4	45.9	10.6	N	Y
	45.5	6.8	9.78	1.22	800	502.1	21.4	11.5	10.6	N	N
	45.5	6.8	9.78	1.22	1000	251.1	21.4	2.9	10.6	N	N
	45.5	6.8	9.78	1.22	1200	0.0	21.4	0.0	10.6		
	45.5	6.8	9.78	1.22	1300	0.0	21.4	0.0	10.6	N	N

Table 4.8 Values of σ_1^2t for composites C6 and C11 as a function of temperature, compared with the results of fracture behaviour.

$\sigma_r^2 t < 106.8 \pm 9.3$ composite C6

$\sigma_r^2 t < 103.3 \pm 10.6$ composite C11

and the fracture steps associated with crack **deflection** disappear for;

$\sigma_r^2 t < 47.5 \pm 9.3$ composite C6

$\sigma_r^2 t < 45.9 \pm 10.6$ composite C11

These results are illustrated in **Figure 4.37.**

The transitions in fracture behaviour for the high temperature results are related to the *same* range in $\sigma_r^2 t$ defined for composites C1-C15 at room temperature (Section 4.3). The ranges for deflection steps and multi-stage fracture were found to be $32.7 \leq \sigma_r^2 t \leq 54.9$ and $95.5 \leq \sigma_r^2 t \leq 153.2$, respectively. As a result, the mechanisms for deflection and bifurcation are not changed at high temperatures. The calculation of σ_r with temperature appears to be accurate.

Conclusions can now be made concerning the design of flaw tolerant ceramic composites for high temperature environments. Al_2O_3 layers in TZ3Y limit superplastic deformation at 1300°C but have no beneficial influence on the strength (or damage tolerance) of TZ3Y at high temperatures. In fact, failure seems to initiate within the Al_2O_3 layers since the standard 4-point bend strength of the composites is lower than monolithic TZ3Y.

The arrest and deflection of cracks in the Al_2O_3/TZ3Y composites is controlled by the residual stress in the Al_2O_3 layers. Since the residual stress is caused by differences in thermal expansion, it disappears at high temperatures. Means of inducing large residual stresses which are not as sensitive to temperature (ie; phase transformations) could also be employed to cause crack deflection at high temerature.

Alternatively, the ratio R_i/R_b in Equation 2.15 should be *lowered* in layered composites by using weak layers or interfaces to cause crack deflection at high temperatures. Examples of weak layers in composites are porous lanthanum aluminate (Bissinger, 1995) and graphite (Vandeperre,

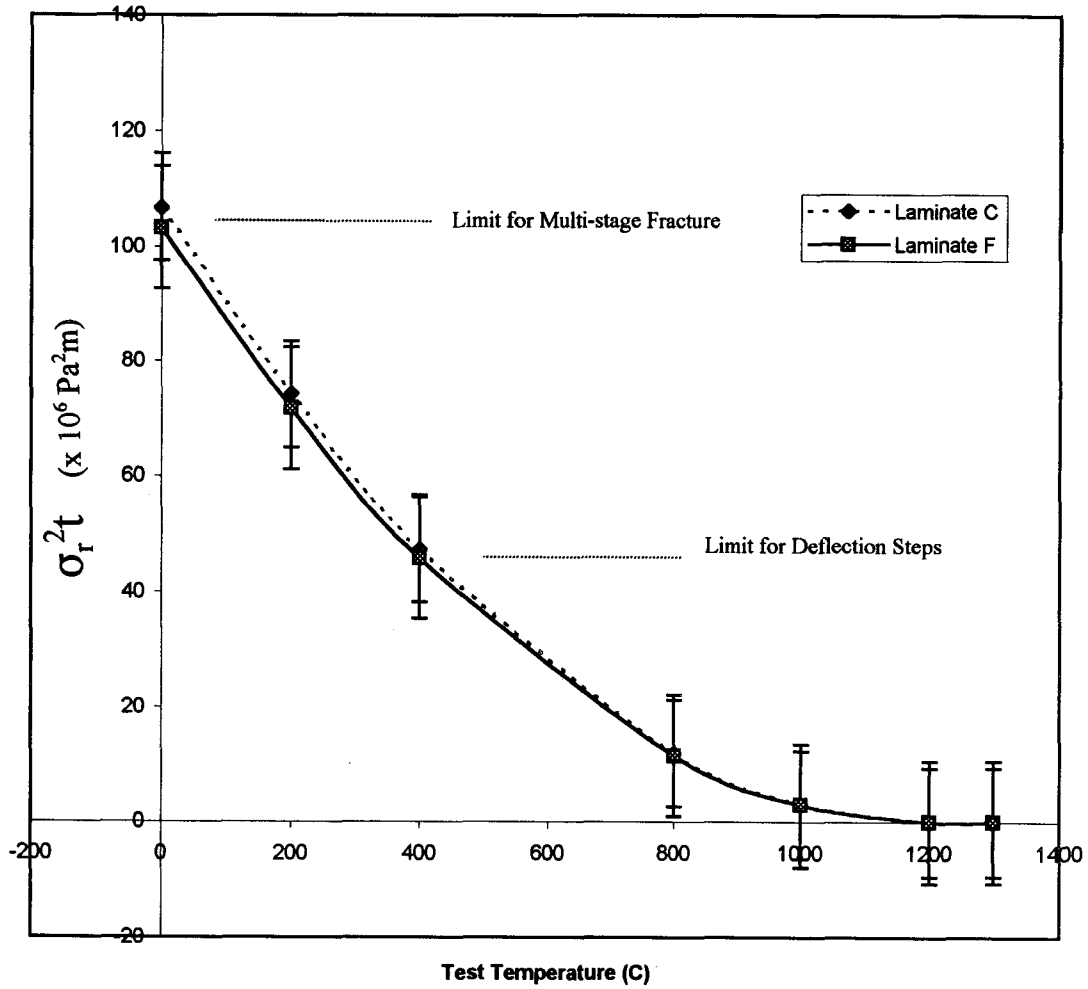

Figure 4.37 Calcuated values of $\sigma_r^2 t$ as a function of temperature for composites C6 and C11 and the corresponding changes in fracture behaviour.

1998). The effectiveness of weak layers on crack deflection should not be as sensitive to temperature as thermal residual stress. However, a major disadvantage of weak phases is the low resistance to creep, which is a useful property of materials for high temperature applications.

An advantage of using residual stress within layers to deflect and/or arrest cracks is that the fracture behaviour is sensitive to composite geometry (Section 4.3). The 'weakness' of weak layers is not easy to control by geometrical design. It seems therefore that a general damage-tolerant design must incorporate *both* compressive and weak layers. Compressive stresses would cause crack arrest at ambient temperatures whilst the weak layers would operate at both low and high temperatures.

Chapter 5: Conclusions and Future Work

The goal of this work was to identify the optimal design of a layered ceramic composite for strength and damage tolerance and thus, improved reliability in high temperature applications. The fracture behaviour of Al_2O_3/TZ3Y composites has been demonstrated over a wide range of layering geometry and temperatures. The optimal design for crack arrest and deflection, ie; multi-stage fracture, has been identified, but there was no beneficial effect of a layered combination of Al_2O_3 and TZ3Y on strength and damage tolerance at high temperatures.

Electrophoretic deposition (EPD) was used to produce layers with high density and high perfection interfaces. Two problems associated with densification by pressureless sintering were delamination and curling. Delamination was shown related to the strain energy release for the propagation of edge cracks. Failure was spontaneous for $\sigma_r^2 t > 130$. The problem of curling is not well understood but is likely related to particle size gradients which develop during the deposition process. Better control of powder size, larger suspension volumes, or increased mixing of the suspension, may prevent such gradients in depositing particle size. Alternatively, a densification procedure such as hot pressing may be used, although this is expensive and impractical for large scale use. Laser machining was effectively used to produce sharp notches in sample surfaces, and thus minimize inaccuracies associated with the large, blunt notches produced by mechanical means. The measured fracture toughness of Al_2O_3 and TZ3Y agreed with the results of other studies.

A piezospectroscopic fluorescence technique was used to measure the residual hydrostatic stress in the Al_2O_3 layers of the composite. Although the results are complicated by stress gradients at the surface, the measured stresses followed the expected relationship with Al_2O_3 volume fraction, within the expressed boundary conditions limits, σ_{min} and σ_{max}. Large variation in the measurements for composites with similar Al_2O_3 volume fraction was found to correlate with layer thickness.

The fracture behaviour of the Al_2O_3/TZ3Y composites was defined by the geometrical parameter $\sigma_r^2 t$, which confirms the model put forward by Oechsner *et al.* (1996) for a wide range

of layer designs. The appearance of deflection steps occurred at $32.7 \leq \sigma_r^2 t \leq 54.9$, and multi-stage fracture at $95.5 \leq \sigma_r^2 t \leq 153.2$. These transitions were found to hold for high temperature fracture. The transition from multi-stage fracture to complete delamination (during processing) was not well defined which suggests the layer design for multi-stage fracture is close to unstable. The partial load drop, which is related to the length of the branch cracks, was found to correlate closely with the Al_2O_3 layer thickness. It did not correlate with $\sigma_r^2 t$.

Measurements of the flaw tolerance over a wide range of indentation loads indicate that composites A,B and C maintain much higher strength than monolithic TZ3Y at large flaw sizes due to crack arrest and deflection.

In situ observation of crack propagation in composite C15, which contained a large number of 50μm Al_2O_3 layers, indicated that pre-crack growth can occur at the notch tip. The cracks were stabilized by the Al_2O_3 layer. Layered designs with large Al_2O_3 volume fractions were susceptible to failure of the TZ3Y layers due to large residual tensile stresses.

Multi-stage fracture was not observed at temperatures > 25°C, due to the decrease of compressive residual stress in the Al_2O_3 layers. The high temperature strength measurements indicate that the flaw tolerance of Al_2O_3/TZ3Y composites is not better than monolithic TZ3Y. The standard strength (no indentation) of the composites was found to be significantly lower than TZ3Y. The latter indicates that failure must initiate at an Al_2O_3 layer or an Al_2O_3/TZ3Y interface. Superplastic deformation of the TZ3Y component of the composites at 1300°C was prevented by the constraint of the Al_2O_3 layers. Flaw-tolerant design of layered ceramic composites should include crack arrest/deflection mechanisms which are not temperature sensitive, such as weak interfaces.

There are several aspects of the present work which can be applied to future studies. Characterization of the curling of deposits during sintering is important for producing consistent layer design. It was suggested that a gradient in particle size may be the cause of curling. Measurement of layer thickness *during* EPD using an on-line ultrasonic technique (Patel, 1997) would allow more control on the layer design of composites.

Layered composites for practical use should incorporate compressive residual stress in the

outer layers to improve the strength to initiate fracture. The thermal shock of Al_2O_3/TZ3Y layered composites could be tested using a standard quench test. Also, the impact resistance (ie; using ballistic tests) of these composites would be an interesting study. Models are necessary to describe the stress to reinitiate fracture after bifurcation, and the failure mechanism of layered Al_2O_3/TZ3Y composites at high temperatures.

Mechanisms for residual stress which are not based on thermal expansion are necessary for multi-stage fracture at high temperature. Alternatively, weak interfaces can be incorporated into layered Al_2O_3/TZ3Y composites.

References

Anderson, T.L. Fracture Mechanics: Fundamentals and Applications (2nd Edition), CRC Press, Boca Raton, Fl. (1995).

Becher, P.F. "Microstructural Design of Toughened Ceramics", J.Am.Ceram.Soc., 74 [2] (1991), 255-69

Bissinger, M. "High Temperature Strength and Toughness of Electrophoretically Deposited Alumina/Lanthanum Aluminate Lamintes" M.Eng Thesis, McMaster University (1995).

Bluhm, J. "Fracture Arrest" Fracture: An Advanced Treatise Volume 5: Fracture Design of Structures, Ed.H.Liebowitz, Academic Press, New York (1969),1-65

Boccaccini, A.R. and Ponton, C.B. "Processing Ceramic-Matrix Composites Using Electrophoretic Deposition," JOM, [10] (1995) 34-42

Braun, L., Bennison, S.J. and Lawn, B.R. "Objective Evaluation of Short-Crack Toughness Curves Using Indentation Flaws: Case Study on Alumina-Based Ceramics" J.Am.Ceram.Soc. 75 [11] 3049-57 (1992)

Broek, D. Elementary Engineering Fracture Mechanics, Sijthoff & Noordhoff, Alphen aan den Rijn, Holland (1978) .

Cai, P.Z., Green, D.J. and Messing, G.L. "Constrained Densification of Alumina/Zirconia Hybrid Laminates, I: Experimental Observations of Processing Defects", J.Am.Ceram.Soc., 80 [8] (1997a) 1929-39

Cai, P.Z., Green, D.J. and Messing, G.L. "Constrained Densification of Alumina/Zirconia Hybrid Laminates, II: Viscoelastic Stress Computation," J.Am.Ceram.Soc., 80 [8] (1997b) 1940-48

Chantikul, P., Anstis, G.R., Lawn, B.R. and Marshall, D.B. "A Critical Evaluation of Indentation Techniques for Measuring Fracture Toughness: II, Strength Method", J.Am.Ceram.Soc. 64 [9] (1981) 539-543

Chen, Z. and Mecholsky, J.J. "Damage-Tolerant Laminated Composites in Thermal Shock", J.Mat.Sci., 28 (1993) 6365-6370

Clarke, D. "Methods of Measuring Residual Stress in Ceramics," Presented at 100th Annual Meeting of the American Ceramic Society, Cincinnati. May 4-6, 1998.

Cook, R.F., Lawn, B.R. and Fairbanks, C.J. "Microstructure-Strength Properties in Ceramics: I, Effect of Crack Size on Toughness," J.Am.Ceram.Soc., 68 [11] (1985) 604-615

Davidge, R.W. and Green, T.J. "The Strength of Two-phase Ceramic/Glass Materials," J.Mat.Sci., [3] (1968) 629-634

De, D. and Nicholson, P.S. "High-Perfection Ceramic Microstructures - The Role of Coagulation Mechanisms " Submitted to J.Am.Ceram.Soc. (1998)

Derjaguin, B.V. and Landau, L.D. Acta Pysiochim, URSS 14 (1941) 633-52

Fischer, R., Fischer, E., De Portu, G. and Roncari, E. "Preparation of Ceramic Micro-laminate by Electrophoresis in Aqueous System," J.Mat.Sci.Letters, 14 (1995) 25-27

Garvie, R.C., Hannink, R.H.J. and Pascoe, R.T. "Ceramic Steel," Nature 258 (1975) 703

Govilla, R.K. "Strength Characterization of Yttria-Partially Stabilized Zirconia," J.Mat.Sci., 30 (1995) 2656-2667

Grabner, L. "Spectroscopic Technique for the Measurement of Residual Stress in Sintered Al_2O_3," J.Appl.Phys., 49 [2] (1978) 580-83

Green, D.J. "Compressive Surface Strengthening of Brittle Materials by a Residual Stress Distribution," J.Am.Ceram.Soc. 66 (1983) 807

Green, D.J., Hannink, R.H.J. and Swain, M.V. Transformation Toughening of Ceramics. CRC Press Inc., Boca Raton, Florida.(1989)

Griffith, A.A. "The Phenomena of Rupture and Flow in Solids," Phil.Trans.Roy.Soc.of London, A 221 (1921) 163-197

Gupta, T.K. "A Qualitative Model for the Development of Tough Ceramics," J.Mat.Sci., 9 (1974) 1585-1589

Gupta, T.K. "Strengthening by Surface Damage in Metastable Tetragonal Zirconia," J.Am.Ceram.Soc., 6 (1980) 117

Hansen, J.J., Cutler, R.A., Shetty, D.K. and Virkar, A.V. "Indentation Fracture Response and Damage Resistance of Al_2O_3-ZrO_2 Composites Strengthened by Transformation-Induced Residual Stresses," J.Am.Ceram.Soc., 71 [12] (1988) C-501-C-505

Harmer, M.P., Chan, H.M. and Miller, G.A. "Unique Opportunities for Microstructural Engineering with Duplex and Laminar Ceramic Composites," J.Am.Ceram.Soc., 75 [7] (1992) 1715-28

Hasselman, D.P.H. "Unified Theory of Thermal Shock Fracture Initiation and Crack Propagation in Brittle Ceramics," J.Am.Ceram.Soc., 52 [11] (1969) 600-604

Hasselman, D.P.H. "Thermal Stress Resistance Parameters for Brittle Refractory Ceramics: A Compendium," J.Am.Ceram.Soc., 49 [12] (1970) 1033-36

He, J. and Clarke, D.R. "Determination of the Piezospectroscopic Coefficients for Chromium-Doped Sapphire," J.Am.Ceram.Soc., 78 [5] (1995) 1347-53

He, M-Y. and Hutchinson, J.W. "Crack Deflection at an Interface Between Dissimilar Elastic Materials," Int.J.Solids Struct., 25 [9] (1989) 1053-1067

He, M-Y., Evans, A.G. and Hutchinson, J.W. "Crack Deflection at an Interface Between Dissimilar Elastic Materials: Role of Residual Stresses," Int.J.Solids Struct., 31 [24] (1994) 3443-3455

Hillman, C., Suo, Z. and Lange, F.F. "Cracking of Laminates Subjected to Biaxial Tensile Stresses," J.Am.Ceram.Soc., 79 [8] (1996) 2127-33

Hilton, P.D. and Sih, G.C. "A Laminate Composite with a Crack Normal to the Interfaces," Int.J.Solids Structures, 7 (1971) 913-930

Ho, S., Hillman, C., Lange, F.F. and Suo, Z. "Surface Cracking in Layers Under Biaxial, Residual Compressive Stress," J.Am.Ceram.Soc., 78 [9] (1995) 2353-59

Huang, X-N. and Nicholson, P.S. "Mechanical Properties and Fracture Toughness of α-Al_2O_3-Platelet-Reinforced Y-PSZ Composites at Room and High Temperatures," J.Am.Ceram.Soc., 76 [5] (1993) 1294-301

Hutchinson, J.W. and Suo, Z. "Mixed Mode Cracking in Layered Materials," Advances in Applied Mechanics, 29 (1992) 63-168

Jayatilaka, A.S. Fracture of Engineering Brittle Materials. Applied Science Publishers, London (1979).

Jiménez-Melendo, M., Clauss, C. and Dominguez-Rodriguez, A. "Microstructure and High-Temperature Mechanical Behaviour of Alumina/Alumina-Yttria-Stabilized Tetragonal Zirconia Multilayer Composites," J.Am.Cer.Soc., 80 [8] (1997) 2126-30

Kelly,A. and MacMillan, N.H. Strong Solids, 3rd Edition. Clarendon Press, Oxford (1986).

Kingery, W.D. "Factors Affecting Thermal Stress Resistance of Ceramic Materials", J.Am.Ceram.Soc., 38 [1] (1955) 3-15

Kingery, W.D., Bowen, H.K. and Uhlmann, D.R. Introduction to Ceramics, 2nd Edition. John Wiley & Sons, New York (1976).